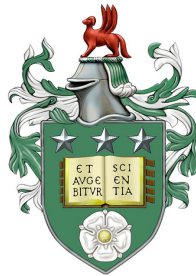


Plane Wave Imaging Beamforming Techniques
for Medical Ultrasound Imaging



Zainab Rami Saleh Alomari
School of Electronic and Electrical Engineering
University of Leeds

A thesis submitted for the degree of

Doctor of Philosophy

May 2017

The candidate confirms that the work submitted is her own, except where work which has formed part of jointly-authored publications has been included. The contribution of the candidate and the other authors to this work has been explicitly indicated below. The candidate confirms that appropriate credit has been given within the thesis where reference has been made to the work of others.

Chapter 3 contains materials from *Alomari et al. (2015)*.

Chapter 4 contains materials from *Alomari et al. (2014)*.

©2017. The University of Leeds and Zainab Alomari.

This copy has been supplied on the understanding that it is copyright material and that no quotation from this thesis may be published without proper acknowledgement.

To Prophet Mohammad (PBUH)

Acknowledgements

First of all, I thank Allah for his guidance and support not only through my study but also through my whole life.

I would like to express my special gratitude to my supervisors Dr. Steven Freear and Dr. Sevan Harput. Their continuous support, guidance and discussions during my study were essential for me to reach this level and be able to complete my research.

I am thankful to my parents who were the first to encourage me to apply for PhD study. No word can show how grateful I am to them for their continuous support, prayers and love.

My special gratitude and thanks go to my dear husband, Mohanad, who did everything to support me during my study. Regardless of his study and valuable time; he was always there for me. Also I would like to say thank you to my beloved sisters for their unconditional support and love.

Special Thanks go to all the members of the Ultrasound Group in Leeds University, it was a pleasure to do my PhD study with this group. Also I would like to say thank you to Leeds University who provided all the required resources and facilities to help us feel comfortable during our research. Special thanks to the Iraqi ministry of higher education and scientific research and to everyone who helped me get the opportunity of studying PhD at Leeds University.

Abstract

In ultrasound array imaging, the beamforming operation is performed by aligning and processing the received echo signals from each individual array element to form a complete image. This operation can be performed in many different ways, where adaptive and non-adaptive beamformers are considered as the main categories. Adaptive beamformers exploit the statistical correlation between the received data to find a weighting value at the focal point, instead of using a fixed weighting window in non-adaptive beamforming. This results in a significant improvement in the image quality in terms of resolution and sidelobes reduction. This improvement is necessary for ultrafast imaging because of the lack of focusing in Plane Wave Imaging (PWI) that results in lowering the SNR, and thus the produced imaging quality is reduced.

This thesis analyses different adaptive beamforming techniques for ultrafast imaging. For accurate medical diagnosis, the frame rate, the imaging resolution, contrast and speckle homogeneity are all considered as important parameters that contribute to the final imaging result.

To be able to evaluate each technique by minimizing the effect of external parameters, two different analysis were performed. First an empirical expression for PWI lateral resolution is produced after studying the effect of the imaging parameters on this imaging method. Then a method for selecting the suitable steering angles in Compound Plane-Wave Imaging (CPWI) is introduced, with a detailed explanation for the effect of the compound angles on resolution and sidelobes level.

In order to add the contrast improvement to the properties of adaptive beamformers, some techniques like the coherence-based factors and Eigenspace-Based Minimum Variance (ESBMV) are produced in the literature. After demonstrating the principle of Minimum Variance adaptive beamformer, a detailed comparison for the types of coherence-based factors is given. In addition, a new technique of Partial-ESBMV is introduced to modify reference ESBMV so that no Black Box Region artefacts nor dark spots appear when using this method in medical imaging. After explaining its background and properties using cystic and wire phantoms, the proposed method is applied to the real RF data of carotid artery, as an application to clarify the efficiency of this method in medical ultrasound imaging.

Contributions

The work carried out in this thesis adds four different contributions to the field of ultrafast ultrasound imaging, where unfocused plane waves are used to form B-mode grey scale images. These contributions are as follows:

- A detailed study for the effects of the imaging parameters on spatial resolution in PWI is presented. Out of this study, an empirical expression that describes the relation between PWI lateral resolution and the imaging parameters is derived. This work is published in the following paper:

- Zainab Alomari, S. Harput, S. Hyder, and S. Freear, ” *The effect of the transducer parameters on spatial resolution in plane-wave imaging*”, in IEEE International Ultrasonics Symposium (IUS), 2015, pp. 1-4.

- A new method is presented to calculate the angular range within which the steering angles in CPWI are selected, depending on the transducer sensitivity, maximum imaging depth and medium attenuation. An explanation for the effect of the compounded angles on lateral resolution and sidelobe levels in CPWI is also presented. This work is published in the following paper:

- Zainab Alomari, S. Harput, S. Hyder, and S. Freear, ” *Selecting the number and values of the CPWI steering angles and the effect of that on imaging quality*”, in IEEE International Ultrasonics Symposium (IUS), 2014, pp. 1191-1194.

- Six different types of coherence-based factors are explained in detail. These factors are implemented to be compared from different perspectives using experimental RF-data.

- A new beamforming method of Partial-ESBMV is proposed. This method can completely remove the Black-Box Region (BBR) artefacts introduced by reference ESBMV without requiring any additional computations. In addition, when combined with CPWI, the proposed method can reduce the dark spots presented in the speckle generating backgrounds by reference ESBMV. This work is submitted for publication in the following paper:

- Zainab Alomari, S. Harput, D. M. Cowell, Asraf Moubark and S. Freear, ”*Partial eigenspace-based minimum variance (PESBMV) beamforming for medical ultrasound imaging*”, IEEE Transactions on Ultrasonics, Ferroelectrics, and Frequency Control, (Manuscript is currently under process).

The other publications that include contributions from this work are:

- A. Moubark, Zainab Alomari, S. Harput and S. Freear, ”*Comparison of spatial and temporal averaging on ultrafast imaging in presence of quantization errors*”, in IEEE International Ultrasonics Symposium (IUS), 2015, pp. 1-4.
- A. Moubark, Zainab Alomari, S. Harput and S. Freear, ”*Enhancement of contrast and resolution of B-mode plane wave imaging (PWI) with non-linear filtered delay multiply and sum (FDMAS) beamforming*”, in IEEE International Ultrasonics Symposium (IUS), 2016, pp. 1-4.
- S. Hyder, S. Harput, Zainab Alomari and S. Freear, ”*Two-way quality assessment approach for tumour detection using free-hand strain imaging*”, in IEEE International Ultrasonics Symposium (IUS), 2014, pp. 1853-1856.
- S. Hyder, S. Harput, Zainab Alomari, D. M. J. Cowell, J. McLaughlan and S. Freear, ”*Improved shear wave-front reconstruction method by aligning imaging beam angles with shear-wave polarization: Applied for shear compounding application*”, in IEEE International Ultrasonics Symposium (IUS), 2016, pp. 1-4.

Contents

Acknowledgements	iii
Abstract	iv
Contributions	i
List of Figures	v
List of Tables	xii
Nomenclature	xiv
1 Introduction	1
1.1 Literature Review	2
1.2 Motivation	4
1.3 The Objectives and Organization of the Thesis	6
I The Properties of Ultrafast Ultrasound Imaging Techniques	10
2 Ultrasound Imaging Techniques	11
2.1 Linear Imaging	11
2.2 Plane Wave Imaging (PWI)	13
2.3 Compound Plane-Wave Imaging (CPWI)	15
2.3.1 The Steering Operation	16
2.3.2 DAS Beamforming in CPWI	18

2.3.3	Compounding Operation	20
2.4	CPWI Properties	21
2.4.1	Advantages	23
2.4.2	Disadvantages	23
2.5	CPWI Applications	24
2.5.1	Elastography	24
2.5.2	Doppler Flow Imaging	26
2.5.3	Microbubble Imaging	27
3	Spatial Resolution in PWI	28
3.1	Field-II Simulations Description	30
3.2	Methodology	31
3.3	Results	31
3.3.1	Spatial Resolution versus Bandwidth	32
3.3.2	Spatial Resolution versus Central Frequency	33
3.3.3	Spatial Resolution versus the Number of Elements	34
3.3.4	Spatial Resolution versus Aperture Width	36
3.3.5	Spatial Resolution versus Imaging Depth	37
3.4	Lateral Resolution Empirical Expression	38
3.5	Lateral Resolution in the Presence of Attenuation	39
3.6	Lateral Resolution in the Presence of Medium Nonlinearity	40
3.7	Discussion	42
3.8	Conclusions	44
4	The Selection of CPWI Parameters	45
4.1	Methodology	46
4.2	Experimental Setup	49
4.2.1	Wire Phantom	49
4.2.2	Specifying the Angular Range	49
4.2.3	Specifying the Number of Compounded Angles	50
4.3	Results and Discussions	51
4.3.1	B-mode Images	51
4.3.2	Spatial Resolution	54
4.3.3	Level of Artefacts	58

4.4	Conclusions	61
-----	-----------------------	----

II Minimum Variance Adaptive Beamforming Techniques 62

5	Minimum Variance Adaptive Beamforming: Background and Properties	65
5.1	Minimum Variance (MV) Beamformer Background Method	66
5.2	Temporal Smoothing in MV	69
5.3	Spatial Smoothing in MV	71
5.4	Robustness in MV	71
5.5	Computational Complexity of MV	72
5.6	Field II Simulations	73
5.7	Results	74
5.8	Discussion	82
5.9	Conclusions	84
6	Coherence Factor-Based Imaging Combined with Adaptive and Non-Adaptive Beamforming Techniques	86
6.1	Background Theory	87
6.1.1	Coherence Factor (CF)	87
6.1.2	Generalized Coherence Factor (GCF)	88
6.1.3	High Resolution Coherence Factor (HRCF)	89
6.1.4	Sign Coherence Factor (SCF)	90
6.1.5	Spatio-Temporally Smoothed Coherence Factor (StS-CF)	91
6.1.6	Scaled Coherence Factor (scCF)	92
6.2	Lab Experiments	93
6.2.1	Phantoms	93
6.2.2	Experimental Setup	94
6.3	Quality Metrics	96
6.4	Results and Discussion	97
6.4.1	Using Coherence-Based Factors with DAS Beamformer	97
6.4.2	Using Coherence-Based Factors with MV Beamformer	113

6.4.3 Using Coherence-Based Factors with CPWI	114
6.5 Conclusions	115
7 Partial Eigenspace-Based Minimum Variance for Medical Ultra-	
sound Imaging	117
7.1 Introduction	118
7.2 Eigenspace-Based Minimum Variance (ESBMV)	120
7.3 Proposed Method	123
7.4 Experimental Setup	126
7.5 Quality Metrics	127
7.6 Results	128
7.6.1 Plane-Wave Imaging (PWI)	128
7.6.2 Compound Plane-Wave Imaging (CPWI)	132
7.6.3 In-vivo Imaging of a Human Carotid	136
7.7 Discussion	137
7.8 Conclusions	142
8 Conclusions	143
8.1 Resolution in PWI	144
8.2 CPWI Parameters	145
8.3 PESBMV	145
Appendix	148
1 Signal Travel Time in CPWI	148
2 Ring Down Time of the Transducer	149
3 Constructed Matlab Functions	149
3.1 MV Function	149
3.2 ESBMV Function	152
3.3 PESBMV Function	152
References	154

List of Figures

2.1	A schematic diagram for the transmitted ultrasound beam in: (a) PWI and (b) Linear Imaging.	14
2.2	A schematic diagram shows the steering operation of ultrasound beams using linear arrays. Steering is achieved by pulsing the transducer elements with two different amounts of fixed delays to steer with angles: (a) θ_1 and (b) θ_2 , where $\theta_1 > \theta_2$	16
2.3	The role of the apodization in minimizing the effect of the grating lobes (a)without the steering (b)with the steering.	18
2.4	The Array Factor plot at different steering angles is used to show the angle at which grating lobes occur.	19
2.5	A schematic diagram for the effect of steering on the time t_{tr} required for the signal to travel from the transmitter to any field point $p(x, z)$	20
2.6	The scattering points model used during Field II simulations and laboratory experiments.	21
2.7	Field II simulations for the point targets phantom shown in figure 2.6, using: (a) incoherent and (b) coherent compounding, using different numbers of compounded angles within the $\pm 7^\circ$. All images are displayed with a dynamic range of 60 dB.	22
3.1	The lateral resolution when decreasing the step size in the lateral direction, for a PSF at the 30mm depth.	30
3.2	The effect of the bandwidth on spatial resolution. Wavelength is fixed to $308\mu\text{m}$	33
3.3	The effect of the central frequency on spatial resolution, for a PSF at the 30mm depth.	34

LIST OF FIGURES

3.4	The effect of the wavelength on lateral resolution, for a PSF at the 30mm depth.	34
3.5	Spatial resolution vs. the total number of elements for a PSF at the 30mm depth. Aperture width is fixed to 30mm and wavelength is $308\mu\text{m}$	35
3.6	The effect of the aperture width on spatial resolution in the absence of medium attenuation. Wavelength is fixed to $308\mu\text{m}$	36
3.7	The effect of the imaging depth on spatial resolution in the absence of medium attenuation. Wavelength is fixed to $308\mu\text{m}$	37
3.8	Simulated 9 scattering points located at the depths from 30 to 190mm to show the effect of increasing the depth on lateral resolution in: (a) linear imaging focused at 70mm depth and (b) PWI.	38
3.9	Matlab curve fitting tool for the lateral resolution versus b , which resembles the wavelength multiplied by the imaging depth and divided by the total aperture width.	40
3.10	Lateral Resolution versus the imaging depth, with and without the presence of attenuation.	41
4.1	The maximum intensity received by the field points at the centre of the transducer at a range of steering angles.	47
4.2	The change in the angular range with the imaging depth using different aperture sizes.	48
4.3	(a) The model of the scattering points simulated using the wire phantom (b) The wire phantom used in the lab experiments.	50
4.4	Experimental results of the wire phantom when using CPWI with different numbers of compounded angles within the $\pm 10.5^\circ$	52
4.5	Experimental results of the wire phantom when using linear imaging with different numbers of elements in the aperture.	53
4.6	A comparison of the axial resolution between linear imaging at different aperture sizes and CPWI at different numbers of compounded angles at the -10dB width, for the point at the 40mm depth, $x=0\text{mm}$. Wavelength is fixed to $293\mu\text{m}$	55

LIST OF FIGURES

4.7	A comparison between the lateral resolution in PWI and linear imaging with different aperture widths, for the point at the 40mm depth in figure 4.5.	56
4.8	The CPWI lateral resolution when using different numbers of compounded angles, for the point at the 40mm depth in figure 4.4.	57
4.9	A comparison of the -10dB lateral resolution between linear imaging at different aperture sizes and CPWI at different numbers of compounded angles, for the 40mm depth point.	58
4.10	The area that represents the interference between the lateral resolutions of three images steered with: (a) $-\theta_1, 0, +\theta_1$ (b) $-\theta_2, 0, +\theta_2$, where: $\theta_2 > \theta_1$	59
4.11	(a) The two rectangles at the sides of the 40mm depth point, at which the maximum of artefacts is measured as given in (b) when compounding different numbers of angles.	59
5.1	The operation of subarray smoothing that divides the transducer elements into P subarrays, each of them consists of L_p elements.	68
5.2	A schematic diagram that shows the steps followed during: (a) DAS beamforming and (b) MV beamforming.	70
5.3	Field II simulated point targets using: (a) DAS with Boxcar receive apodization, (b) DAS with Hamming receive apodization, (c) MV ($L_p=32$, $K=60$), (d) MV ($L_p=48$, $K=60$), (e) MV ($L_p=64$, $K=60$), (f) MV ($L_p=32$, $K=0$), (g) MV ($L_p=48$, $K=0$), (h) MV ($L_p=64$, $K=0$). All images are produced with 50dB dynamic range.	75
5.4	Comparing the lateral resolution of DAS and MV for the 40mm depth point shown in figure 5.3, for images: a and b for DAS and c , d and e for MV produced with temporal smoothing of $K=60$	76
5.5	Comparing the lateral resolution of DAS and MV for the 40mm depth point shown in figure 5.3, for images: a and b for DAS and f , g and h for MV produced with temporal smoothing of $K=0$	77

LIST OF FIGURES

5.6	Simulated point targets using MV beamformer in the presence of various amounts of Diagonal Loading with the subarray length being 64 elements. (a) $K=60$, $\Delta=1/20L_p$, (b) $K=60$, $\Delta=1/10L_p$, (c) $K=60$, $\Delta=1/L_p$, (d) $K=0$, $\Delta=1/20L_p$, (e) $K=0$, $\Delta=1/10L_p$, (f) $K=0$, $\Delta=1/L_p$. All images are produced with 50dB dynamic range.	78
5.7	Comparing the lateral resolution of MV beamformer for the 40mm depth point shown in figure 5.6, in the presence of different amounts of Diagonal Loading. $L_p=64$ element and $K=60$	79
5.8	Comparing the lateral resolution of MV beamformer for the 40mm depth point shown in figure 5.6, in the presence of different amounts of Diagonal Loading. $L_p=64$ element and $K=0$	80
6.1	The effect of the coefficient P on SCF using equation 6.9, for the values from 1 to 8.	91
6.2	scCF versus CF at $\eta(SNR) = 1/N$, according to equation (6.13).	94
6.3	The phantom model used for assessing the imaging quality of the coherence-based factors in this chapter. (a) The cystic phantom. (b) The wire-targets phantom.	95
6.4	Ultrasound images of the cystic phantom shown in figure 6.3(a), using DAS beamformer, for different types of coherence-based methods. All images are displayed with a dynamic range of 60 dB.	98
6.5	Ultrasound images of the cystic phantom shown in figure 6.3(a), using DAS beamformer and CPWI, for different types of coherence-based methods. All images are displayed with a dynamic range of 60 dB.	99
6.6	Ultrasound images of the cystic phantom shown in figure 6.3(a), using MV beamformer, for different types of coherence-based methods. All images are displayed with a dynamic range of 60 dB.	100
6.7	Ultrasound images of the cystic phantom shown in figure 6.3(a), using MV beamformer and CPWI, for different types of coherence-based methods. All images are displayed with a dynamic range of 60 dB.	101
6.8	Ultrasound images of the wire-targets phantom shown in figure 6.3(b), using DAS beamformer, for different types of coherence-based methods. All images are displayed with a dynamic range of 60 dB.	102

LIST OF FIGURES

6.9	Ultrasound images of the wire-targets phantom shown in figure 6.3(b), using DAS beamformer and CPWI, for different types of coherence-based methods. All images are displayed with a dynamic range of 60 dB.	103
6.10	Ultrasound images of the wire-targets phantom shown in figure 6.3(b), using MV beamformer, for different types of coherence-based methods. All images are displayed with a dynamic range of 60 dB.	104
6.11	Ultrasound images of the wire-targets phantom shown in figure 6.3(b), using MV beamformer and CPWI, for different types of coherence-based methods. All images are displayed with a dynamic range of 60 dB. . .	105
6.12	The value of CNR achieved from the implemented types of coherence-based factors when used with four different types of beamforming methods.	110
6.13	The value of $SSNR_{Bg}$ achieved from the implemented types of coherence-based factors when used with four different types of beamforming methods.	111
6.14	The FWHM achieved from the implemented types of coherence-based factors when used with four different types of beamforming methods. .	112
6.15	The value of $SSNR_{BBR}$ achieved from the implemented types of coherence-based factors when used with four different types of beamforming methods.	113
7.1	Explaining the principle of ESBMV, where the signal subspace and noise subspace matrices are found depending on a threshold of λ_{th} after Eigendecomposing the covariance matrix of MV into Eigenvalues and Eigenvectors.	122

LIST OF FIGURES

7.2 The value of N_{sig} , or the number of eigenvectors included in the signal subspace matrix E_s , using reference ESBMV at $\delta=0.2$. (a) and (c) show the two phantoms for which, N_{sig} is displayed in (b) and (d) using a subarray length of 32. Therefore, the colour bars that indicate the values of N_{sig} to the left of the figure are between 1 and 32. (a) is a wire phantom with 5 wires and an 8mm diameter lesion centred at the 36mm depth. The two 6x4mm black squares to the sides of the lesion indicate the area for which, BBR artefacts are assessed using $SSNR_{BBR}$. (c) is a cyst phantom with a 3mm diameter cyst centred at the 18mm depth. The three 2x2 white squares to the left of the cyst are the background areas for which, CR and CNR are measured, while the 10x10mm black square is used to assess the homogeneity of the background speckle using $SSNR_{Bg}$ 124

7.3 Flow charts that explain the steps followed during the beamforming operation after calculating the MV weighting vector and covariance matrix using: (a) ESBMV and (b) PESBMV. 125

7.4 Ultrasound images of the experimental RF-data of the wire phantom shown in figure 7.2(a) using: (a) DAS (b) MV (c) CF-MV (d) ESBMV ($\delta = 0.2$) (e) ESBMV ($\delta = 0.4$) (f) PESBMV ($\delta = 0.2, \eta = 0.65$) (g) PESBMV ($\delta = 0.4, \eta = 0.35$). All images are displayed with a dynamic range of 50dB. 129

7.5 Ultrasound images of the experimental RF-data of cyst phantom shown in figure 7.2(c) using: (a) DAS (b) MV (c) CF-MV (d) ESBMV ($\delta = 0.2$) (e) ESBMV ($\delta = 0.4$) (f) PESBMV ($\delta = 0.2, \eta = 0.65$) (g) PESBMV ($\delta = 0.4, \eta = 0.35$). All images are displayed with a dynamic range of 50dB. 130

7.6 Ultrasound images of the experimental RF-data of the wire phantom shown in figure 7.2(a) using CPWI with: (a) DAS (b) MV (c) CF-MV (d) ESBMV ($\delta = 0.2$) (e) ESBMV ($\delta = 0.4$) (f) PESBMV ($\delta = 0.2, \eta = 0.65$) (g) PESBMV ($\delta = 0.4, \eta = 0.35$). All images are displayed with a dynamic range of 50dB. 133

LIST OF FIGURES

- 7.7 Ultrasound images of the experimental RF-data of cyst phantom shown in figure 7.2(c) using CPWI with: (a) DAS (b) MV (c) CF-MV (d) ESBMV ($\delta = 0.2$) (e) ESBMV ($\delta = 0.4$) (f) PESBMV ($\delta = 0.2, \eta = 0.65$) (g) PESBMV ($\delta = 0.4, \eta = 0.35$). All images are displayed with a dynamic range of 50dB. 134
- 7.8 Ultrasound images of a human carotid RF-data using: (a) DAS (b) MV (c) CF-MV (d) ESBMV ($\delta=0.3$) (e) PESBMV ($\delta=0.3,\eta=0.3$) (f) PESBMV ($\delta=0.3,\eta=0.4$). Three types of imaging objects are indicated by the circles A, B and C: (A) represents a hypoechoic area, (B) represents a BBR area and (C) contains a deep homogeneous tissue. All images are displayed with a dynamic range of 50 dB. 138
- 1 The RF data received by element #64 when imaging the wire phantom with 7 scattering points shown in figure 4.3 with 0° steering angle. . . 150

List of Tables

3.1	<i>THE PARAMETERS OF THE ULTRASOUND SYSTEM USED DURING THE SIMULATION STUDY.</i>	32
3.2	<i>THE RELATIONSHIP BETWEEN LATERAL AND AXIAL RESOLUTIONS AND THE STUDIED IMAGING PARAMETERS.</i>	39
5.1	<i>THE SIZES OF THE VARIABLES USED DURING THE MV BEAMFORMING OPERATION.</i>	69
5.2	<i>FWHM AND PSLR FOR THE POINT LOCATED AT THE 40mm DEPTH, FOR THE BEAMFORMERS SHOWN IN FIGURE 5.3.</i>	81
5.3	<i>FWHM AND PSLR FOR THE POINT LOCATED AT THE 40mm DEPTH IN THE PRESENCE OF DIFFERENT AMOUNTS OF DIAGONAL LOADING, FOR THE BEAMFORMERS SHOWN IN FIGURE 5.6.</i>	81
6.1	<i>CONTRAST AND SPECKLE STATISTICS MEASUREMENTS FOR THE CYST PHANTOM SHOWN IN FIGURE 6.3(a) FOR DIFFERENT COHERENCE-BASED FACTORS WHEN USED WITH DAS BEAMFORMER.</i>	106
6.2	<i>CONTRAST AND SPECKLE STATISTICS MEASUREMENTS FOR THE CYST PHANTOM SHOWN IN FIGURE 6.3(a) FOR DIFFERENT COHERENCE-BASED FACTORS WHEN USED WITH MV BEAMFORMER.</i>	107

LIST OF TABLES

6.3	<i>RESOLUTION AND BLACK-BOX REGION MEASUREMENTS FOR THE WIRE PHANTOM SHOWN IN FIGURE 6.3(b) FOR DIFFERENT COHERENCE-BASED FACTORS WHEN USED WITH DAS BEAMFORMER.</i>	108
6.4	<i>RESOLUTION AND BLACK-BOX REGION MEASUREMENTS FOR THE WIRE PHANTOM SHOWN IN FIGURE 6.3(b) FOR DIFFERENT COHERENCE-BASED FACTORS WHEN USED WITH MV BEAMFORMER.</i>	109
6.5	<i>THE COMPUTATIONAL COMPLEXITY OF THE IMPLEMENTED COHERENCE-BASED FACTORS.</i>	114
7.1	<i>RESOLUTION AND BLACK-BOX REGION MEASUREMENTS FOR THE WIRE PHANTOM USING DIFFERENT BEAMFORMING METHODS WITH PWL.</i>	131
7.2	<i>CONTRAST AND SPECKLE STATISTICS MEASUREMENTS FOR THE CYST PHANTOM USING DIFFERENT BEAMFORMING METHODS WITH PWL.</i>	131
7.3	<i>RESOLUTION AND BLACK-BOX REGION MEASUREMENTS FOR THE WIRE PHANTOM USING DIFFERENT BEAMFORMING METHODS WITH 5-ANGLES CPWL.</i>	135
7.4	<i>CONTRAST AND SPECKLE STATISTICS MEASUREMENTS FOR THE CYST PHANTOM USING DIFFERENT BEAMFORMING METHODS WITH 5-ANGLES CPWL.</i>	135

Abbreviations

AF	Array Factor
AR	Angular Range
ARFI	Acoustic Radiation Force Impulse
BBR	Black Box Regions
BW	Bandwidth
CF	Coherence Factor
CNR	Contrast-to-Noise Ratio
CPWI	Compound Plane-Wave Imaging
CR	Contrast Ratio
DAS	Delay-And-Sum
DM	Directivity Masking
ESBMV	Eigenspace-Based Minimum Variance
FR	Frame Rate
FWHM	Full Width at Half Maximum
GCF	Generalized Coherence Factor
HRCF	High Resolution Coherence Factor
MV	Minimum Variance
PA	Photoacoustic
PCF	Phase Coherence Factor
PESBMV	Partial Eigenspace-Based Minimum Variance
PSF	Point Spread Function
PSLL	Peak Sidelobe level
PWI	Plane-Wave Imaging
S	Transducer sensitivity

LIST OF TABLES

ScCF	Scaled Coherence Factor
SCF	Sign Coherence Factor
SNR	Signal-to-Noise Ratio
SSNR	Speckle Signal-to-Noise Ratio
SSI	Supersonic Shear Imaging
StS-CF	Spatio-Temporally Smoothed Coherence Factor
UARP	Ultrasonic Array Research Platform

List of Symbols

A	The number of elements in the aperture
A_t	The medium attenuation
$b(k)$	A vector containing the sign bits of a signal
B/A	Nonlinearity coefficient
c	Sound speed
d	The elements centre-to-centre distance
d_x	Lateral step size
d_z	Axial step size
e	Steering vector
E_n	Noise subspace matrix
E_s	Signal subspace matrix
$f_{\#}$	F number
f_0	Central frequency
f_s	Sampling frequency
G_p	The p^{th} subarray
H_{Wiener}	The transfer function of Wiener postfilter
I	Identity matrix
I_{AR}	The minimum distinguishable intensity at the angular range
k	The wave number
K	Temporal averaging coefficient
L_p	Subarray length in spatial smoothing operation
M_0	The cutoff frequency
N	The total number of elements in the transducer
N_A	The number of compounded angles
N_m	The number of averaged focused images
N_{sl}	The number of scan lines

N_{sig}	The number of columns in the signal subspace matrix
P	The number of subarrays
$p(x, z)$	The value of the point located at (x, z) in the image
P_0	The transmitted pressure
P_n	Noise power
P_s	Signal power
R	Covariance Matrix
R_{ax}	Axial Resolution
R_{lat}	Lateral Resolution
R_p	Noise covariance matrix
S	Transducer sensitivity
T_j	The value received by the j^{th} element
τ_j	The sum of the transmit and receive times to and from the focal point
t_{rc}	The receive time from the focal point
T_{sl}	The time between the transmit and receive for a scan line
t_{tr}	The transmit time to the focal point
w	The weighting vector
W_{ESBMV}	The weighting vector of ESBMV
W_{PESBMV}	The weighting vector of PESBMV
W_t	The total width of the transducer
x	Lateral distance
x_j	The lateral distance of the j^{th} element
$x_m(n)$	The signal received by the m^{th} element
$X(k)$	A signal in the discrete frequency domain
Y	Beamformer output
Y_{CF}	Coherence Factor-weighted output
z	Axial distance
Z	The maximum imaging depth
Z_f	Focal depth
β_n	The pulsing delay time of the n^{th} element
$\eta(SNR)$	The adaptive coefficient controlling scCF
θ	The steering angle
λ	The wavelength
λ_i	The i^{th} eigenvalue of the covariance matrix
λ_{th}	A threshold that controls the value of N_{sig}

ψ	The relative phase between the elements
σ_s	The shock parameter
ρ_0	Medium density
μ	Mean value
σ	Standard deviation
δ	ESBMV coefficient
η	PESBMV coefficient
\mathbb{V}	A matrix contains the eigenvectors of the covariance matrix
$\mathbb{\Lambda}$	Diagonal matrix whose diagonal is the eigenvalues of the covariance matrix

Chapter 1

Introduction

Plane Wave Imaging (PWI) is the technique where a complete ultrasound image is produced with a single transmission and reception using multi-element array transducers. It is mainly used to produce Brightness or B-mode images in ultrahigh frame rates of up to thousands frames per second. B-mode images are 2-dimensional grey scale images that are considered as the standard display method in diagnostic ultrasound imaging (Bui & Taira, 2009). B-mode images use the brightness to reveal the size and amount of reflectivity of the objects in the imaging region, depending on the time and amplitude of the received ultrasound echo. The operation of producing an image out of the received ultrasound echo signals from each element of an array is referred to as the Beamforming operation. This operation is the most important step that helps reveal the required information carried by the reflected echo signals, and without it, the ultrasound imaging operation has no useful meaning.

PWI produces a much higher frame rate than traditional linear scanning. This high frame rate is crucial for flow measurements and in determining the elasticity of tissue. The lack of focusing in transmit leads to low image quality, however this can be compensated in receive processing. Due to the importance of PWI for ultrafast ultrasound imaging applications, attention has turned towards improving the beamforming operation to compensate for the quality loss in PWI. Different techniques such as Compound Plane-Wave Imaging, adaptive beamforming, Coherence-based factors and Eigenspace-Based adaptive beamforming, were investigated recently by different research groups to produce high quality

ultrasound images without losing the high frame rate provided through the use of plane waves.

1.1 Literature Review

In medical imaging and during the last 40 years, the field of ultrasound imaging has gained a lot of interest, due to its properties of being non-invasive, cheap, repeatable, easy-to-use, non-ionizing and able to display flow information (Meola *et al.*, 2016). The use of ultrasound for imaging emerged in the 1960s, while multichannel transducers with electronical steering and focusing were developed for medical imaging purposes in the 1970s (Bercoff, 2011). Developing this type of transducer introduced the idea of fast imaging which enabled different types of medical imaging applications like tracking the motion of cardiac valves and blood flow estimation. Meanwhile, compounding multiple steered plane waves was produced and discussed as a method for providing a better quality for ultrafast imaging (Berson *et al.*, 1981; Delannoy *et al.*, 1979; Kossoff *et al.*, 1976). Since then, the field of ultrafast ultrasound imaging has witnessed the rise and growth of different types of applications that became of great importance in the diagnostic imaging. Examples of these applications are shear wave imaging (Bercoff *et al.*, 2004), strain imaging (Park *et al.*, 2007), Doppler flow imaging (Bercoff *et al.*, 2011) and contrast enhanced microbubble imaging (Couture *et al.*, 2012).

Due to the importance of the compounding operation for improving the quality of plane wave imaging, several researchers have investigated the effect of the selected number of angles and angular range on the produced imaging quality (Montaldo *et al.*, 2009; Wilhjelm *et al.*, 2004). However, these studies did not give a direct method for this selection, where a minimized number of angles within the suitable angular range must be used to preserve the frame rate. In addition, no study could explain the relationship between the compounding angles and spatial resolution.

Another way to improve the quality of ultrasound imaging is the use of adaptive beamforming. Since it was first introduced by Capon (1969), the Minimum Variance adaptive beamformer (MV) has gained a lot of interest in the field of ultrasound imaging, due to its ability to improve the produced quality through

the use of data-dependent weighting. In the last few years, MV was widely investigated for different types of medical ultrasound imaging applications; [Van Veen *et al.* \(1997\)](#) used the MV principle to produce a spatial filter for localizing the sources of the electrical activities of the human brain. In 2002, the MV beamformer performance was experimentally investigated on a cyst phantom ([Mann & Walker, 2002](#)), while in 2005, it was used for imaging a cystic phantom, heart phantom and the RF data of a rat mammary tumour ([Wang *et al.*, 2005](#)).

When combined with MV adaptive beamformer, the compounding operation becomes highly efficient and requires less angles to achieve a specific level of imaging quality. [Austeng *et al.* \(2011\)](#) in a simulation study showed that a three-fold increase in the frame rate can be achieved when using MV instead of DAS beamformer with CPWI.

Since it was first introduced for measuring the focusing quality by [Hollman *et al.* \(1999\)](#), the Coherence Factor (CF) was widely used for weighting the output of DAS and MV beamformers, where the resolution and sidelobe reduction are improved significantly. However, the dependence on the degree of coherency of the received signals at the focal point when calculating the CF results in destroying the speckle homogeneity due to being highly incoherent. Another drawback arises with the CF is the Black Box Regions (BBR), which are black areas that appear to the sides of any strong scattering object embedded in a speckle generating background. The Generalized Coherence Factor (GCF) is another way to weight the beamformer output with having the ability to maintain the homogeneity of the background speckle at the cost of reduced contrast ([Li & Li, 2003](#)). The High Resolution Coherence Factor (HRCF) uses the MV output instead of the coherent sum of the received signals to produce a more precise type of coherence weighting, where a better speckle homogeneity is created with lower BBR artefacts, compared to conventional CF ([Wang & Li, 2009](#)). A simple form of CF is the Sign Coherence Factor (SCF) produced by [Camacho *et al.* \(2009\)](#). SCF depends on the sign of the received signals to calculate the weighting value. Both the speckle homogeneity and the BBR reduction are improved at the cost of reduced contrast. The Spatio-temporal Smoothed Coherence Factor (StS-CF) was introduced in 2014 to solve the problem of BBR using temporal and spatial smoothing operations, at the cost of reduced contrast ([Xu *et al.*, 2014](#)).

In the Scaled Coherence Factor produced by Wang & Li (2014), a factor that ranges between the CF and 1, depending on the SNR, is used for weighting the beamformer output. One drawback is related to this method, is that the level of SNR is usually similar in both the BBR and the cystic areas, so that both the contrast and BBR are improved or reduced simultaneously.

The method of Eigenspace-Based Minimum Variance (ESBMV) which uses the Eigen decomposition to modify the weighting vector of MV, has the ability to reduce the sidelobes level and improve both contrast and resolution. It was first introduced by Van Veen (1988) and was widely used afterwards for various ultrasound imaging applications (Lee & Lee, 1997; Mehdizadeh *et al.*, 2012a; Sekihara *et al.*, 2002). Two types of artefacts usually occur when using ESBMV for medical imaging, the first type is the BBR artefacts, and the second is the dark spots that appear in the background speckle. Aliabadi *et al.* (2015) proposed a new ESBMV method that amends the value of the focal point depending on the echo signals received by the surrounding points. This method was able to improve contrast by reducing dark spots, but failed to eliminate BBR artefacts. Zhao *et al.* (2016) used a compensated subspace scheme to reduce BBR artefacts. In this method, the user iteratively decreases the size of the signal subspace whenever BBR artefacts occur in the image until these artefacts are eliminated, at the cost of reducing both contrast and resolution. Therefore, it can be said that no method in the literature has managed to totally eliminate the problem of these artefacts that appear in ESBMV.

1.2 Motivation

Ultrafast frame rates are essential for many ultrasound imaging applications where images are required to be obtained in microseconds. This is due to the need to capture the motion of a specific target such as capturing the heart beats during the cardiac cycle, detecting the blood flow velocity and tracking the propagation of shear waves in Elastography (Macé *et al.*, 2011; Montaldo *et al.*, 2009). Reaching ultrahigh frame rates of thousands frames per second is not possible without the use of Plane Wave Imaging (PWI). Despite the fact that it has been widely used in different fields of ultrasound imaging, there is still no specific formula

that can be used in estimating spatial resolution when the system parameters are known. This is unlike conventional linear imaging, where the resolution has a formula for each type of transducer.

Due to the lack of focusing in PWI and the use of a single transmitted pulse for imaging the whole region of interest, a reduced imaging quality in terms of resolution, sidelobe levels and contrast is usually produced. Therefore, research has turned towards compensating for this quality loss through developing and/or combining different types of advanced beamforming techniques, each of which, however, has its own benefits and drawbacks.

One of the most popular techniques for improving PWI quality is the Compound Plane-Wave Imaging (CPWI). [Bercoff \(2011\)](#) demonstrated the lowest frame rates required for capturing the shear wave propagation in human tissue. To preserve these frame rates, no more than 3, 5 and 15 frames can be compounded during abdominal, cardiac and breast imaging, respectively, when using CPWI. However, the random selection of the compounded angles leads to the need to compound a large number of frames to reach the required imaging quality, and this prevents the ability to use CPWI in many ultrafast imaging applications. Therefore, a clear method that calculates the optimum steering angles is required so that the best possible imaging quality is achieved using the minimum number of compounded frames.

The use of MV adaptive beamformer is another recent technique to improve the imaging quality in PWI, where a high resolution imaging and reduced sidelobe levels compared to conventional DAS beamformer can be achieved. This is suitable for point targets imaging. However, three disadvantages or drawbacks occur with this type of beamforming; the first drawback is the low robustness that can be decreased at the expense of sacrificing resolution. Secondly, the high computational complexity of this method compared to the conventional beamformer of DAS. In the literature, several research groups have recently introduced various schemes that help to overcome these two limitations ([Asl & Mahloojifar, 2012](#); [Holfort *et al.*, 2008a](#)).

The other drawback of MV which is addressed in the second part of this research is producing a low contrast which is very near to that produced by DAS. This is because of its failure in resolving cystic targets, which results in a low

1.3 The Objectives and Organization of the Thesis

quality medical ultrasound imaging. Weighting the beamformer output using the Coherence Factor (CF) is one method that can be used for improving the imaging quality of any type of beamformers including MV. By depending on the amount of coherency of the received RF signals, the CF can improve the resolution, contrast and sidelobe reduction. The speckle statistics, however, are highly distorted due to being highly incoherent, in addition to the BBR that appear to the sides of any hyperechoic lesion, leading to a low quality medical ultrasound imaging.

Another method for improving the imaging quality of MV and is recently widely investigated by research groups is the Eigenspace-Based Minimum Variance (ESBMV). By projecting the MV weighting vector to the signal subspace matrix, any off-axis signal as well as noise is rejected, leading to high resolution and contrast, whilst preserving the homogeneity of the background speckle. However, dark spots as well as BBR to the sides of the hyperechoic objects usually occur in the background speckle when using this beamformer. Under-estimating the size of the signal subspace matrix helps improving both the resolution and contrast, but results in increasing the problem of BBR and dark spots. The occurrence of these two types of artefacts makes it unsuitable to use ESBMV for medical imaging where hyperechoic objects widely exist, such as bones, stones, deep fat, gas bubbles, cardiac valves and spleen.

1.3 The Objectives and Organization of the Thesis

Due to the growing popularity for ultrafast imaging applications that use unfocused plane waves, the need for a formula for assessing lateral resolution for this type of imaging has increased. After a detailed explanation of the background principle of PWI and CPWI in chapter 2 in this thesis, chapter 3 was dedicated for studying the imaging parameters that affect spatial resolution of unfocused PWI. This study results in an empirical expression that estimates the lateral resolution of PWI, which is found to be directly proportional to the transducer width and the transmitted wavelength, and inversely proportional to the imaging depth. This study was published in the following paper:

1.3 The Objectives and Organization of the Thesis

- Zainab Alomari, S. Harput, S. Hyder, and S. Freear, ” *The effect of the transducer parameters on spatial resolution in plane-wave imaging*”, in IEEE International Ultrasonics Symposium (IUS), 2015, pp. 1-4.

Improving the imaging quality of unfocused imaging using CPWI is accompanied with a reduction in the frame rate that is directly proportional to the number of compounded signals. When using CPWI for ultrafast imaging applications, such as shear wave imaging that requires a minimum of 1000 to 4000 frames per second (Bercoff, 2011), the required imaging quality needs to be achieved using the minimum possible number of compounded signals. This requires knowing the effect of the number and values of the compounding angles on spatial resolution and sidelobes level, to help choosing the suitable angles for steering. Chapter 4 in this thesis introduces a new method to specify the angular range within which the steering angles should be selected. In addition, this chapter shows the relation between the angular step and the spatial resolution and sidelobes level. Knowing these two pieces of information makes it very easy to select the suitable steering angles for CPWI, without the need to iteratively compound different combinations of steered signals. This study was published in the following paper:

- Zainab Alomari, S. Harput, S. Hyder, and S. Freear, ” *Selecting the number and values of the CPWI steering angles and the effect of that on imaging quality*”, in IEEE International Ultrasonics Symposium (IUS), 2014, pp. 1191-1194.

The use of adaptive beamforming is another way to improve the quality of PWI by using data-dependent weighting instead of fixed weighting during the beamforming. MV adaptive beamformer uses both temporal and spatial smoothing operations to enhance the resolution and speckle homogeneity. However, some techniques, like the coherence-based factors and Eigenspace-Based Minimum Variance (ESBMV), were recently developed in order to improve the low contrast of this beamformer. Part II of this thesis is dedicated for the MV beamformer and these techniques, where in chapter 5, a detailed explanation is given for the background method and properties of MV beamformer. Chapter 6 compares the different types of coherence-based factors and explains the advantages

1.3 The Objectives and Organization of the Thesis

and drawbacks of each of them through the use of experimental RF data of a cystic and wire phantoms. Finally, chapter 7 explains the principle of ESBMV and gives a solution for the BBR artefacts that occur to the sides of any hyperechoic object in the image when using this technique, through the use of a new method of Partial-ESBMV. This method defines the area at which the BBR artefacts occur, and then replaces the performance of ESBMV with the response from conventional MV. In this way, the technique becomes highly suitable for medical imaging applications, where hyperechoic objects widely appear. Examples on these objects include: bones, heart valves, gas bubbles and spleen. The work introduced in chapter 7 will be published in the following paper:

- Zainab Alomari, S. Harput, D. M. Cowell, Asraf Moubark and S. Freear, ” *Partial eigenspace-based minimum variance (PESBMV) beamforming for medical ultrasound imaging*”, IEEE Transactions on Ultrasonics, Ferroelectrics, and Frequency Control, (Manuscript is currently under review).

The search carried out in this thesis has contributed to the work presented in four papers submitted by students in the Ultrasound Group, and were not included in this thesis. These papers were all published in the IEEE International Ultrasonics Symposium (IUS) as follows:

- A. Moubark, Zainab Alomari, S. Harput and S. Freear, ” *Comparison of spatial and temporal averaging on ultrafast imaging in presence of quantization errors*”, in IEEE International Ultrasonics Symposium (IUS), 2015, pp. 1-4.
- A. Moubark, Zainab Alomari, S. Harput and S. Freear, ” *Enhancement of contrast and resolution of B-mode plane wave imaging (PWI) with non-linear filtered delay multiply and sum (FDMAS) beamforming*”, in IEEE International Ultrasonics Symposium (IUS), 2016, pp. 1-4.
- S. Hyder, S. Harput, Zainab Alomari and S. Freear, ” *Two-way quality assessment approach for tumour detection using free-hand strain imaging*”, in IEEE International Ultrasonics Symposium (IUS), 2014, pp. 1853-1856.

1.3 The Objectives and Organization of the Thesis

- S. Hyder, S. Harput, Zainab Alomari, D. M. J. Cowell, J. McLaughlan and S. Freear, ” *Improved shear wave-front reconstruction method by aligning imaging beam angles with shear-wave polarization: Applied for shear compounding application*”, in IEEE International Ultrasonics Symposium (IUS), 2016, pp. 1-4.

Part I

The Properties of Ultrafast Ultrasound Imaging Techniques

Chapter 2

Ultrasound Imaging Techniques

The presence of linear array transducers that consist of multiple elements arranged in straight rows provides the ability to produce different combinations of steered and/or focused emitted beams (Cobbold, 2007; Schäberle, 2010). This is achieved by controlling the pulsing operation of these elements using specific timing patterns.

This chapter discusses the background method and properties of the three imaging techniques that are produced using linear arrays and used during the work of this thesis. These techniques are the linear imaging, Plane-Wave Imaging (PWI) and Compound Plane-Wave Imaging (CPWI).

2.1 Linear Imaging

In linear imaging, each line of data, which is called a scan line, is produced by pulsing a group of the transducer elements to produce a single focused beam. This group of elements is called the aperture, and it is used to receive the echo signals that enter the beamforming operation to produce a single scan line. The aperture is then shifted by one element and the pulsing is repeated to produce another scan line. This operation is repeated $(N - A + 1)$ times and it produces $(N - A + 1)$ scan lines, where N is the number of the transducer elements and A is the number of elements in the aperture.

The final image is the result of gathering the scan lines in a single matrix, performing the envelope detection using Hilbert transform, and finally converting

the result to dB. Converting into dB scale is done because this scale has the ability to represent both very small and very large quantities of gain into a convenient figure (Bhargava & Kulshreshtha, 1984).

The frame rate in linear array imaging is affected by the maximum imaging depth and the number of scan lines. It is calculated from (Bercoff, 2011):

$$FR_{LinearImaging} = \frac{1}{N_{sl} \cdot T_{sl}}, \quad (2.1)$$

where FR is the frame rate and N_{sl} is the number of scan lines. T_{sl} is the time between transmitting the beam and receiving the backscattered echoes for each scan line, and it is calculated by:

$$T_{sl} = \frac{2Z}{c}, \quad (2.2)$$

where Z is the maximum imaging depth and c is the speed of sound in the imaging medium. The operation of processing the received echoes to produce the final image is called the beamforming operation and it varies from one imaging technique to another.

Increasing the aperture size helps in improving the lateral resolution of the image. This is because both of the beam width at the focal depth and the beam divergence angle are inversely proportional to the aperture width (Schickert *et al.*, 2003). The noise level is also related to the width of the aperture. This is because larger aperture provides more data to be beamformed and this helps in decreasing noise. However, the width of the resulted image is inversely proportional to the aperture size, where using larger apertures decreases the number of scan lines and thus the width of the imaging is decreased. Therefore, in linear imaging, a trade-off between the imaging quality and the width of the resulted image should be considered.

In order to improve the resolution and reduce noise level in linear imaging, multiple images with different focal depths are produced for the region of interest and then they are combined together (Montaldo *et al.*, 2009). This technique is called Multifocus imaging. The improvement in the imaging quality achieved with this technique comes at the cost of reducing the frame rate, which will be calculated as follows:

$$FR_{Multifocus} = \frac{FR_{LinearImaging}}{N_m}, \quad (2.3)$$

where N_m is the number of averaged focused images and $FR_{LinearImaging}$ is the frame rate of a single focused image, calculated from equation (2.1).

2.2 Plane Wave Imaging (PWI)

Plane Wave Imaging (PWI) is the type of imaging that uses a single unfocused beam to view the imaging region. While a single transmission in linear imaging yields a single scan line, PWI produces a whole image with a single transmission. Therefore, PWI can have a high frame rate that equals to the linear imaging frame rate multiplied by the number of scan lines, and it is usually several thousands frames per second (Bercoff, 2011).

$$FR_{PWI} = \frac{1}{T_{sl}}. \quad (2.4)$$

Thus, PWI can provide a frame rate that is independent on the number of the produced data lines for the required imaging width.

The implementation of PWI requires following the same steps used in linear imaging implementation with two differences; first, the ultrasound beam is unfocused in PWI. This can be achieved by setting the focal point to a large number which ideally equals to infinity. Secondly, the imaging is performed using all the transducer elements as transmitters and receivers instead of using part of them as the aperture.

In order to form a single frame in PWI, all the elements in the transducer are pulsed in the same time and then used to receive the echoes reflected from the field points. This is unlike linear imaging which pulses only the elements in the aperture each time. In order to form a frame out of these received echoes during the beamforming operation, dynamic focusing is performed. Dynamic focusing is the operation of delaying the signal received by each receiving element with a delay equal to the time required by the signal to reach the required point and be reflected back to the receiver. This means that the focusing of the transducer is changed dynamically with each focal point (Cobbold, 2007).

2.2 Plane Wave Imaging (PWI)

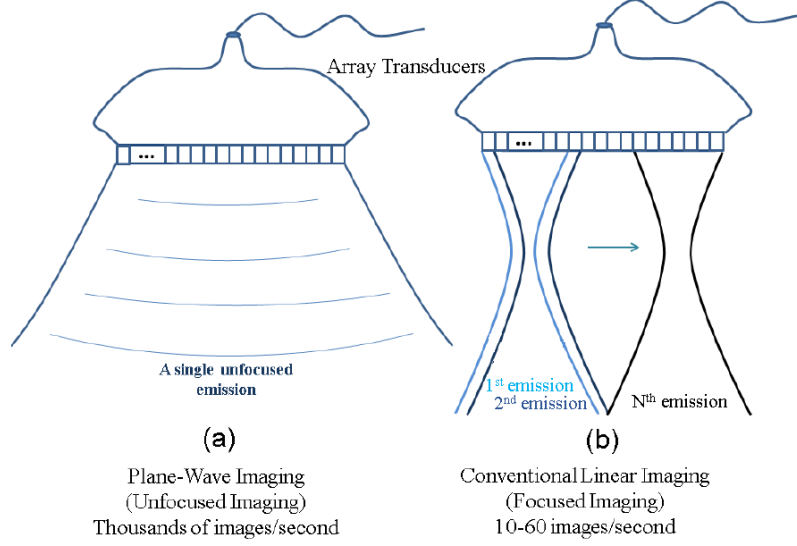


Figure 2.1: A schematic diagram for the transmitted ultrasound beam in: (a) PWI and (b) Linear Imaging.

The value of each focal point in the final image is the result of averaging the values received by all the receiving elements from that point after delaying them by a specific value. This can be expressed mathematically by the following equation (Montaldo *et al.*, 2009):

$$p(x, z) = \sum_{j=1}^N T_j(t - \tau_j(x, z)), \quad (2.5)$$

where $p(x, z)$ is the value given to the point located at x in the lateral direction and z in the axial direction, N is the total number of receiving elements and $T_j(t)$ is the value received by the j^{th} receiving element. $\tau(x, z)$ is the total time taken by the signal to travel from the transmitter to the field point and then back to receiver j , as in the following equation (Montaldo *et al.*, 2009):

$$\tau_j(x, z) = t_{tr} + t_{rc}, \quad (2.6)$$

where t_{tr} and t_{rc} are the transmit and receive times to and from the focal point,

2.3 Compound Plane-Wave Imaging (CPWI)

respectively, and they are calculated as follows:

$$t_{tr} = \frac{z}{c} \quad (2.7)$$

$$t_{rc} = \frac{\sqrt{z^2 + (x_j - x)^2}}{c}, \quad (2.8)$$

where x_j is the lateral distance of the j^{th} receiving element.

The beamforming operation that sums the delayed RF signals as in equation (2.5) is called the Delay-And-Sum (DAS) beamforming, and it is widely used in medical ultrasound imaging (Synnevag *et al.*, 2007).

Many applications become possible when ultrahigh frame rate imaging is provided. However, PWI cannot be used with many of these applications due to the absences of focusing which usually yields low quality images in terms of spatial resolution, contrast and level of artefacts (Holfort *et al.*, 2008b). The imaging quality in PWI can be improved either by averaging multiple plane wave images together, or by using data-dependent adaptive beamforming.

2.3 Compound Plane-Wave Imaging (CPWI)

In order to improve the imaging quality in PWI while preserving the high frame rate, CPWI is produced. Rather than forming the image with a single transmission in PWI, CPWI produces an image by compounding or averaging multiple images, each of which is produced by steering the unfocused beam with a specific angle. These frames are beamformed separately before being compounded. The compounding operation that produces the final image can be achieved using either coherent or incoherent compounding method.

The frame rate achieved in CPWI is the frame rate required for each individual frame, divided by the number of compounded angles:

$$FR_{CPWI} = \frac{FR_{PWI}}{N_A}, \quad (2.9)$$

where N_A is the number of compounded angles and FR_{PWI} is given in equation (2.4). It can be seen from this equation that the frame rate in CPWI is inversely proportional to the number of compounded angles. This frame rate is suitable for

2.3 Compound Plane-Wave Imaging (CPWI)

ultrafast imaging applications up to a specific limit of angles. After this limit, the frame rate reduction becomes unsuitable for these applications. In addition, the tissue motion will start to have an observable effect on the quality of the produced images (Papadacci *et al.*, 2014). The maximum number of compounded angles can be estimated depending on the imaging depth, speed of sound and the amount of tissue motion in the region of interest.

2.3.1 The Steering Operation

The steering operation can be achieved using multi-element linear array transducers by pulsing each element separately, with a constant time delay between the pulses. This is shown in figure 2.2, where small steering angles are produced by decreasing the delay time between pulses.

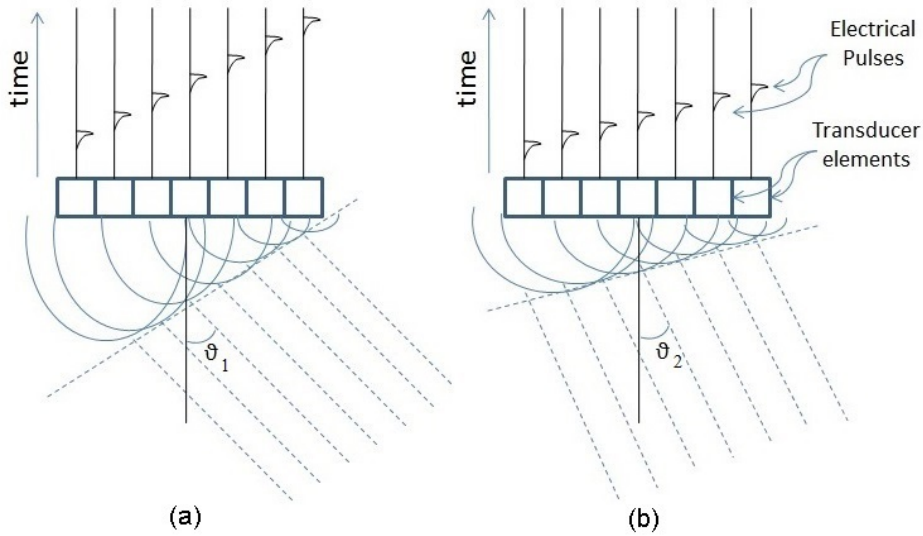


Figure 2.2: A schematic diagram shows the steering operation of ultrasound beams using linear arrays. Steering is achieved by pulsing the transducer elements with two different amounts of fixed delays to steer with angles: (a) θ_1 and (b) θ_2 , where $\theta_1 > \theta_2$.

For steering the beam with a specific angle, the amount of delay between the pulses can be calculated from the following equation (Cobbold, 2007):

2.3 Compound Plane-Wave Imaging (CPWI)

$$\beta_n = \frac{1}{c} \left[\sqrt{Z_f^2 + \frac{d^2(N-1)}{4}} + Z_f d \sin |\theta| (N-1) - \sqrt{Z_f^2 + (nd)^2 - 2nZ_f d \sin |\theta|} \right], \quad (2.10)$$

where d is the centre-to-centre distance, ϑ is the steering angle, Z_f is the focal depth and $-(N-1)/2 \leq n \leq (N-1)/2$. Equation (2.10) is used to calculate the amount of delay required to achieve both beam steering and focusing in the same time. This is usually required in phased array imaging that yields in sector-shape images (Gan, 2012). In order to calculate the time delays required to steer the beam without focusing, a big number is assigned to the focusing depth Z_f , which makes the delay equal to zero according to equation (2.10). In this case, the following equation can be used (Von Ramm & Smith, 1983):

$$\beta = \frac{d}{c} \sin \vartheta. \quad (2.11)$$

The steering operation is usually limited by the occurrence of the grating lobes. Grating lobes are weak replica of the main lobe and they occur due to the constructive interference in any multi-element array transducer that has regularly spaced elements (Sanders & Winter, 2007). They occur at the sides of the main beam with angles of up to 90° . The effect of the grating lobes can be minimized by setting the centre-to-centre distance between the transducer elements to one wavelength or less (Huang *et al.*, 2007).

When the beam is steered with a specific angle, the grating lobe which occurs at a constant angle becomes nearer to the line that is perpendicular to the transducer centre. Because of the apodization operation, this results in growing the grating lobe in amplitude at one side, while the amplitude of the grating lobe at the other side is weakened (Delchar, 1997; Leondes, 2007; Szabo, 2004). This increases with increasing the steering angle, as explained in figure 2.3.

The angle at which the grating lobes start to occur can be found by using the Array Factor (AF), which resembles the directivity pattern of the transducer array (Harput & Bozkurt, 2008). For any transducer with N elements, d centre-to-centre distance, θ steering angle and a wavelength of λ , the AF can be found from the following equation (Harput & Bozkurt, 2008):

2.3 Compound Plane-Wave Imaging (CPWI)

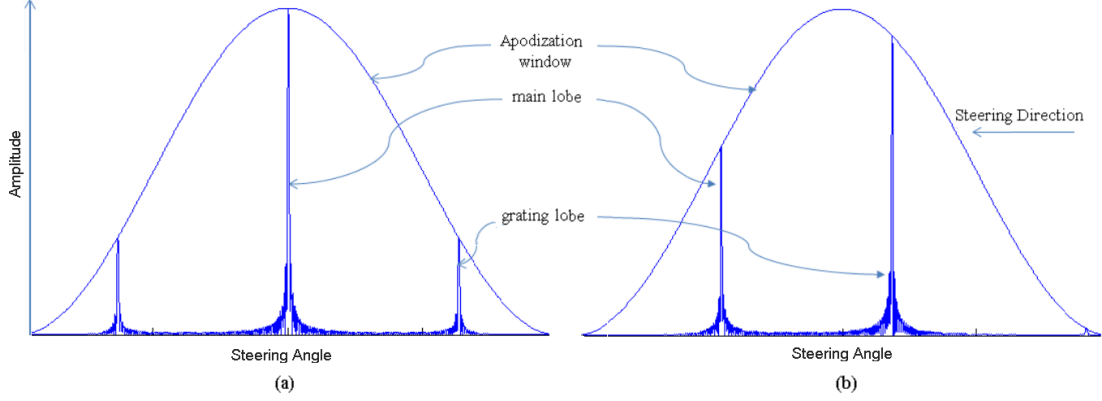


Figure 2.3: The role of the apodization in minimizing the effect of the grating lobes (a)without the steering (b)with the steering.

$$AF = \frac{1}{N} \left[\frac{\sin\left(\frac{N}{2}\psi\right)}{\sin\left(\frac{1}{2}\psi\right)} \right], \quad (2.12)$$

where ψ is the relative phase between the elements of the transducer and it is found as (Harput & Bozkurt, 2008):

$$\psi = kd \sin(\theta) + \beta, \quad (2.13)$$

where k is the wave number and it equals to $2\pi/\lambda$.

For the ultrasound imaging system used during the lab experiments in this thesis, the AF was calculated for the steering angles from 0 to 90°, using Matlab program (The Mathworks Inc., Natick, MA, USA). This is to specify the steering angles at which grating lobes occur. The result is shown in figure 2.4, where the lobe at the steering angle of 0° represents the main lobe. In this figure, the first grating lobe can be seen to occur at the angle of 66.7° from the main lobe. By steering with angles of less than this angle, the effect of grating lobes can be avoided. Thus the use of AF can be useful to specify the range within which it is possible to steer without introducing grating lobes into the image.

2.3.2 DAS Beamforming in CPWI

After transmitting the unfocused steered beam and receiving the echoes, the beamforming operation is performed. The DAS beamforming is performed in

2.3 Compound Plane-Wave Imaging (CPWI)

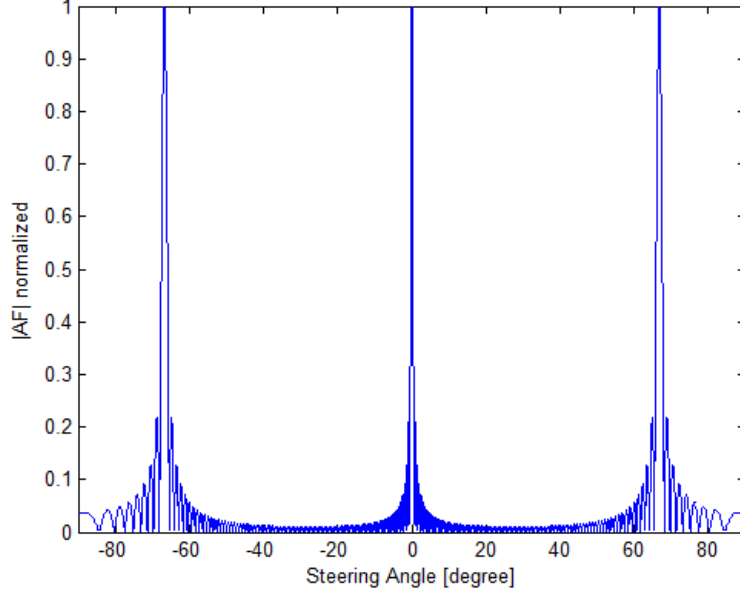


Figure 2.4: The Array Factor plot at different steering angles is used to show the angle at which grating lobes occur.

CPWI depending on equation (2.5) used to beamform a plane wave. The steering operation has the effect of changing the delay time between the transmitter and the field point t_{tr} . This is because of the delays added between the pulses during the pulsing operation to perform the steering, which can be simulated by steering the whole transducer with respect to the field point, as shown in figure 2.5. Therefore, the transmit delay t_{tr} used in equation (2.6) will be calculated as follows (Montaldo *et al.*, 2009):

$$t_{tr} = \frac{z \cos \theta + x \sin \theta}{c}. \quad (2.14)$$

This equation is derived from the equation of steering a point with an angle, considering that steering the transducer with an angle of θ is the same as steering the field point with $-\theta$. In equation (2.14), $x = 0$ is assumed to be at the edge of the transducer, while assuming it at the centre of the transducer changes the equation to (Korukonda, 2012):

$$t_{tr} = \frac{z \cos \theta + x \sin \theta + \frac{W_t}{2} \sin(|\theta|)}{c}, \quad (2.15)$$

2.3 Compound Plane-Wave Imaging (CPWI)

where W_t is the total width of the transducer. During this work, $x = 0$ is assumed to be at the centre of the transducer. The detailed derivation of equation (2.15) is given in the appendix.

As can be noticed from figure 2.5, the steering operation adds no change to the delay time between the field point and the receiver t_{rc} in PWI, which is given in equation (2.8).

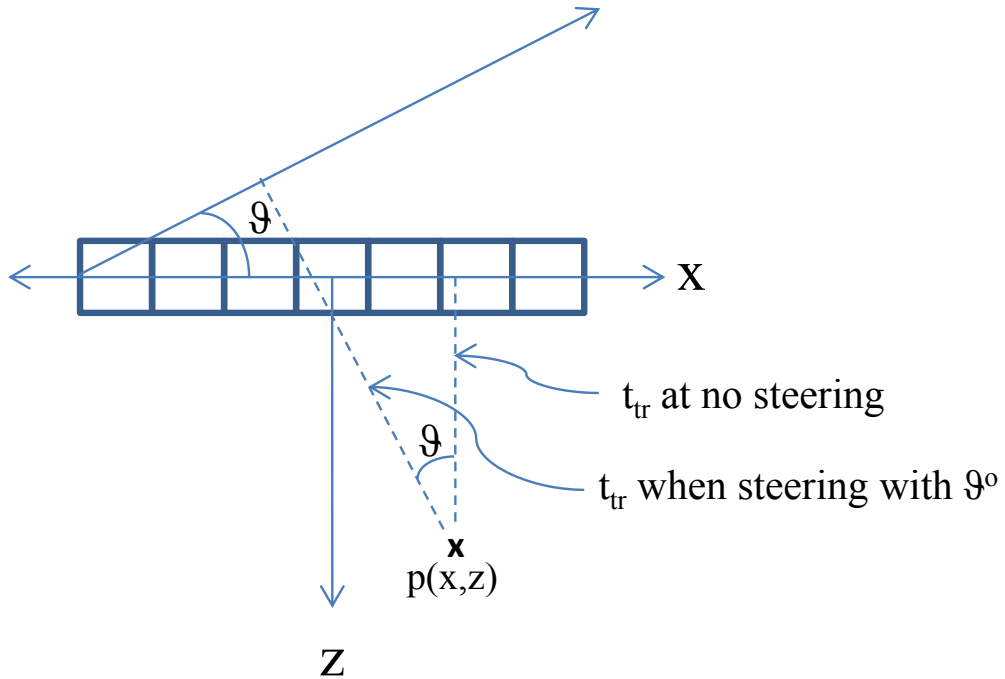


Figure 2.5: A schematic diagram for the effect of steering on the time t_{tr} required for the signal to travel from the transmitter to any field point $p(x, z)$.

2.3.3 Compounding Operation

In CPWI, the compounding operation is done after beamforming the data received from each angle separately. CPWI can be coherent or incoherent. In incoherent CPWI, the envelope detection is performed for each signal separately and then the signals are compounded, while in coherent CPWI, the beamformed signals are compounded and then the result is envelope detected (Montaldo *et al.*, 2009). The envelope detection operation is usually done using Hilbert transform, which gives a similar effect of squaring and low pass filtering a signal.

The main difference between coherent and incoherent CPWI is that the compounding operation that is performed in coherent CPWI before Hilbert transform helps diminishing the sidelobes, where destructive interference occur between incoherent signals. On the other hand, applying the envelope detection to each signal separately before the compounding operation in incoherent CPWI improves unwanted artefacts as it prevents destructive interference between incoherent signals. This difference is shown using Field II in figure 2.7, where both coherent and incoherent CPWI are implemented using the same number of compounded angles on the point model given in figure 2.6. The number of angles used during this simulation are from 3 to 11 with a step of 2, within the angular range of $\pm 7^\circ$. During the work of this thesis, the coherent type of CPWI is used.

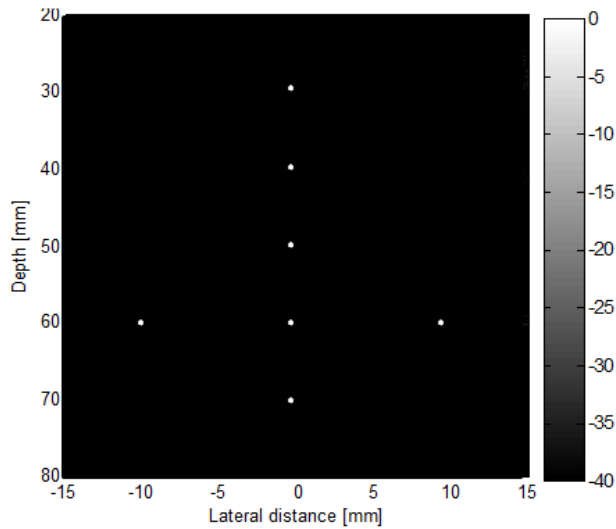


Figure 2.6: The scattering points model used during Field II simulations and laboratory experiments.

2.4 CPWI Properties

The properties of CPWI are widely investigated and discussed through the literature, due to the importance of this imaging technique for many types of appli-

2.4 CPWI Properties

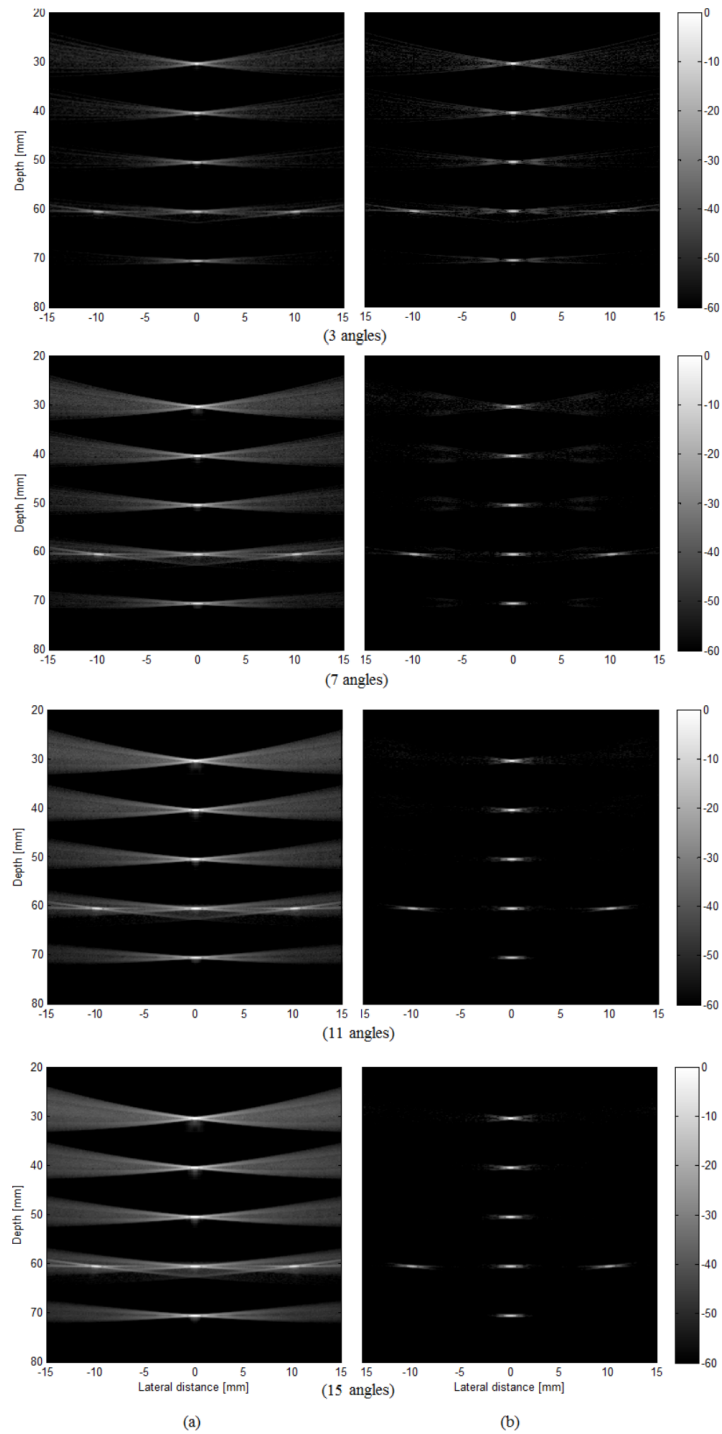


Figure 2.7: Field II simulations for the point targets phantom shown in figure 2.6, using: (a) incoherent and (b) coherent compounding, using different numbers of compounded angles within the $\pm 7^\circ$. All images are displayed with a dynamic range of 60 dB.

cations.

2.4.1 Advantages

In CPWI, ultrahigh frame rates can be achieved as only a single emission is required to produce a whole frame. In addition to this property, CPWI has the ability to reduce the imaging artefacts and sidelobes. This reduction is due to the averaging of multiple uncorrelated images for a single object, each is produced using a different transmit angle. The speckle reduction in CPWI results in improving contrast in soft tissues, which makes it suitable for tumour and lesion detection in the breast. Speckle reduction also contributes by providing a better delineation and border definition for lesions and cysts as compared to conventional linear imaging (Entrekin *et al.*, 2001; Huber *et al.*, 2002; Jespersen *et al.*, 2000; Opretzka *et al.*, 2011; Weinstein *et al.*, 2006). Furthermore, in CPWI, the width of the final image is not restricted by the imaging parameters and wide images can be produced. This is an advantage over the conventional focused imaging, where increasing the aperture size to improve the image quality results in reducing the number of scan lines, and narrower images are produced.

2.4.2 Disadvantages

One of the disadvantages that may occur when using CPWI is the blurring that results when averaging multiple images of a rapidly moving target. The effect of motion blurring increases when the target speed or the number of compounded angles is increased (Papadacci *et al.*, 2014). Therefore, there should be a trade-off between imaging quality, which increases with the number of compounded angles, and the effect of the blurring.

The spatial resolution achieved in CPWI is usually better than that in conventional linear imaging and PWI (Montaldo *et al.*, 2009). However, it is shown in the literature that increasing the number of compounded angles usually does not result in any improvement or even decreases spatial resolution (Jespersen *et al.*, 2000; Mohana Shankar & Newhouse, 1985; Montaldo *et al.*, 2009). The relationship between the angular parameters and resolution in CPWI is not investigated

in the literature yet, where more attention is given to the CPWI applications than to the imaging technique itself.

Another disadvantage of CPWI is the occurrence of grating lobes. These lobes are maximized after specific steering angles which differ from one system to another as described in the previous section. This leads to limiting the angular range within which the steering angles are selected.

The effect of having sound speed errors arises in both conventional imaging and CPWI. These errors occur when the value of the sound speed used during the beamforming operation is different from the actual value. This has the effect of assigning the wrong depth to the imaging points, in addition to reducing spatial resolution (Holfort *et al.*, 2008a). In linear imaging, the effect of the sound speed error increases with increasing the aperture width. Therefore in CPWI, as the aperture equals to the total number of elements, larger effect for the sound speed errors is expected.

2.5 CPWI Applications

2.5.1 Elastography

Elastography is the measurement of the stiffness of the tissue, where it is usually not possible to distinguish between soft and stiff tissue using conventional B-mode imaging (Szabo, 2004). This property is measured in elastography by compressing the required tissue and imaging it before and after the compression. This enables following the effect of pressure on tissue particles and estimating the local tissue displacement. The compression operation can be done either dynamically by generating shear waves that propagate inside the medium, which is called Shear Wave Imaging, or quasi-statically by compressing the medium using the imaging probe for a limited time, which is called Strain Imaging (Ramalli *et al.*, 2010). Imaging the tissue particles in both methods requires the use of ultrafast imaging techniques.

Shear Wave Imaging

The elasticity of the human tissue can be measured through the generation and depiction of shear waves inside the tissue (Szabo, 2004). Shear waves are the type of waves that propagate with a speed of 1 to 10 m/sec (Bercoff *et al.*, 2001) and have a low frequency of 50 to 500 Hz (Montaldo *et al.*, 2009). As the speed of propagation of this type of waves is much lower than that of the ultrasound waves which propagate with a speed of 1540 m/sec or more, shear waves are used to reveal elastic properties of the human tissue. This is done by generating and depicting these waves, then measuring their propagation pattern and behaviour inside the tissue. This is done through the use of ultrafast ultrasound imaging techniques. Tracking shear waves in tissues requires imaging with a minimum frame rate of 1000 frames/sec, in order to preserve the minimum theoretical limit of the Nyquist sampling rate (Montaldo *et al.*, 2009).

One of the methods used to generate shear waves is the use of an external mechanical vibrator. This is a very efficient measuring method but with some limitations related to the need for heavy equipment and the directivity of the generated shear waves. Acoustic Radiation Force Impulse (ARFI) is another way for generating shear waves using deeply focused ultrasonic beams. The displacement in tissue particles at the focus caused by the generated shear waves can then be estimated from the captured ultrasound images (Bercoff *et al.*, 2004; Montaldo *et al.*, 2009).

Bercoff *et al.* (2004) proposed the Supersonic Shear Imaging (SSI), which is a technique of generating strong-amplitude shear waves by successively focusing an ultrasonic beam called the pushing beam at different depths. This operation generates multiple shear waves that constructively interfere, making it possible for the ultrasonic imaging system, which is the same system used for applying the pushing beam, to track its propagation through the use of CPWI with frame rates of few kilohertz.

Strain Imaging

In this type of elastography, the compression operation is done mechanically using the imaging probe. The displacement is then estimated from the echo signals

taken before and after the compression using the correlation operation (Ramalli *et al.*, 2010). This technique was increasingly and successfully used during the last decade in different clinical diagnoses and treatment monitoring (Varghese, 2009).

In order to ensure a reliable displacement estimation for the tissue particles during compression, the use of ultrafast imaging is required. In addition to the accurate displacement estimation due to the high frame rates, CPWI provides comparable imaging quality as compared to conventional linear imaging. Two groups of researchers have experimentally studied the use of ultrafast imaging techniques in strain imaging (Park *et al.*, 2007; Ramalli *et al.*, 2010). As compared to conventional linear imaging, ultrafast imaging was able to provide superior CNR, SNR and spatial resolution.

2.5.2 Doppler Flow Imaging

Doppler analysis for flow imaging is one of the most important applications that require the use of ultrafast imaging for flow analysis and quantification. It enables imaging the fast transient phenomena that usually occur in blood flow, in addition to the peak and mean flow velocities and the resistance and pulsatility of the cardiac cycle (Bercoff *et al.*, 2011).

The ability of CPWI to produce the same quality as that in conventional linear imaging but with 10 times higher frame rate enables 300 frame/sec Doppler images, which was shown to be highly efficient in imaging very low velocity flows (Montaldo *et al.*, 2010). Bercoff *et al.* (2011) studied the use of CPWI for blood flow imaging, where the performance of this type of imaging was assessed by comparing with the conventional focused imaging. The results show that for the same depth and acquisition time, CPWI is able to produce 16 times more frames than that produced by focused imaging. This high frame rate provides the opportunity of achieving higher resolution with a high sensitivity to the flow characteristics.

2.5.3 Microbubble Imaging

Another application that requires the use of high frame rates is the Microbubble imaging. Microbubbles are bubbles of less than $10\mu\text{m}$ diameter (Gorce *et al.*, 2000), used as a contrast agent through injection into the blood. The intensity difference between the microbubble contents and the blood results in strong scattering and thus high imaging contrast is achieved. Microbubbles are also used to provide better visualization for the liver perfusion and coronary chamber (Couture *et al.*, 2009, 2012).

In conventional focused imaging and due to the high peak pressure, a big portion of the injected microbubbles is destroyed during imaging. The use of PWI results in decreasing the peak pressure and improving the microbubbles, at the cost of degraded imaging quality. This can be compensated by the use of CPWI that improves the imaging quality and preserves the high frame rate in the same time. Couture *et al.* (2012) studied the use of CPWI for microbubble imaging. The results indicated that for the same amount of resolution, the acoustic intensity required to disrupt 50% of the microbubbles with CPWI is 24 times higher than that in linear imaging, while at the same disruption level, CPWI provides a contrast of 11dB higher than that in linear imaging. This is added to the ability of CPWI to preserve the high frame rates and allow the imaging of additional transient phenomena that cannot be visualized with conventional imaging.

Chapter 3

Spatial Resolution in PWI

This chapter is based on a published paper entitled: *(The Effect of the Transducer Parameters on Spatial Resolution in Plane-Wave Imaging)*.

Point Spread Function (PSF) is a point with an amplitude of 1, resembling a complete reflection of the transmitted ultrasound pulse (Jensen, 2001). PSF is used to measure the efficiency of ultrasound systems assessed based on the spatial resolution, which is divided into axial and lateral resolutions for 2-Dimensional ultrasound imaging. These two resolutions are defined as the minimum distinguishable distances between two adjacent points located perpendicular and parallel to the transducer surface, respectively (Bushberg & Boone, 2011). A lower resolution value means better imaging is achieved. Lateral resolution is usually poorer than axial resolution, since it is mainly affected by the beam width, while axial resolution depends on the width of the transmitted pulse (Kremkau & Taylor, 1986).

There are two methods for measuring spatial resolution for ultrasound imaging systems. The first method is taken from the definition of spatial resolution mentioned above, where for estimating lateral resolution, two points are placed adjacent to each other in the lateral direction, parallel to the transducer surface. If the lateral profile passing from the centre of the points is displayed down to 50% of the peak amplitude, then the minimum distance at which the responses of the two points are separated will resemble lateral resolution. Similarly for axial

resolution, this measurement is repeated for two points located adjacent to each other in the axial direction (Azhari, 2010). The measurements in this method need to be repeated until the minimum distance is specified, which is an iterative and time consuming way. The second method is to measure the Full Width at Half Maximum (FWHM), which is defined as the mainlobe width of the PSF when the intensity drops to -6dB (Righetti *et al.*, 2003). This method is used for measuring spatial resolution as proposed by Harput *et al.* (2014).

In focused imaging, lateral resolution is usually estimated for ultrasound imaging systems from the beam width, which is calculated at the focal depth using the following formula (Hedrick, 2013; Shung, 2005):

$$R_{lat} = C.f_{\#}.\lambda, \quad (3.1)$$

where C is a constant depending on the used system, λ is the wavelength and $f_{\#}$ is the f-number that represents the ratio between the focal depth and aperture width. The lack of a focal point makes this formula unsuitable for estimating PWI lateral resolution, where the focal depth approaches infinity and thus lateral resolution becomes infinity too. The existence of a formula that estimates spatial resolution is important to enable assessing the PWI performance of any ultrasound system depending on its characteristics.

An empirical expression for PWI spatial resolution can be derived based on experimental measurements and observations for the effects of the imaging parameters on spatial resolution, rather than depending on mathematical derivations and equations. This requires studying the effect of each parameter separately while fixing the other parameters. This study is carried out in this chapter using Field II simulation program. Afterwards, the results represented by the curves that explain the effect of each parameter on axial and lateral resolutions were used with the help of Matlab curve fitting tool to derive an empirical expression that best clarifies the relation between resolution and the studied parameters. These parameters are the central frequency, wavelength, bandwidth, the number of elements, the total width of the transducer and the imaging depth. At the end of this chapter, a detailed discussion and conclusions are presented based on the obtained results.

3.1 Field-II Simulations Description

In this work, spatial resolution is measured using the FWHM, which is calculated using the function produced by [Harput *et al.* \(2014\)](#). This function can efficiently determine the mainlobe width at the required direction and intensity drop using interpolation method.

In digital images, the size of each pixel used to represent the image is specified by the used step size in the axial and lateral directions. This results in limiting axial and lateral resolutions to multiples of these steps ([Azhari, 2010](#)), introducing rounding errors to the calculations. Therefore, it is required to minimize the step size so that an accurate resolution estimation can be achieved. This minimization, on the other hand, increases the amount of computations required to produce a single image. Consequently, an experiment is needed in order to specify the largest suitable step that provides an accurate resolution estimation using less number of computations.

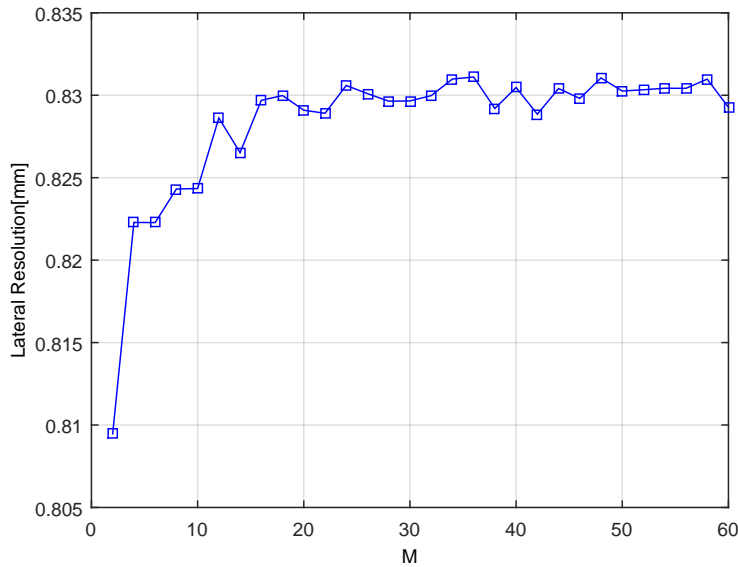


Figure 3.1: The lateral resolution when decreasing the step size in the lateral direction, for a PSF at the 30mm depth.

Using Field II simulations, the lateral resolution is evaluated at different step sizes as given in figure 3.1. The step size in this figure is calculated by λ/M ,

where increasing M (the x-axis) means smaller step is being used. It can be seen from the figure that the error in lateral resolution is directly proportional to the step size, or equally, inversely proportional to M . After $M=15$, the step size becomes small enough to decrease the error in the estimated resolution to $2\mu\text{m}$ or less. Therefore, the value of M is set to 15 during measuring lateral resolution in this thesis. As the step size used in axial direction is already smaller than the lateral step at $M = 15$, no estimation for the step size in axial direction is required. The system settings used during the simulation study of this chapter are given in detail in table 3.1, including the used axial and lateral step sizes.

The parameters whose effect is studied in this work are the central frequency, wavelength, bandwidth, the number of elements, transducer width and the imaging depth. Spatial resolution is measured for an array transducer with the number of elements varying from 32 to 256, a frequency range of 1 to 30MHz, bandwidth of 10 to 100%, a total aperture width of 10 to 60mm and an imaging depth of 1 to 200mm.

3.2 Methodology

Initially, the effect of each imaging parameter on axial and lateral resolutions of a PSF is studied separately. This is done by changing the required parameter within a specific range while fixing the other parameters to the values given in table 3.1. The results are plotted using curves that represent the effect of each parameter on axial and lateral resolutions. From these curves, and with the help of Matlab curve fitting tool, a mathematical expression is derived that best explains the relationship between the resolution and the varying parameters.

3.3 Results

In order to develop an expression that explains the relation between resolution and the transducer parameters, the effect of each of these parameters is studied separately, as shown in the following sections:

Table 3.1: *THE PARAMETERS OF THE ULTRASOUND SYSTEM USED DURING THE SIMULATION STUDY.*

Parameter	Value
Transducer type	Linear array
f_s	100MHz
f_0	5MHz
Bw	2MHz
wavelength (λ)	$c/f_0 = 308\mu\text{m}$
N	96
Aperture width	30mm
Pitch	$\lambda = 308\mu\text{m}$
Kerf	10% of pitch= $30.8\mu\text{m}$
element width	$277.2\mu\text{m}$
element height	6mm
sound speed	1540m/s
Excitation pulse	2-cycles Gaussian pulse
Focal depth	Infinity (No focusing)
Transmit Aperture	96
Receive Aperture	96
Transmit Apodization	Hamming
Receive Apodization	No apodization
Lateral step size (dx)	$\lambda/15 = 20.53\mu\text{m}$
Axial step size (dz)	$c/2f_s = 7.7\mu\text{m}$
Medium Attenuation	0 dB/cm.MHz

3.3.1 Spatial Resolution versus Bandwidth

While fixing the central frequency to 5MHz, the bandwidth is changed from 10 to 100% and the resulted resolution curves are shown in figure 3.2. It can be seen that within this range, the bandwidth has a minor effect on lateral resolution, unlike axial resolution which shows inverse proportion to the bandwidth. This is due to the dependence of axial resolution on the pulse width, which is mainly

affected by the transmitted bandwidth. It will be seen from the following sections that the bandwidth is the only parameter that affects axial resolution, in contrast to the lateral resolution which is affected by the other parameters.

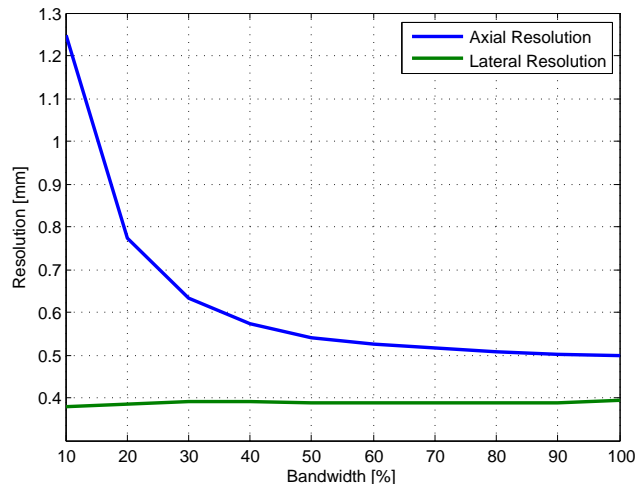


Figure 3.2: The effect of the bandwidth on spatial resolution. Wavelength is fixed to $308\mu\text{m}$.

3.3.2 Spatial Resolution versus Central Frequency

For a transducer with a fixed bandwidth of 2MHz, the central frequency was changed from 1 to 30MHz. Spatial resolution for this range of frequencies is shown in figure 3.3. According to this figure, Axial resolution is hardly affected by the increase in the central frequency, while for lateral resolution, a direct proportion to the central frequency can be seen.

Figure 3.4 shows the effect of the wavelength on lateral resolution for the frequencies between 1 and 30MHz at a speed of sound of 1540m/s. This figure shows a linear relationship between the wavelength and lateral resolution at this range of frequencies. Axial resolution is not included in this figure as it is already shown not to be affected by the central frequency.

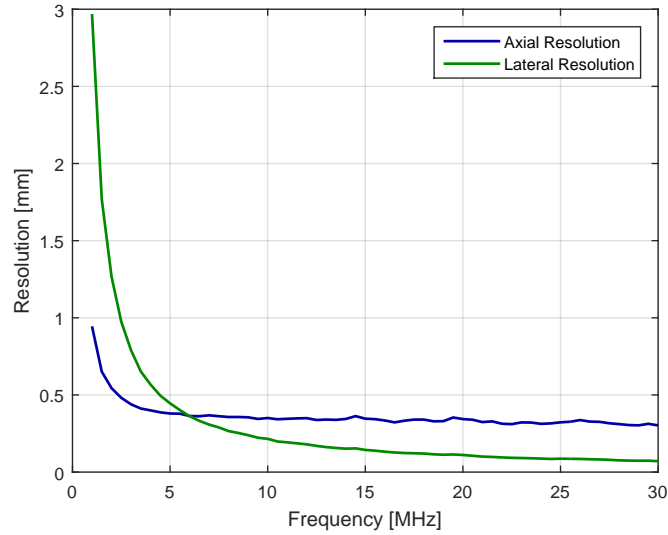


Figure 3.3: The effect of the central frequency on spatial resolution, for a PSF at the 30mm depth.

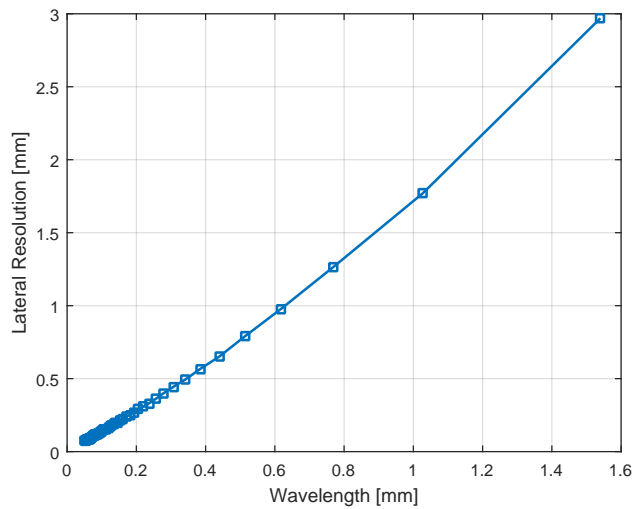


Figure 3.4: The effect of the wavelength on lateral resolution, for a PSF at the 30mm depth.

3.3.3 Spatial Resolution versus the Number of Elements

It is stated in the literature that increasing the number of active elements in the transducer has the effect of increasing lateral resolution in PWI (Avanji *et al.*, 2013; Holfort *et al.*, 2010; Szabo & Lewin, 2013). However, their statements

were based on the experiments where the transducer width was changed correspondingly with the number of elements. This means that the effect of these two parameters, the number of elements and the transducer width, are studied in the same time.

A more accurate evaluation for the effect of the number of elements on resolution can be achieved by fixing the transducer width when varying the number of elements. Using the parameter values given in table 3.1, spatial resolution is determined when changing the number of elements from 32 to 256, while fixing the total transducer width to 30mm. The resultant axial and lateral resolution curves are given in figure 3.5.

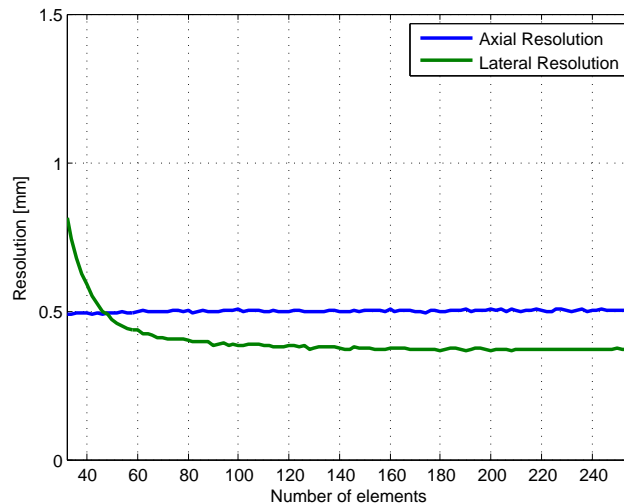


Figure 3.5: Spatial resolution vs. the total number of elements for a PSF at the 30mm depth. Aperture width is fixed to 30mm and wavelength is $308\mu\text{m}$.

It can be seen from figure 3.5 that axial resolution is not affected by changing the number of elements. Lateral resolution, on the other hand, was improved with increasing the number of elements. However, increasing the number of elements to higher than 100 added no more improvement to lateral resolution.

Increasing the number of elements with fixing the transducer width requires decreasing the centre-to-centre distance correspondingly. At the central frequency of 5MHz and sound speed of 1540m/s, it can be calculated that the pitch is equal to one wavelength when using 97 elements. As explained before, the effect of the grating lobes increases when the centre-to-centre distance is greater than

one wavelength, due to constructive interference that occur between the signals received by the adjacent elements (Huang *et al.*, 2007). Grating lobes result in degrading the imaging quality, including lateral resolution, which explains the behaviour of the lateral resolution curve when the number of elements is less than 97. After achieving the limit of one wavelength for the centre-to-centre distance by increasing the number of elements, lateral resolution starts not to be affected by the number of elements.

Depending on this explanation, the number of elements can be considered to have no direct effect on spatial resolution. Therefore, in the next section, the effect of the transducer width will be studied by changing the number of elements correspondingly, while fixing the centre-to-centre distance to one wavelength.

3.3.4 Spatial Resolution versus Aperture Width

The effect of the aperture width on spatial resolution is studied within the range from 10 to 60mm width. Changing the total transducer width is accompanied with amending the total number of elements since the centre-to-centre distance is fixed to one wavelength. The resulting resolution curves are shown in figure 3.6.

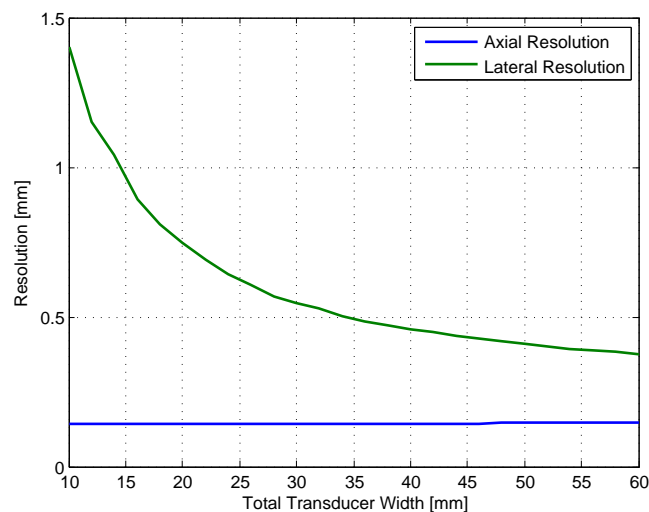


Figure 3.6: The effect of the aperture width on spatial resolution in the absence of medium attenuation. Wavelength is fixed to $308\mu\text{m}$.

According to this figure, increasing the total aperture width is found to have a direct effect on lateral resolution and no effect on axial resolution. Choosing the transducer width for medical imaging applications is therefore a trade-off between lateral resolution and the ability to provide a complete contact with the body wall during imaging.

3.3.5 Spatial Resolution versus Imaging Depth

The effect of the imaging depth on spatial resolution was studied for up to the depth of 200mm. As shown in figure 3.7, the lateral resolution value is directly proportional to the imaging depth, while axial resolution shows no change. Figure 3.8 compares the imaging of 9 scattering points located at the depths from 30 to 190mm when using PWI and linear imaging. It can be noticed that the beam width is controlling the lateral resolution in linear imaging where a focus at 70mm is used, while the lateral resolution in PWI is decreasing linearly with the depth due to the lack of focusing.

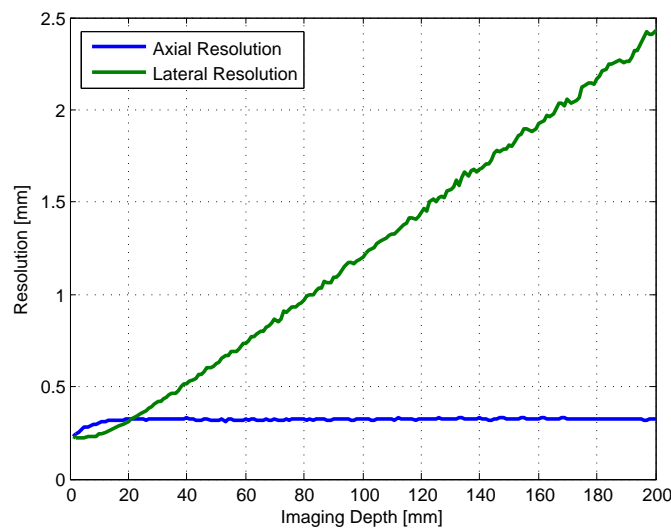


Figure 3.7: The effect of the imaging depth on spatial resolution in the absence of medium attenuation. Wavelength is fixed to $308\mu\text{m}$.

3.4 Lateral Resolution Empirical Expression

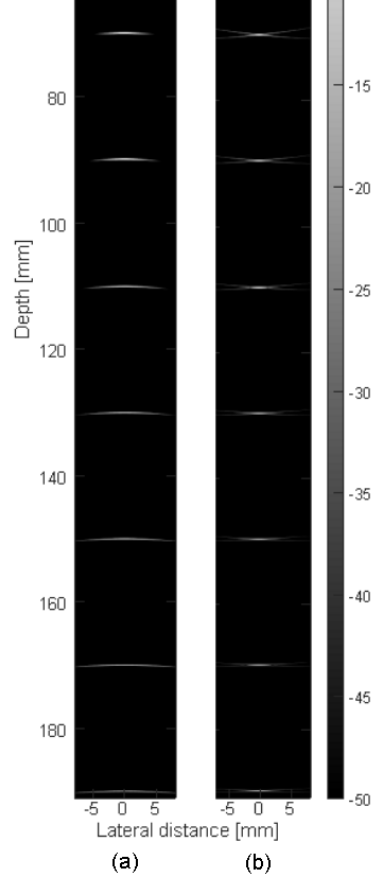


Figure 3.8: Simulated 9 scattering points located at the depths from 30 to 190mm to show the effect of increasing the depth on lateral resolution in: (a) linear imaging focused at 70mm depth and (b) PWI.

3.4 Lateral Resolution Empirical Expression

The results of this study, as given in details in table 3.2, show that the PWI lateral resolution value is directly proportional to the wavelength and the imaging depth, and inversely proportional to the total transducer width. According to this study, the three variables are used to produce a single variable called b , so that:

$$b = \frac{\lambda \cdot z}{W_t}. \quad (3.2)$$

With the help of curve fitting tool in Matlab, the lateral resolution is plotted at different values of b , as given in figure 3.9. From this figure, it can be noticed that

3.5 Lateral Resolution in the Presence of Attenuation

Table 3.2: *THE RELATIONSHIP BETWEEN LATERAL AND AXIAL RESOLUTIONS AND THE STUDIED IMAGING PARAMETERS.*

Parameter	$R_{lat} \propto$	$R_{ax} \propto$
Central Frequency (f_0) (BW is fixed to 2MHz)	$1/f_0$	-
Wavelength (λ)	λ	-
Bandwidth (BW)	-	$1/BW$
Number of elements (N)	-	-
Aperture Width (W_t)	$1/W_t$	-
Imaging depth (Z)	Z	-

R_{lat} is the Lateral Resolution,
 R_{ax} is the Axial Resolution.

a linear relationship connects b with lateral resolution. Therefore, an empirical expression of PWI lateral resolution can be given by:

$$R_{lat} = k_1 \cdot b, \tag{3.3}$$

where k_1 is a constant whose value was found to be 1.32.

The degree of fit between the data and the fitted curve is usually measured using R^2 , where a value of 1 represents a perfect fit (Righetti *et al.*, 2003). Figure 3.9 shows the high fit of the lateral resolution values measured from the simulations with the fitted curve of equation (3.3), with $R^2 = 0.994$.

3.5 Lateral Resolution in the Presence of Attenuation

Attenuation is the energy decrease in the ultrasound signal that travels through the medium. The amount of this decrease is affected by the signal frequency and the depth, and it is estimated from the attenuation coefficient, measured in dB/cm.MHz. In human soft tissue in general, the attenuation coefficient of ultrasound signals is about 1dB/cm.MHz (Ward, 1999).

3.6 Lateral Resolution in the Presence of Medium Nonlinearity

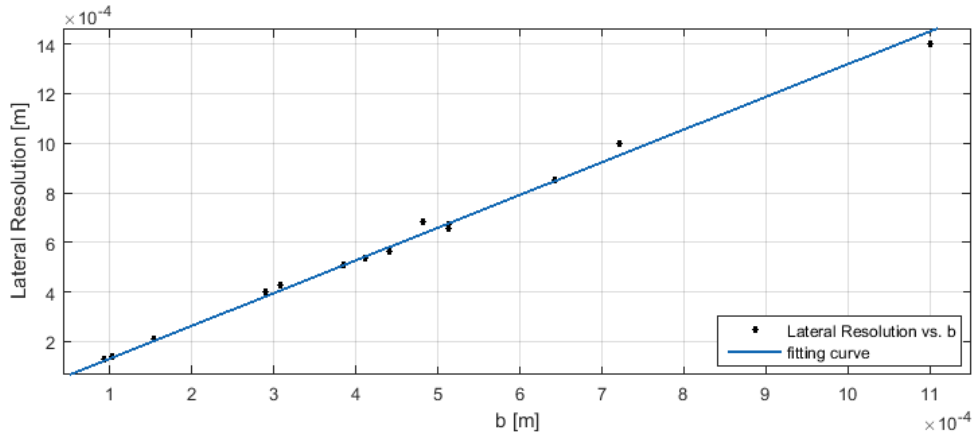


Figure 3.9: Matlab curve fitting tool for the lateral resolution versus b , which resembles the wavelength multiplied by the imaging depth and divided by the total aperture width.

Due to the presence of attenuation in almost all ultrasound imaging media, it is important to clarify the effect of the imaging parameters on lateral resolution in the presence of attenuation. The curves that represent the effect of frequency, bandwidth, aperture width and depth on lateral resolution with and without the presence of attenuation are given in figures 3.10, where in the presence of attenuation, the attenuation coefficient was set to 0.5dB/cm.MHz. From this figure, it can be noticed that for the depth curve, lateral resolution starts to change logarithmically with the depth in the presence of attenuation. However, this change can be considered to be nearly linear for up to 50mm. For the other three parameters, attenuation was affecting lateral resolution by only adding a constant shift to the curve.

3.6 Lateral Resolution in the Presence of Medium Nonlinearity

In Field II, only the linear propagation of ultrasound signals is simulated without considering the non-linearity effects of the medium. In real life, harmonics that are multiples of the transmitted frequency are generated during the nonlinear propagation of ultrasound signals through the medium. When generated, the

3.6 Lateral Resolution in the Presence of Medium Nonlinearity

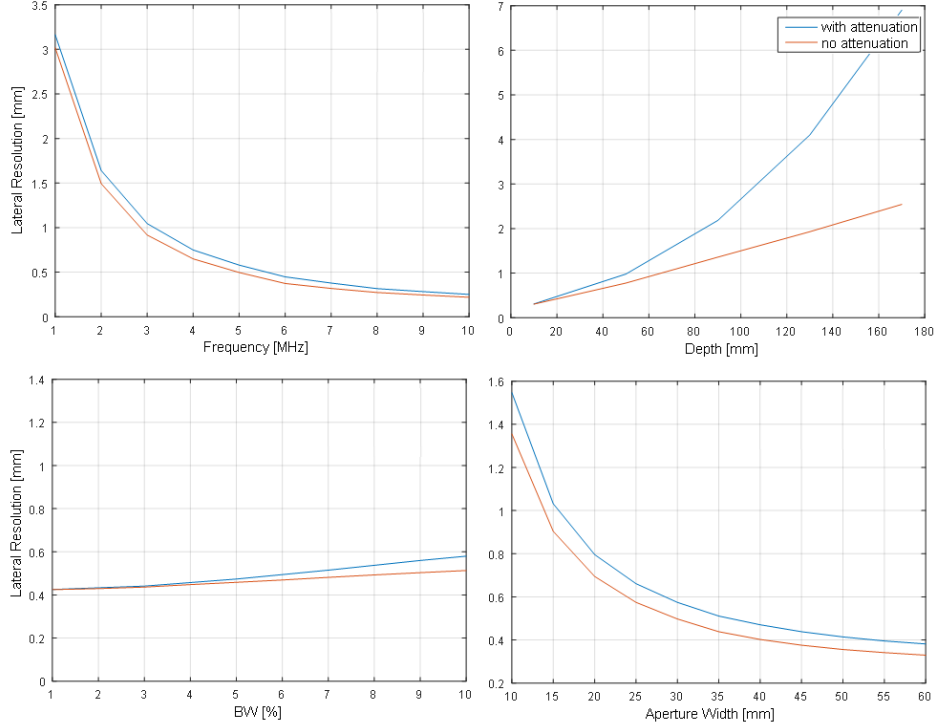


Figure 3.10: Lateral Resolution versus the imaging depth, with and without the presence of attenuation.

harmonic frequencies result in degrading the resolution in the fundamental signal from which they take their energy. The amount of the generated harmonics is calculated by the shock parameter that depends on multiple factors according to the following equation (Duck, 2002):

$$\sigma_s = \frac{2\pi}{\rho_0 c^3} P_0 f_0 z \left(1 + \frac{B}{2A}\right), \quad (3.4)$$

where ρ_0 , P_0 and B/A are the medium density, transmitted pressure and nonlinearity coefficient, respectively. The generation of the second harmonics increases and peaks when the shock parameter is between 1 and 3, where after 3, the harmonics are weakened by the attenuation due to their high frequencies.

Equation (3.4) shows that the value of σ is directly proportional to the transmitted frequency and imaging depth. Therefore, second harmonics are expected to reduce the lateral resolution in the central frequency and depth curves given in figures 3.3 and 3.7. This reduction starts when the value of f or z is increased so

that σ becomes greater than 1, which increases the harmonics amplitude. These harmonics weaken the fundamental signal and result in increasing lateral resolution value to higher than that given in the central frequency and depth curves, starting from the value that makes $\sigma > 1$.

3.7 Discussion

It is confirmed during this study that the bandwidth is the only parameter affecting PWI axial resolution. This means that both linear imaging and PWI has the same axial resolution, in contrast to the lateral resolution which is found to be proportional to the central frequency, aperture width and imaging depth.

Lateral resolution in PWI according to the expression derived in this work is very close to that in linear imaging at the focal depth, which can be clearly noticed from figure 3.8. This is due to the use of dynamic focusing during the beamforming at the receive in PWI, which compensates for the lack of focusing. Furthermore, PWI uses all the transducer elements, while in linear imaging, only part of these elements are used as the aperture.

From figure 3.3, it can be noticed that increasing the central frequency to higher than 10MHz has no effect on lateral resolution. Therefore for a transducer that provides a band of frequencies of higher than 10MHz, it is recommended to exploit this band for increasing the bandwidth rather than the central frequency. This is done after considering the effect these two parameters on resolution, attenuation and penetration depth.

The relation between the three parameters of the aperture width, number of elements and centre-to-centre distance is similar to the relation between the three sides of a triangle; when one of them is fixed, then any change in the second one is accompanied by changing the third one accordingly. It is proved during this study that increasing the aperture width improves lateral resolution, while the number of elements has no direct effect on it. Therefore when choosing between two transducers with different aperture widths, the wider transducer is recommended for getting higher resolution, only if the centre-to-centre distance was fixed and the width is increased by increasing the number of elements. Otherwise, grating lobes will be introduced when the pitch is increased to higher than one wavelength,

and will negatively affect lateral resolution in the wide transducer. Another point to bear in mind when selecting the transducer width is to ensure a complete coupling with the body wall is possible, as mentioned earlier.

3.8 Conclusions

Resolution is an important metric for assessing the quality of ultrasound imaging. In linear imaging, the resolution is estimated from the width of the transmitted beam, where a formula for lateral resolution at the focal depth exists for different ultrasound systems. However, such a formula can not be used for PWI due to the lack of a focusing point. Deriving a formula for PWI lateral resolution helps in estimating the feasibility of using PWI transducers for different applications. This chapter seeks to introduce an empirical expression for PWI lateral resolution that is based on experimental measurements and observations, where the effect of different imaging parameters is studied using Field II simulation program. The results of this study show that PWI lateral resolution value is directly proportional to the wavelength and imaging depth and inversely proportional to the aperture width, while both the number of elements and bandwidth are shown to have no significant effect. Also from this study, axial resolution in PWI is verified to be equal to that in linear imaging, where it is only affected by the transmitted bandwidth.

The produced formula is very near to that of linear imaging at the focal depth. However, lateral resolution is higher in PWI when compared to that in linear imaging at the focal depth. This is due to the direct effect of the aperture width on lateral resolution in both cases, where the aperture is the total number of elements in PWI, but only part of these elements are used in linear imaging as the aperture.

The dependency of PWI lateral resolution on the transducer parameters makes the selection of the appropriate transducer an essential step for improving the quality of PWI, which is significant for many applications such as shear wave elastography and microbubble imaging.

Chapter 4

The Selection of CPWI Parameters

This chapter is based on a published paper entitled: *(Selecting the Number and Values of the CPWI Steering Angles and the Effect of that on Imaging Quality)*.

The first step required to perform CPWI using either simulators or lab equipments is to specify the CPWI imaging parameters. These parameters are the angular range within which the steering angles are selected, angular step and the number of compounded angles. Due to the importance of frame rate in ultrafast imaging, selecting the number and value of the compounded angles is a critical step to achieve the best possible imaging quality using the minimum number of angles whilst preserving the frame rate.

Several research groups have investigated the use of CPWI in various types of diagnostic imaging using different compounded angles. CPWI was successfully implemented by these groups with achieving comparable imaging results ([Entrekin *et al.*, 2001](#); [Hernandez *et al.*, 1996](#); [Huber *et al.*, 2002](#); [Jespersen *et al.*, 2000](#); [Kern *et al.*, 2004](#); [Opretzka *et al.*, 2011](#); [Vogt & Ermert, 2008](#)). However, the methods based on which the steering angles are selected were not mentioned.

[Wilhjelm *et al.* \(2004\)](#) have experimentally investigated the effect of the number of angles and the angular range on the imaging quality. They concluded that compounding more angles within the $\pm 14^\circ$ angular range can significantly

improve the imaging quality, while using angles from outside this range is questionable. The reason behind choosing the used angular range and step were not explained or connected to the imaging parameters. Later, [Montaldo *et al.* \(2009\)](#) proposed a mathematical method to specify the angular step and the number of angles so that the same quality as that of the multifocus imaging is achieved. However, the number of required angles calculated by their method was so high that the frame rate was not suitable for ultrafast imaging. In addition, the effect of the angular range was not included in this study, where a wider range could result in the same quality with less number of compounded frames.

In this chapter, a new method for selecting the angular range and the number of angles in CPWI depending on the characteristics of the transducer and medium using Field II program is produced. Experiments were performed on a wire phantom to show the efficiency of the produced method. The results show a comparative imaging quality of CPWI at the selected parameters when compared with linear imaging.

4.1 Methodology

In order to minimise the number of compounded angles and preserve the frame rate in CPWI, a method of selecting the number and values of the compounded angles based on the characteristics of the transducer and the imaging medium is developed. The angular range is selected depending on the plot of figure 4.1, which gives the maximum intensity received by the field points located at the centre of the transducer at different depths for a range of steering angles.

In figure 4.1, the intensity curves are plotted for the depths from 10 to 100mm with a step of 10 mm, for the steering angles from 0 to 50°. As the value of the received intensity is calculated at the centre of the transducer ($x = 0$), the behaviour of the curve at the negative and positive of any angle will be the same. Therefore, the received intensity is only given for positive steering angles.

It can be noticed from this figure that the maximum intensity received by the field points at $x=0$ mm comes from the centre of the beam at 0°. Afterwards, the intensity starts to decrease with increasing the steering angle as the centre of the beam moves away from the centre of the imaging field. After a specific

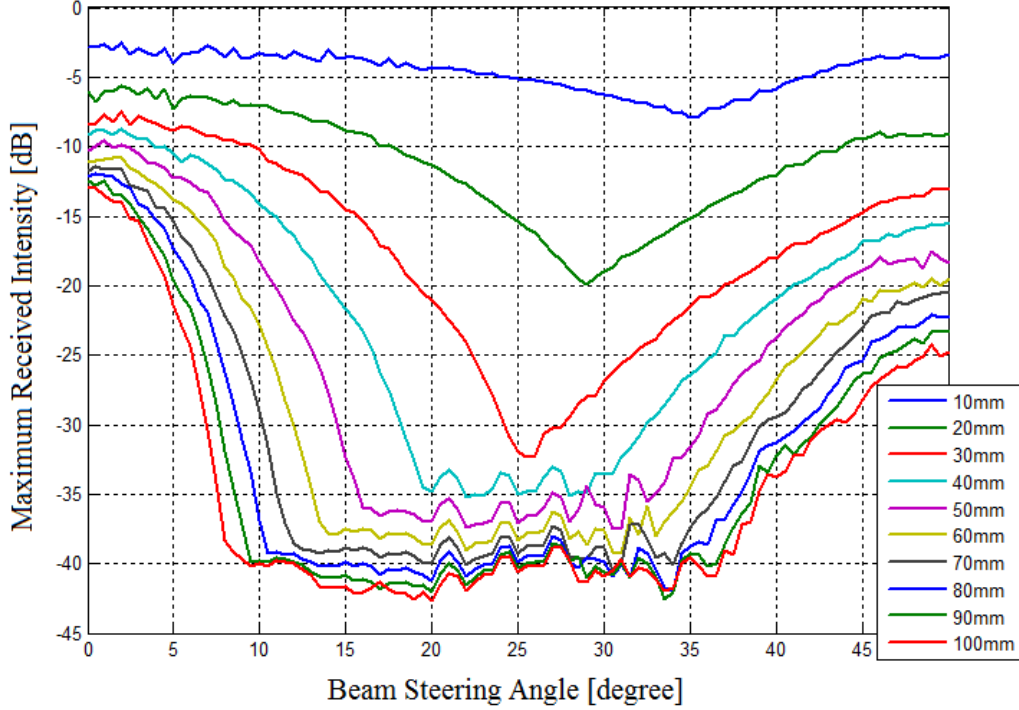


Figure 4.1: The maximum intensity received by the field points at the centre of the transducer at a range of steering angles.

limit of steering, the central field points start not to receive any intensity from the main beam. However, the received intensity does not become zero after this limit because of the existence of side lobes. Thus it can be seen that the received intensity has a noisy pattern which starts to increase in value with increasing the steering angle as it becomes nearer to the angle at which grating lobes occur.

In order to specify the maximum steering angle or the angular range, both the transducer sensitivity and the medium attenuation at the imaging depth are considered. This is done by calculating the minimum distinguishable intensity by the transducer at the angular range using the following equation:

$$I_{AR} = S + A_t, \quad (4.1)$$

where S is the transducer sensitivity, which is usually given by the manufacturer, and A_t is the total amount of the medium attenuation at the required imaging depth. After I_{AR} is calculated, the curves in figure 4.1 are used so that the steering

angle corresponding to I_{AR} is considered as the angular range, where the echoes from angles from outside this range will not be recognized by the receiver. If I_{AR} was low so that all the steering angles before side lobes occur have a recognizable echo signals, then the angle at which the effect of side lobes begins is considered as the angular range.

In addition to the factors mentioned above, the angular range is directly affected by the imaging depth and the transducer width. This is shown clearly in figure 4.2. In this figure, the angular range is measured at the limit where the side lobes effect starts to occur, assuming a transducer sensitivity of -56dB with the water being the imaging medium, for six different numbers of elements. It can be seen that the angular range is decreased with increasing the imaging depth, while it increases when the number of the transducer elements increases (using a fixed centre-to-centre distance) because larger beams are produced.

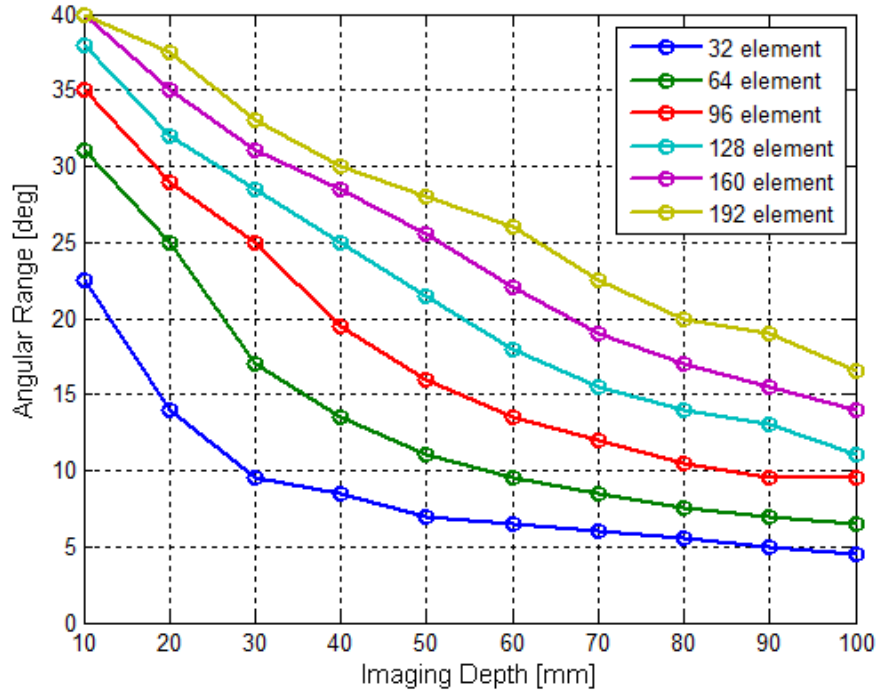


Figure 4.2: The change in the angular range with the imaging depth using different aperture sizes.

4.2 Experimental Setup

The imaging was carried out using the L3-8/40EP medical probe, which has 128 element and a centre-to-centre distance of 0.3048mm, driven by the Ultrasonic Array Research Platform (UARP) imaging device. UARP was designed to provide the control for 96 transducer elements, which is why 96 out of the available 128 elements were used during the imaging (Harput *et al.*, 2013; Raiton *et al.*, 2011; Smith *et al.*, 2012). A Gaussian pulse with a 5.05MHz central frequency and 100% bandwidth was used for pulsing the elements at the transmit and the RF signals were received with a sampling frequency of 50MHz.

4.2.1 Wire Phantom

The imaging quality in terms of the spatial resolution and level of artefacts are usually measured using PSF, which is similar to assessing a system by its impulse response. Wire phantoms are usually used to provide point targets with a black background (no reflections), which is provided by putting the phantom in a clear demineralized degased water. Water has 0.0022dB/cm.MHz attenuation coefficient and a sound speed of 1480m/sec at a temperature of 20°C (Culjat *et al.*, 2010).

The wire phantom used during the lab measurements of Linear Imaging and CPWI in this chapter consists of seven point targets, distributed as shown in figure 4.3a with a space of 10mm in between the wires. To simulate the point targets, a nylon wire with 0.12mm diameter was installed on an acrylic water tank as shown in figure 4.3b. This phantom is placed in a water tank filled with deionized degased water, while the probe is located perpendicular to the wires so that each wire appears as a single point. The probe position was fixed using a holder to ensure an immovable transducer position along the imaging for a correct comparison.

4.2.2 Specifying the Angular Range

At the imaging depth of 80mm for the wire phantom and a 5.05MHz central frequency, the amount of attenuation applied to the signal by the medium is about

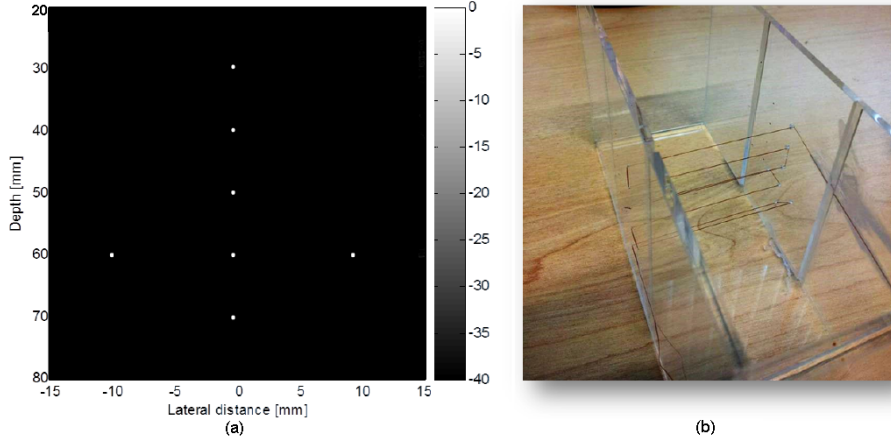


Figure 4.3: (a) The model of the scattering points simulated using the wire phantom (b) The wire phantom used in the lab experiments.

0.02dB, where the imaging was done in the water that has 0.0022dB/cm.MHz attenuation coefficient (Culjat *et al.*, 2010). This amount of attenuation has a very small effect on the angular range and can be neglected. However, in almost all the types of the human tissue, the attenuation coefficient is about 0.5dB/cm.MHz or more (Culjat *et al.*, 2010), which causes a significant amount of signal attenuation that can not be neglected. Because of the high sensitivity of the transducer and the low attenuation in water, all the steering angles in figure 4.1 can produce a detectable amount of intensity for the used medical probe, which has a high sensitivity of -56dB as given by the manufacturer. Therefore, and in order to avoid the effect of the side lobes on the angular range, the angle at which the effect of the side lobes starts to occur is chosen as the maximum steering angle, which for the depth of 80mm is equal to $\pm 10.5^\circ$.

4.2.3 Specifying the Number of Compounded Angles

After specifying the angular range for steering, the number of angles can be specified by depending on the quality of the produced images. The quality is expected to continue improving up to a specific limit, and afterwards this improvement becomes negligible. This is because increasing the number of angles within a constant angular range decreases the step between the angles so that the arte-

facts of these individual angles will overlap. This overlapping will be higher near to the scattering points, causing less artefacts cancellation during the compounding operation. Thus, increasing the number of angles after a specific limit will be useless and a waste of the frame rate which is inversely proportional to the number of compounded angles.

4.3 Results and Discussions

4.3.1 B-mode Images

The wire phantom images obtained using CPWI are shown in figure 4.4 when compounding 8 different numbers of angles within the $\pm 10.5^\circ$ angular range, while the linear imaging results are shown in figure 4.5 when using 6 different aperture lengths.

In CPWI, it can be seen that the image is visually improved with increasing the number of compounded angles. However, after compounding more than 11 angles, little or no improvement can be noticed. Therefore, the result of compounding 11 angles can be considered as the best image among the images given in the figure. In linear imaging, the image is improved with increasing the aperture size, as both the noise level and spatial resolution of the scattering points are improved with this increase. However, this improvement is at the cost of producing narrower images, as the number of scan lines is inversely proportional to the aperture width as described in section 2.1, while in CPWI, the size of the produced image is not affected by the compounded angles as the aperture width is not changed. For the images in figure 4.5, if the width of the image is of no importance, then the 48 element aperture image can be considered as the best result, as lower number of scan lines are produced leading to a higher frame rate, with having the best spatial resolution and lowest level of artefacts as compared with other images in the figure.

It can be noticed that the results of the lab measurements shown in figure 4.4 are very near to the Field II simulation results of coherent CPWI shown in figure 2.7(b). This is due to the accurate representation of the simulation of Field II for the linear behaviour of ultrasound signal in mediums. The level of noise

4.3 Results and Discussions

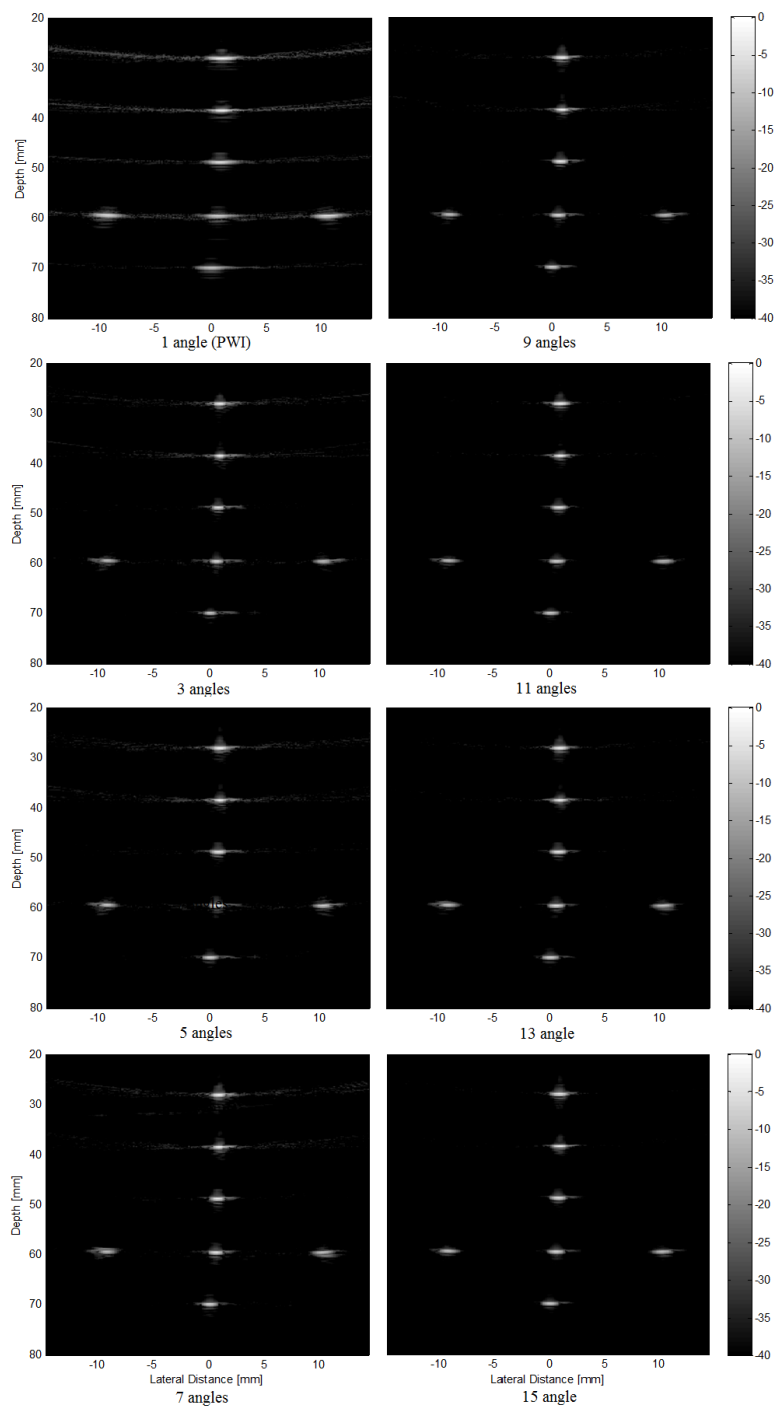


Figure 4.4: Experimental results of the wire phantom when using CPWI with different numbers of compounded angles within the $\pm 10.5^\circ$.

4.3 Results and Discussions

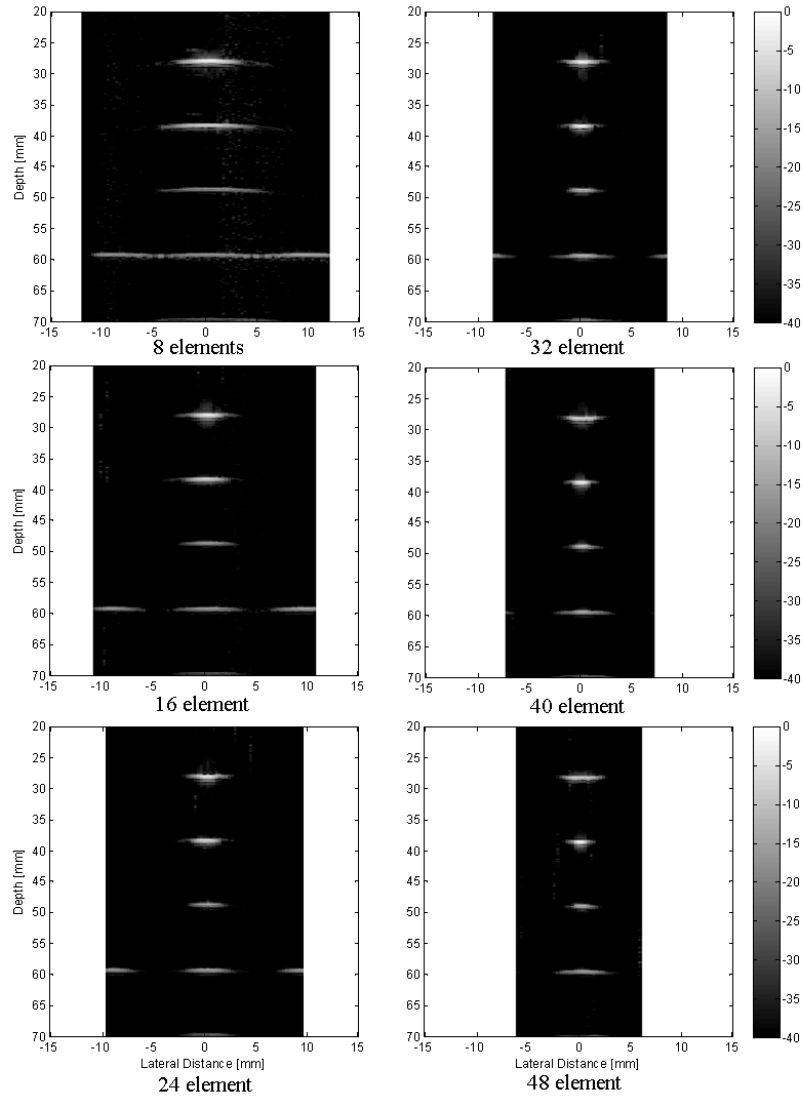


Figure 4.5: Experimental results of the wire phantom when using linear imaging with different numbers of elements in the aperture.

is a little higher in the simulation results and this is due to the use of a wider dynamic range of 60dB. Wider dynamic ranges have the advantage of enabling distinguishing between the different types of tissues, but the disadvantage is that the noise level is increased.

Another difference between the two results is the additional intensities observed around the scattering points in the lab images and do not appear in Field II simulations, in both linear imaging and CPWI. This can be explained as the effect of the generated harmonic frequencies, where only the linear behaviour is simulated in Field II (Jensen, 1999).

4.3.2 Spatial Resolution

Spatial resolution is divided into axial and lateral resolutions. Axial resolution which depends on the width of the transmitted signal is not affected by the used imaging technique, as shown in chapter 3. For this reason, the change in the number of compounded angles in CPWI or the number of the aperture elements in linear imaging did not meet a significant change in axial resolution, which is shown in the curves of figure 4.6. However, the axial resolution achieved with CPWI is better than that achieved with linear imaging. The reason for this may be the existence of sound speed errors which have higher effect for larger apertures, where ideally the axial resolution is the same for the two imaging techniques because the same excitation signal is used.

Lateral resolution, on the other hand, is affected by the applied imaging technique. It was assessed for the 40mm depth point at the -10dB width. For linear imaging, lateral resolution is directly proportional to the aperture width, which is shown in figures 4.7 and 4.9. However, increasing the aperture width decreases the number of scan lines and thus narrower images are produced. For this reason, the number of aperture elements were not increased in the measurements of figure 4.9 to more than 40, as the width of the produced image becomes about 14mm and the scattering points at $x = \pm 10\text{mm}$ become invisible. In figure 4.7, lateral resolution in PWI and linear imaging are plotted together for comparison. This comparison shows that lateral resolution in PWI is very near to that of linear imaging with 24-element aperture. However, the noise level at the

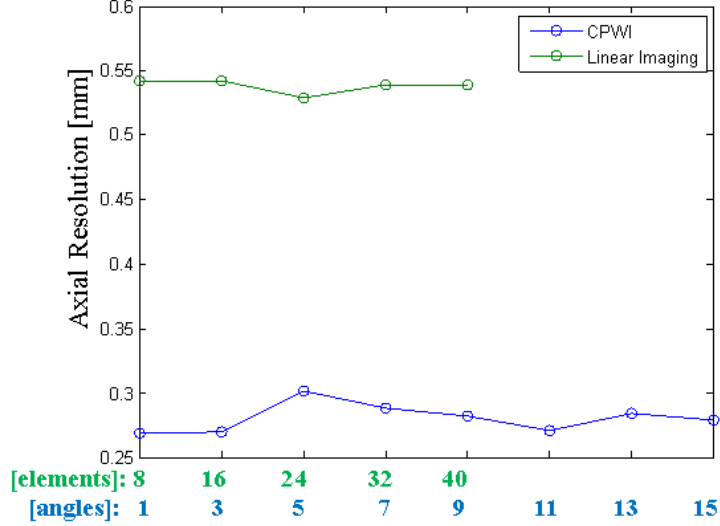


Figure 4.6: A comparison of the axial resolution between linear imaging at different aperture sizes and CPWI at different numbers of compounded angles at the -10dB width, for the point at the 40mm depth, $x=0$ mm. Wavelength is fixed to $293\mu\text{m}$.

sides of the scattering point is much higher, due to the lack of focusing. Figure 4.9 shows two curves representing the lateral resolution values in linear imaging and CPWI. In CPWI, starting the compounding with 3 angles results in a significant improvement in lateral resolution by 1.12mm compared to PWI. However, when compounding more angles no more improvement can be noticed, as can be seen from figures 4.8 and 4.9. The behaviour of CPWI lateral resolution is explained using figure 4.10, which shows a schematic diagram for the lateral resolution areas of three compounded signals. It can be seen that the compounding operation results in a lateral resolution that equals to the overlapped areas of the individual resolutions. When smaller angular step is used as in 4.10(a), the overlapped area is increased and the overall lateral resolution is thus degraded. This is what happens when increasing the number of compounded angles to more than 3 within a fixed angular range. From figure 4.9, a slight decrease in the lateral resolution is noticed when the step between the angles is decreased, which leads to concluding that the lateral resolution will approach that of PWI as the number of compounded angles approaches infinity, or equally, as the angular step

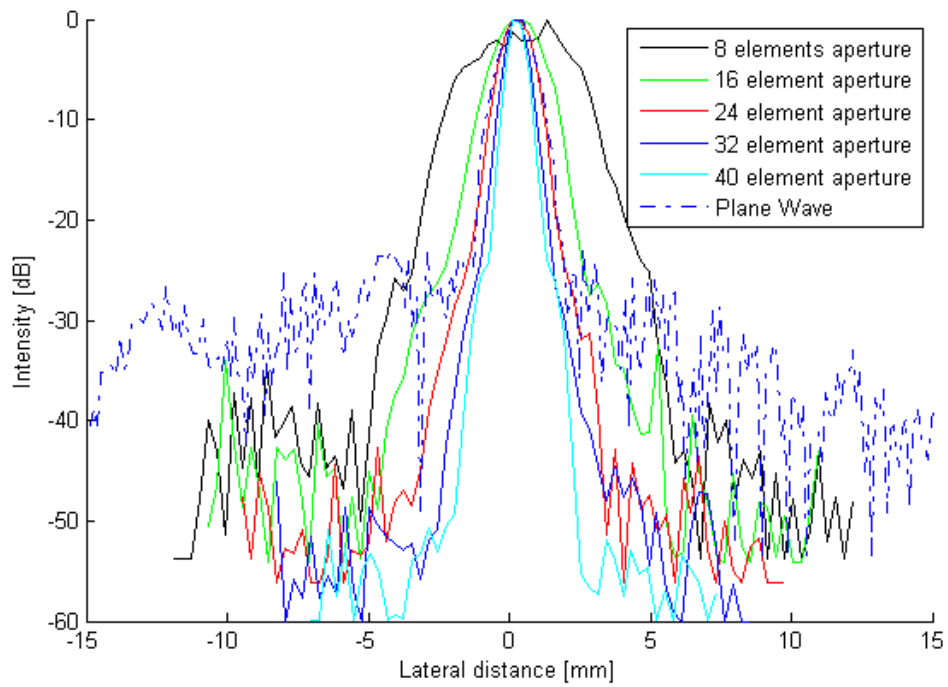


Figure 4.7: A comparison between the lateral resolution in PWI and linear imaging with different aperture widths, for the point at the 40mm depth in figure 4.5.

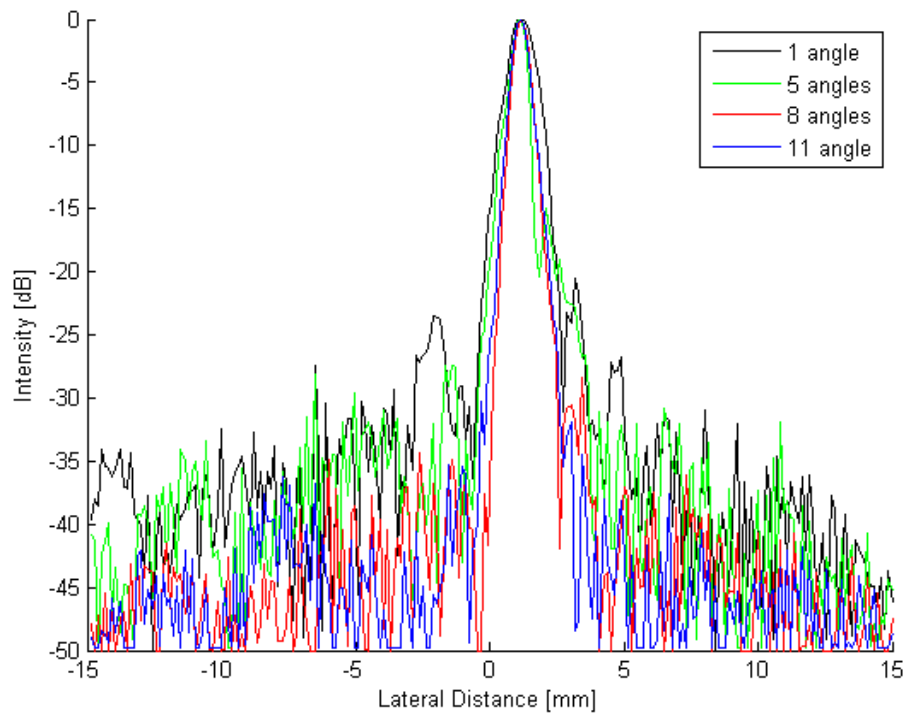


Figure 4.8: The CPWI lateral resolution when using different numbers of compounded angles, for the point at the 40mm depth in figure 4.4.

approaches 0. Therefore in CPWI, minimizing the number of compounded angles is not only important for preserving the frame rate, but also for preserving lateral resolution.

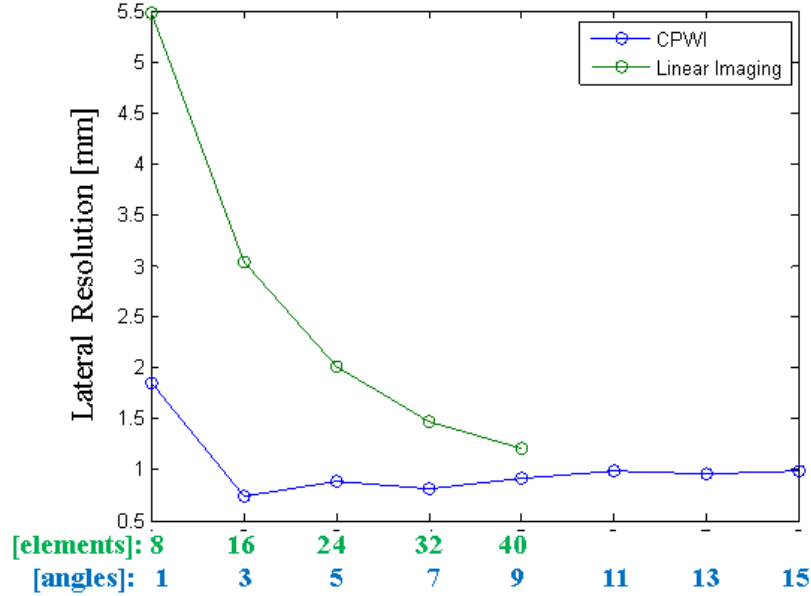


Figure 4.9: A comparison of the -10dB lateral resolution between linear imaging at different aperture sizes and CPWI at different numbers of compounded angles, for the 40mm depth point.

4.3.3 Level of Artefacts

Imaging artefacts are the false information which show a structure in the image that does not exist, or hide a structure that actually exists. They are usually caused by the physical limitations of the imaging technique (Baun, 2004; Hindi *et al.*, 2013). The false information given by the artefacts should be avoided or eliminated as it may degrade the imaging quality and lead to an inaccurate diagnosis (Baun, 2004).

The effect of the artefacts depends on the used imaging technique. In linear imaging, each scan line in the image is produced from a separate RF data, so the artefacts appear as vertical lines, as can be seen in figure 4.5. These artefacts

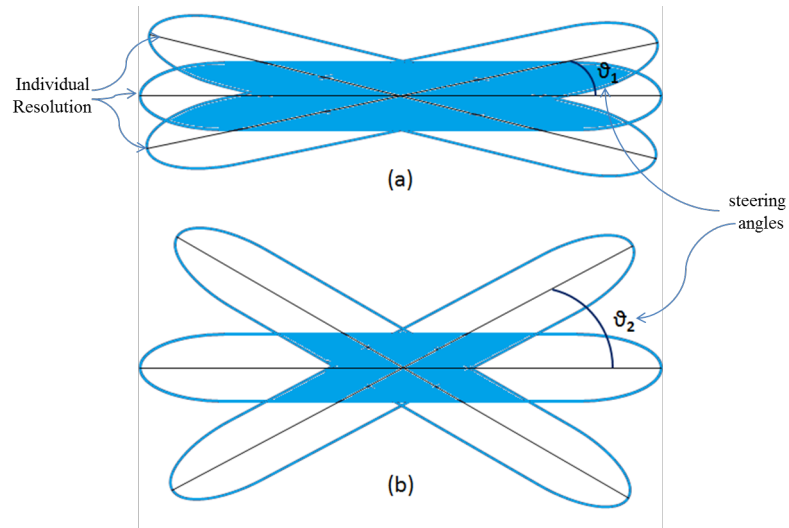


Figure 4.10: The area that represents the interference between the lateral resolutions of three images steered with: (a) $-\theta_1, 0, +\theta_1$ (b) $-\theta_2, 0, +\theta_2$, where: $\theta_2 > \theta_1$

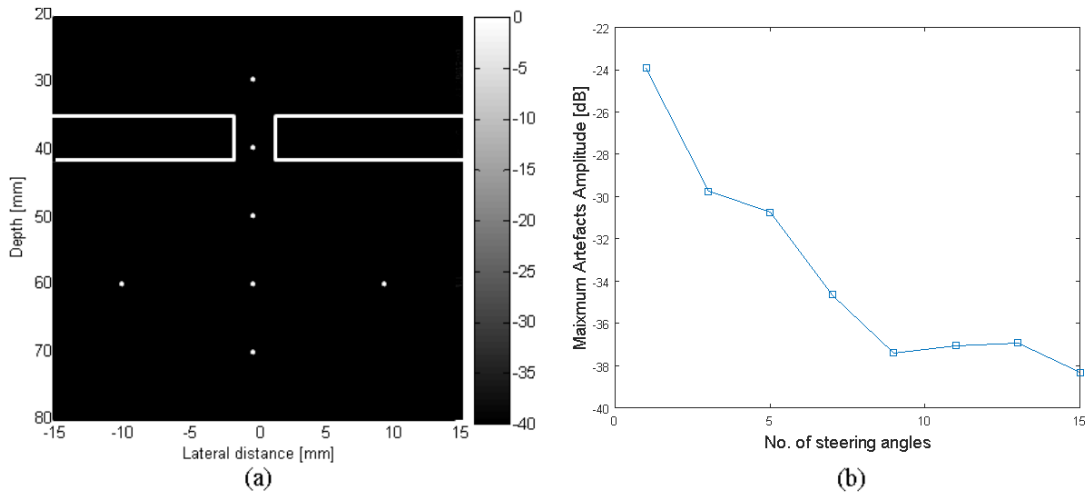


Figure 4.11: (a) The two rectangles at the sides of the 40mm depth point, at which the maximum of artefacts is measured as given in (b) when compounding different numbers of angles.

decrease with increasing the number of elements in the aperture as more data is used to produce each scan line. In unfocused imaging when all the elements are used for a single transmission and reception, the artefacts appear at the sides of the scattering points. The location of these artefacts is steered with steering the transmitted beam. Therefore, they are cancelled during the compounding operation in CPWI.

The curve that relates the maximum artefacts intensity at the sides of the 40mm depth points and the number of compounded angles is shown in figure 4.11(b). The two areas at which the maximum artefacts intensity is measured are from the 37.5 to 41mm depth, starting from the -30dB intensity drop of the point, as given by the white rectangles in figure 4.11(a). The artefacts curve has a logarithmic behaviour, where the decrease in the artefacts maximum with increasing the number of compounded angles becomes insignificant after compounding specific number of angles. This is because the step between the steering angles becomes small and causes the artefacts to interfere as explained in section 4.2.3. From the limit where the improvement becomes insignificant, the number of compounded angles can be specified. From the curve, this number can be chosen to be 11 angles.

4.4 Conclusions

The quality of the produced ultrasound images in CPWI is mainly dependent on the steering angles of the compounded frames. In order to assure ultrahigh frame rates for CPWI, the required imaging quality needs to be achieved using the minimum number of frames. In addition, for a specific number of angles, the use of a wider angular range helps increasing the step between the steering angles, which enables achieving a better lateral resolution and efficient artefacts reduction.

The first step for specifying the steering angles is to find the maximum possible steering angle or the angular range within which steering will be done. Secondly, the number of the compounded angles that will be selected within this range are specified depending on the limit after which no more improvement is added to the quality, measured in lateral resolution and level of artefacts for a PSF.

Several factors need to be considered when specifying the angular range in CPWI. The first is the maximum possible steering angle for the transducer, which is usually given by the manufacturer. Secondly, the amount of medium attenuation added to the signal at the required imaging depth, and finally, the transducer sensitivity or the minimum distinguishable intensity by the receiver. These factors are considered by first plotting the maximum received intensity at the required imaging depth versus the steering angles for the required imaging system using Field II simulation. Then the angle corresponding to the intensity that resembles the transducer sensitivity plus the medium attenuation is considered as the maximum steering angle.

As compared to conventional linear imaging, CPWI is able to provide ultrahigh frame rates that are necessary for many recent applications. In addition, a superior imaging quality is provided due to compounding multiple signals with different steering angles. The produced imaging quality in terms of lateral resolution and level of artefacts is highly affected by the angular range and the step between the angles. Unlike in linear imaging where the image width is affected by the number of elements in the aperture, the produced images widths in CPWI are not affected by the imaging parameters like the number or values of the compounded angles.

Part II

Minimum Variance Adaptive Beamforming Techniques

Adaptive beamformers have been widely used recently in different fields. Examples on these fields include wireless communications, photoacoustic imaging, speech processing, radar and sonar applications (Lo, 2004; Mehdizadeh *et al.*, 2012b; Park *et al.*, 2008; Ser *et al.*, 2007), in addition to ultrasound imaging.

In DAS beamformer as explained previously, the image is formed by delaying the RF signals received from each of the aperture channels and summing the resultant values. These received signals are weighted with apodization weights that are related to the location of the receiving element, higher weights are given to the signals coming from the central elements, while lower weights are given to the signals coming from the elements located farther from the centre. This apodization is done to provide better imaging quality by reducing the sidelobe level. However, the apodization weighting is predefined, data-independent and has the drawback of increasing the width of the mainlobe and thus reducing the lateral resolution of DAS beamformer. This can be avoided by using adaptive beamformers, where the set of the apodization weights is updated for each point in the image, depending on the input RF data (Holfort *et al.*, 2008b). The use of data-dependent weighting vectors in adaptive beamforming results in higher spatial resolution and lower sidelobe levels compared to conventional DAS.

One of the most common adaptive beamformers is the Minimum Variance (MV), which was first introduced by Capon (1969). It is so called due to its minimization of the output power depending on which, the weighting vector is calculated, whilst preserving the response from the focal point.

Several methods have been investigated recently for supporting the MV beamformer and producing improved performance in terms of contrast and/or resolution. These methods are the CPWI, Coherence Factor (CF) and Eigenspace-Based Minimum Variance (ESBMV).

The first chapter in this part of the thesis is dedicated to explain the background and properties of MV adaptive beamforming intensively, supported by Field II simulation examples, while a detailed comparison among the different types of coherence-based factors is given in chapter 6 using experimental RF-data. In chapter 7, a proposed technique of Partial Eigenspace Based Minimum Variance (PESBMV) is introduced to overcome the limitations of the already ex-

isting method of ESBMV and thus enable for efficient medical ultrasound imaging using MV adaptive beamforming.

Chapter 5

Minimum Variance Adaptive Beamforming: Background and Properties

In adaptive beamformers, data-dependent weighting vectors are used during the apodization operation. This weight is derived from an assumption that varies depending on the type of the adaptive beamformer (Madisetti, 2009). In Minimum Variance (MV) beamforming, the weighting vector is derived from the optimization equation which assumes that the output power is minimized, subjected to the constraint that the output from the look direction is preserved.

MV beamformer have been widely studied in the past years in medical ultrasound imaging research. Synnevåg *et al.* (2007) explained the advantages of introducing higher contrast and resolution when using MV compared to DAS. They also discussed two methods used for improving the robustness in MV. The effect of MV on speckle statistics compared to DAS was demonstrated by Synnevåg *et al.* (2007), with explaining the effect of temporal and spatial smoothing operations on these statistics. Synnevåg *et al.* (2009) also demonstrated that a similar quality level to that in DAS can be achieved using smaller apertures, lower transmitted frequencies or larger penetration depths when MV beamforming is used.

MV beamforming can be performed in either the time domain or frequency domain. In time domain implementation, the received vectors of data or sensor

5.1 Minimum Variance (MV) Beamformer Background Method

signals are directly used to find the weighting vector and then the output value for each $p(x, y)$. In frequency domain implementation on the other hand, the sensor signals are converted to the frequency domain using Fourier transforms, after the dynamic focusing delays are applied. Then the operation of calculating the weighting vector as well as the output vector is performed in the frequency domain. Afterwards, the inverse Fourier transform is applied to the weighted output vector and the central sample of the resulted vector in time domain is taken as the final output. A detailed explanation for the MV background method and properties using the frequency domain implementation was introduced by [Holfort *et al.* \(2009\)](#) using Field II simulation experiments. The two types of MV implementations were compared using Field II simulations in another study by [Diamantis *et al.* \(2014\)](#). In this study, it was shown that very similar results can be achieved from the two MV implementation methods. This makes the use of time domain implementation more efficient in terms of the computational complexity, as no Fourier transforms are required. Therefore, the time domain implementation of MV beamforming is the method used during this thesis.

In this chapter, the background and properties of MV beamforming method are given in details. The operations of subarray averaging, temporal smoothing and diagonal loading are also discussed in detail in this chapter with their advantages and drawbacks, supported by Field II simulation examples using point targets model.

5.1 Minimum Variance (MV) Beamformer Background Method

In MV beamformer, the weighting vector for each $p(x, y)$ is continuously updated so that the output power is minimized whilst preserving a unity gain for the response from the focal point. This condition can be explained mathematically as an optimization problem in the following formula ([Holfort *et al.*, 2009](#); [Sasso & Cohen-Bacrie, 2005](#); [Synnevag *et al.*, 2007](#)):

5.1 Minimum Variance (MV) Beamformer Background Method

$$\begin{aligned} \min_w w^H R w \\ \text{subject to } w^H e = 1, \end{aligned} \quad (5.1)$$

where w is the weighting vector, R is the covariance matrix, $\{\cdot\}^H$ is the conjugate transpose operation. Variable e is called the steering vector and it is used to compensate for the delays of the responses from the focal point for each receiving element. Because the delays are applied to the RF-data at the start of the beamforming, e becomes a vector of ones.

Solving the optimization problem in equation (5.1) using Lagrangian multiplier theory leads to the following formula for the MV weight (Holfort *et al.*, 2009; Synnevag *et al.*, 2007):

$$w = \frac{R^{-1}e}{e^H R^{-1}e}. \quad (5.2)$$

The covariance matrix (R) is estimated from the data by following the steps of the spatial smoothing approach (Shan & Kailath, 1985) as follows: First, the transducer array of elements are divided into P overlapped groups or subarrays, each subarray is equal to its adjacent subarray but shifted with one element, as shown in figure 5.1. After subarray smoothing is applied, the covariance matrix is approximated from the data using the following equation (Holfort *et al.*, 2009; Synnevag *et al.*, 2007):

$$R = \frac{1}{P} \sum_{p=0}^{P-1} G_p G_p^H, \quad (5.3)$$

where P is the number of subarrays and it equals to $(N - L_p + 1)$ and G_p is the p^{th} subarray given by (Holfort *et al.*, 2009; Synnevag *et al.*, 2007):

$$G_p = [y_p(n) \quad y_{p+1}(n) \quad \dots \quad y_{p+L_p-1}(n)]', \quad (5.4)$$

where $y_p(n)$ is a segment from the input signal received by the p^{th} element, $p = 0, 1, \dots, P - 1$. Each $y_p(n)$ is a vector with the length of $(2K + 1)$. $\{\cdot\}'$ denotes the transpose operation. It can be noticed that this operation of subarray smoothing has the effect of reducing the size of the covariance matrix to $L_p \times L_p$ and thus the size of the produced weighting vector w is reduced correspondingly to $L_p \times 1$.

5.1 Minimum Variance (MV) Beamformer Background Method

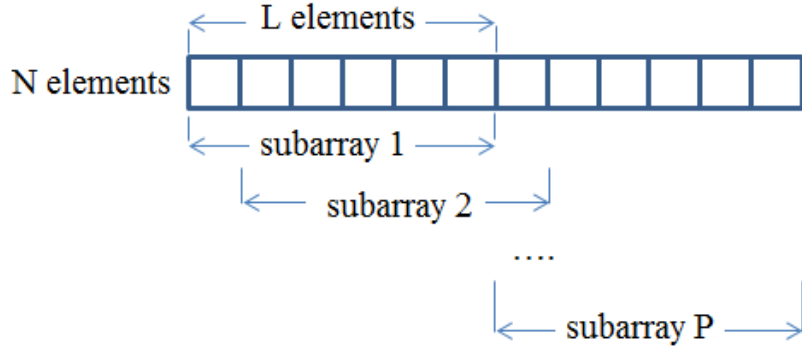


Figure 5.1: The operation of subarray smoothing that divides the transducer elements into P subarrays, each of them consists of L_p elements.

After the weighting vector is calculated, the output value of the beamformer for the required focal point at (x, z) is calculated by multiplying the average of the subarrays by the weighting vector as follows (Holfort *et al.*, 2009; Synnevag *et al.*, 2007):

$$Y(x, z) = w' \frac{1}{P} \sum_{p=0}^{P-1} G_p. \quad (5.5)$$

This equation yields a vector $Y(x, z)$ with an odd length that equals to the number of temporal smoothing samples $(2K + 1)$. The central sample of this vector is taken as the final output of MV beamformer for $p(x, y)$. Table 5.1 gives the sizes of all the variables used during the MV beamforming to help in understanding the operations explained above.

A schematic diagram that shows the beamforming steps of applying the focusing delays to the received signals, the weighting operation and the calculation of the output value in DAS and MV beamformers are shown in figure 5.2. The main differences between the two beamformers as shown in this figure are: the use of predefined weights in DAS in (a), and that the signals after applying focusing delays $y_i(n)$ are scalars, while in MV in (b), the weighting vector is calculated from the data during the beamforming operation and, after applying the focusing delays, $y_i(n)$ are all vectors of length $(2K + 1)$, due to the use of temporal

5.2 Temporal Smoothing in MV

Table 5.1: *THE SIZES OF THE VARIABLES USED DURING THE MV BEAMFORMING OPERATION.*

Variable	Size
Weighting vector (w)	$L_p \times 1$
Covariance matrix (R)	$L_p \times L_p$
Steering vector (e)	$L_p \times 1$
Subarray (G_p)	$L_p \times (2K + 1)$
Input segment ($y_i(t)$)	$1 \times (2K + 1)$
Output vector ($Y(x, z)$)	$1 \times (2K + 1)$

smoothing.

5.2 Temporal Smoothing in MV

In temporal smoothing, instead of taking a single input sample from each data line when applying the focusing delays, a vector of samples of length $(2K + 1)$ is selected, with the response from the focal point located at the centre of this vector, *i.e.*:

$$y_i(n) = x_i(n), \quad n \in [-K; +K], \quad (5.6)$$

where x_i is the signal received by the i^{th} element. As $y_i(n)$ is from $-K$ to $+K$, the response received from the focal point will be at $n=0$. The length of the vector $y_i(n)$ should be no longer than the pulse length, in order to preserve axial resolution. Therefore, it is usually chosen to be less or equal to the duration of the convolution between the excitation signal and the 2-way impulse response of the transducer (Holfort *et al.*, 2009).

Temporal smoothing in MV beamforming is used to give a homogeneous speckle pattern similar to that achieved using conventional DAS (Li & Stoica, 2005; Wan *et al.*, 2015), whilst preserving the high resolution of MV. When no temporal smoothing is required, the value of K is set to 0.

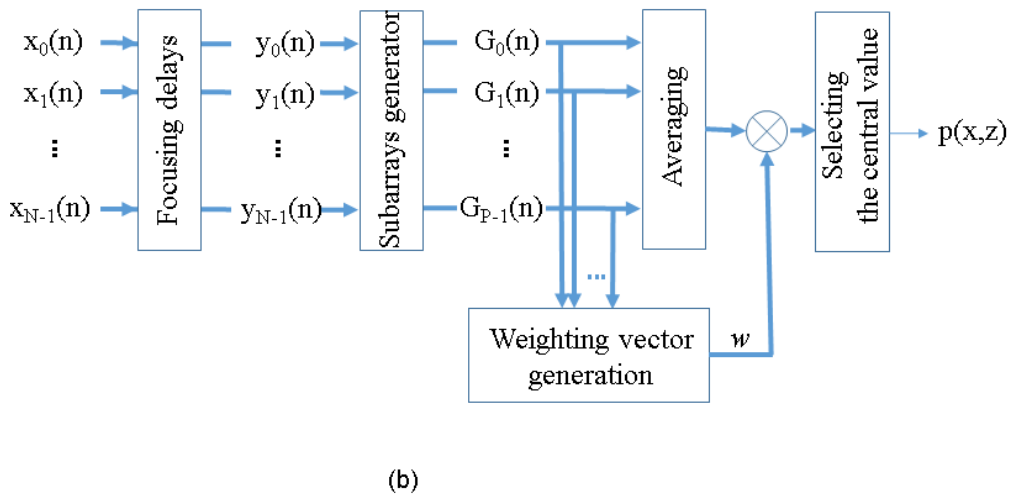
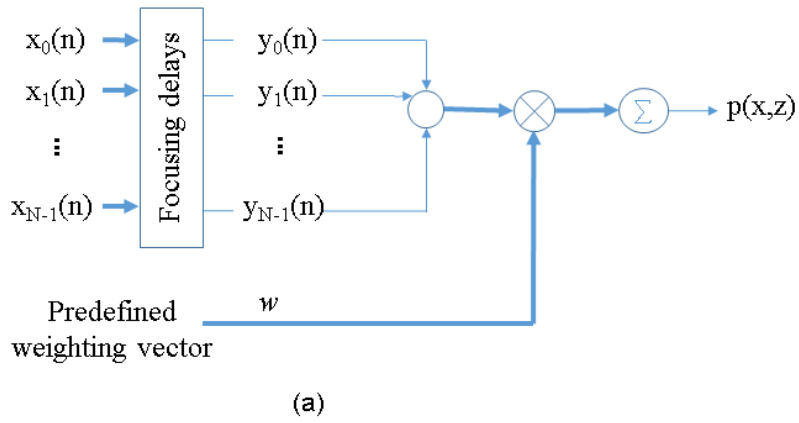


Figure 5.2: A schematic diagram that shows the steps followed during: (a) DAS beamforming and (b) MV beamforming.

5.3 Spatial Smoothing in MV

The main benefit of subarray averaging or spatial smoothing is the reduction of the problem of signal cancellation. Signal cancellation happens when coherent signals arrive at slightly different phases at the surface of the transducer elements, resulting in under estimating the energy of the overall signal (Cheng *et al.*, 2011). Signal cancellation is a common problem in adaptive beamformers due to the use of data-dependent weighting. However, the effect of signal cancellation becomes negligible when using smaller apertures. Therefore, subarray averaging is performed in MV beamformer by dividing the aperture into subapertures of L_p length.

The length of the subarray is used to control both spatial resolution and robustness that are inversely proportional to each other. Increasing L_p , which equally means reducing the number of subarrays, helps improving the imaging resolution at the cost of reducing the robustness of the beamformer (Synnevag *et al.*, 2007, 2009). As the value of L_p decreases, the response becomes nearer to the DAS beamformer (Synnevag *et al.*, 2007). A MV beamforming with a subarray length of 1 equates to the DAS beamforming with uniform weighting (no apodization).

The maximum limit of L_p is half the number of the transducer elements (Synnevag *et al.*, 2007). This is to ensure that the covariance matrix R is invertible.

5.4 Robustness in MV

Robustness is defined as the ability of the beamformer to maintain the imaging quality in the presence of errors such as array steering vector errors, distorted transducer shape, wavefront distortions and sound speed estimation errors (Li & Stoica, 2005). The presence of such errors leads the adaptive beamformer to eliminate the signal of interest considering it an off-axis signal instead of preserving a unity response for it, which results in a significant degradation in the produced imaging quality. The performance of adaptive beamformers can also be highly degraded by the motion or vibration that may occur in the channel and/or environment, which is common in sonar, radar and wireless communication systems

5.5 Computational Complexity of MV

(Li & Stoica, 2005) and therefore may be a problem when applying to medical imaging of dynamic organs (e.g. heart). Despite the low resolution that result from reducing the subarray size, it leads to improving the robustness of adaptive beamformers, as less number of elements and thus less errors are present in each subarray. Therefore, a trade-off between lateral resolution and robustness exists in MV beamformer, due to the use of subarray smoothing.

In order to improve the robustness in MV beamformer without reducing the subarray length, several methods are produced in the literature, such as the Amplitude and Phase Estimation Beamforming (APES) and Forward-Backward Averaging (FB) (Holfort *et al.*, 2008a; Li & Stoica, 2005). However, the most commonly used method is the Diagonal Loading (DL) (Asl & Mahloojifar, 2009, 2012; Holfort *et al.*, 2008a; Synnevag *et al.*, 2007, 2009). In this method, the covariance matrix R is replaced by the loaded covariance matrix R' . This matrix is found by adding a load that is proportional to the power included in the received signal to the covariance matrix R , *i.e.* (Asl & Mahloojifar, 2009):

$$R' = R + \Delta \text{tr}\{R\}I, \quad (5.7)$$

where $\text{tr}\{R\}$ is the trace of R which represents the sum of the diagonal elements, I is the identity matrix and Δ is used to control the amount of diagonal loading. The value of Δ is usually chosen to be a constant multiplied by $1/L_p$ (Synnevag *et al.*, 2007), and it is used to control the amount of the applied DL.

A drawback of the diagonal loading method is that it slightly decreases the mainlobe width and leads to a reduced lateral resolution. At the same time, the enhanced robustness improves the ability of MV to resolve targets in the presence of system errors that lead to underestimating targets reflectivity when no DL is used (Synnevag *et al.*, 2007).

5.5 Computational Complexity of MV

Despite the ability of adaptive beamforming to increase the resolution and reject interference signals, DAS is still more commonly used in most medical imaging applications. This is due to the high computational complexity of MV, which

increases the computational burden on the processor and makes it unsuitable for real time applications.

The computational complexity in DAS beamformer increases linearly with the number of the transducer elements, it is a function of (L_p^3) in MV beamformer. Therefore, decreasing the number of elements in each subarray during the MV beamforming helps reducing its computational complexity in addition to improving the robustness, but at the cost of reducing the lateral resolution, which is directly proportional to the number of elements in the subarray (Synnevag *et al.*, 2007, 2009). In the literature, several research groups have investigated the use of various low-complexity techniques to increase the computational efficiency of MV beamforming whilst preserving the produced imaging quality (Asl & Mahloojifar, 2012; Synnevag *et al.*, 2011; Zeng *et al.*, 2013), which opens the way for real time implementations of MV beamforming.

5.6 Field II Simulations

In order to clarify the efficiency of MV beamforming in resolution enhancement and sidelobe reduction compared to DAS, Field II program was used to simulate the ultrasound imaging of a point scattering model using PWI with the two types of beamformers.

A linear array transducer with 128 elements, 5MHz central frequency, 100% bandwidth, 100MHz sampling frequency and a pitch of half the wavelength was used during the simulations. DAS with two types of receive apodization windows, Boxcar and Hamming, were simulated for comparison, while MV beamforming was performed with various temporal smoothing lengths and subarray lengths. For both beamformers, no apodization was performed during transmitting the beam. All the 128 elements were used during the transmission and reception, with no focusing at the transmit and a dynamic focusing at the receive. The excitation signal was a 2-cycles Gaussian pulse. Additional white Gaussian distributed noise with SNR of 60dB was added to the received signals before the beamforming is performed. A medium sound speed of 1540m/s was assumed.

5.7 Results

Ultrasound images of a point scattering model were produced with Field II using DAS and MV beamformers. The model contained seven scattering points. Five of these points are located at the 30, 35, 40, 45 and 50mm depths perpendicular to the middle of the transducer ($x=0$), while two other scatterers are located at $x=\pm 3$ mm and 45mm depth.

Images (a) and (b) in figure 5.3 show the results of using DAS beamforming with Boxcar and Hamming apodization windows respectively, at the receive. MV beamforming results are shown in figure 5.3 (c-e) using three different subarray lengths of 32, 48 and 64 elements, with a temporal smoothing of ($K=60$) due to the use of a 121 samples pulse. This pulse results from convolving the excitation signal with the two-way impulse response of the transducer. In figure 5.3 (f-h), MV beamforming is repeated at the same subarray lengths with no temporal smoothing ($K=0$). The images in this figure are all produced with a dynamic range of 50dB.

The lateral variations for the point located at the 40mm depth for the beamformers used in figure 5.3 are given in figures 5.4 and 5.5, in order to clarify the effect of using MV with various subarray lengths and temporal smoothing coefficients on lateral resolution and sidelobe levels. The beamforming performance at this depth was also evaluated in terms of resolution and sidelobe levels using FWHM and Peak-SideLobe Level (PSLL) (Harput *et al.*, 2014). These measurements are given in table 5.2, where PSLL is equal to the amplitude of the first sidelobe, measured in dB.

For the two cases of the temporal smoothing used in figure 5.3, $K=60$ and $K=0$, the use of diagonal loading is simulated with a subarray length of 64 element, where the lowest level of robustness is achieved. Figure 5.6 shows the results of these simulations, where three different amounts of diagonal loading are used: ($\Delta=1/20L_p, 1/10L_p$ and $1/L_p$). The lateral variation for the 40mm depth point is shown for these cases in figures 5.7 and 5.8, for $K=60$ and $K=0$, respectively. Furthermore, the FWHM and PSLL are measured at the 40mm depth as given in table 5.3, in order to show the exact effect of the applied amounts of DL on the imaging quality.

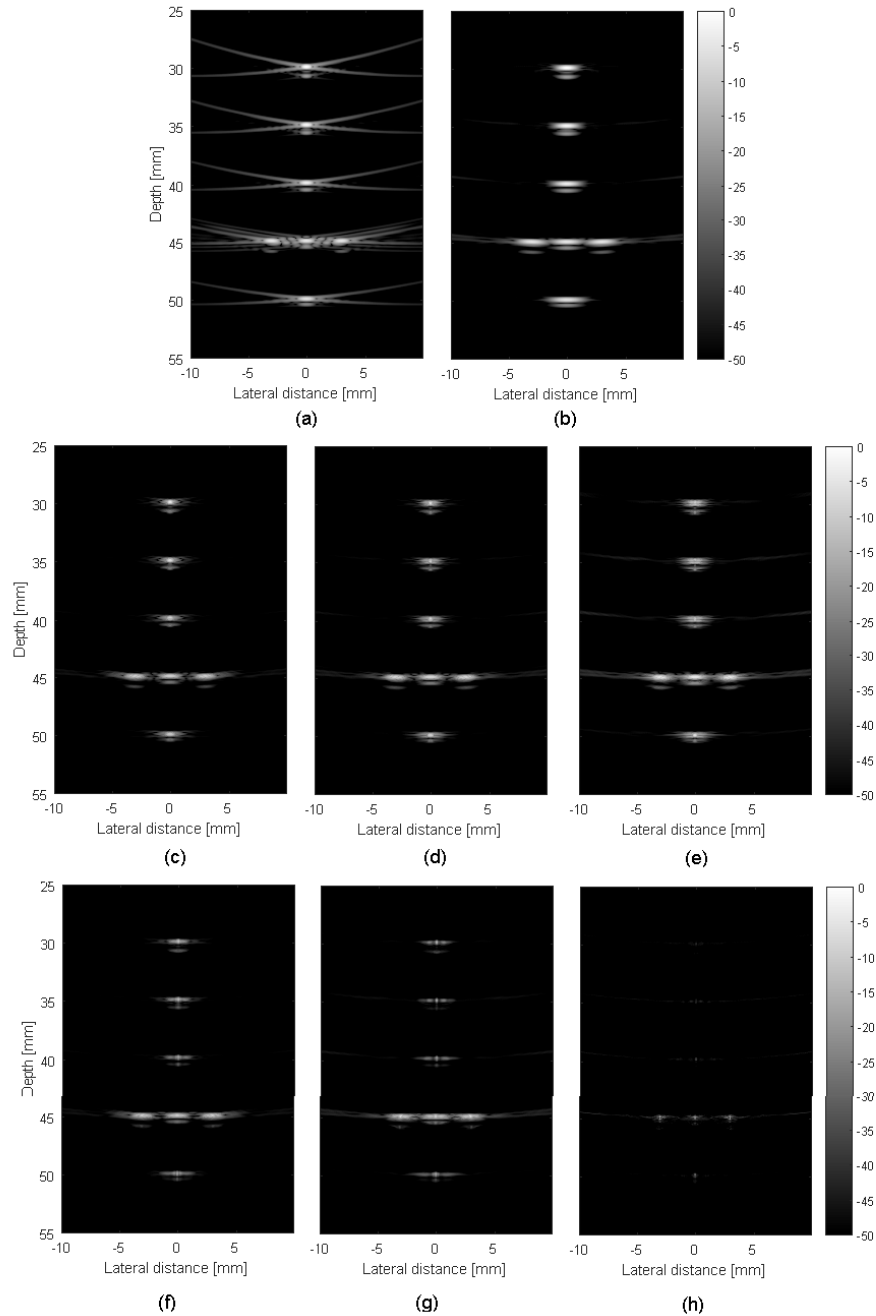


Figure 5.3: Field II simulated point targets using: (a) DAS with Boxcar receive apodization, (b) DAS with Hamming receive apodization, (c) MV ($L_p=32$, $K=60$), (d) MV ($L_p=48$, $K=60$), (e) MV ($L_p=64$, $K=60$), (f) MV ($L_p=32$, $K=0$), (g) MV ($L_p=48$, $K=0$), (h) MV ($L_p=64$, $K=0$). All images are produced with 50dB dynamic range.

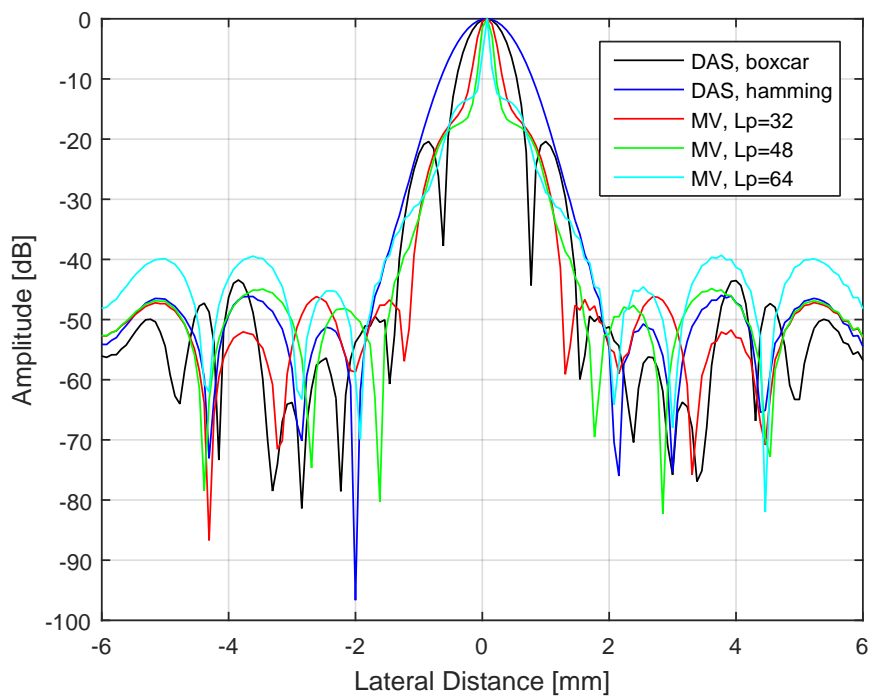


Figure 5.4: Comparing the lateral resolution of DAS and MV for the 40mm depth point shown in figure 5.3, for images: *a* and *b* for DAS and *c*, *d* and *e* for MV produced with temporal smoothing of $K=60$.

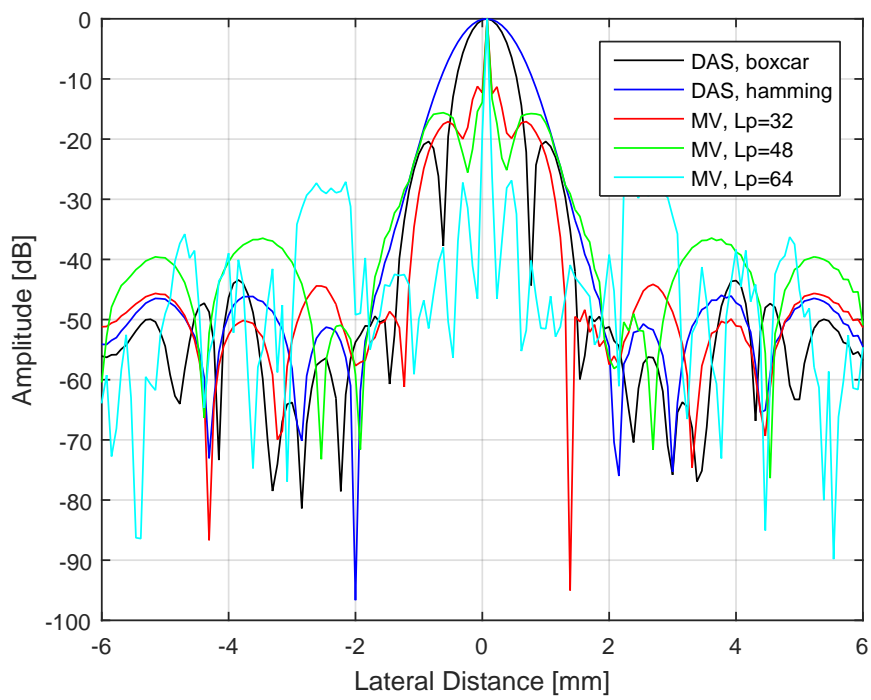


Figure 5.5: Comparing the lateral resolution of DAS and MV for the 40mm depth point shown in figure 5.3, for images: *a* and *b* for DAS and *f*, *g* and *h* for MV produced with temporal smoothing of $K=0$.

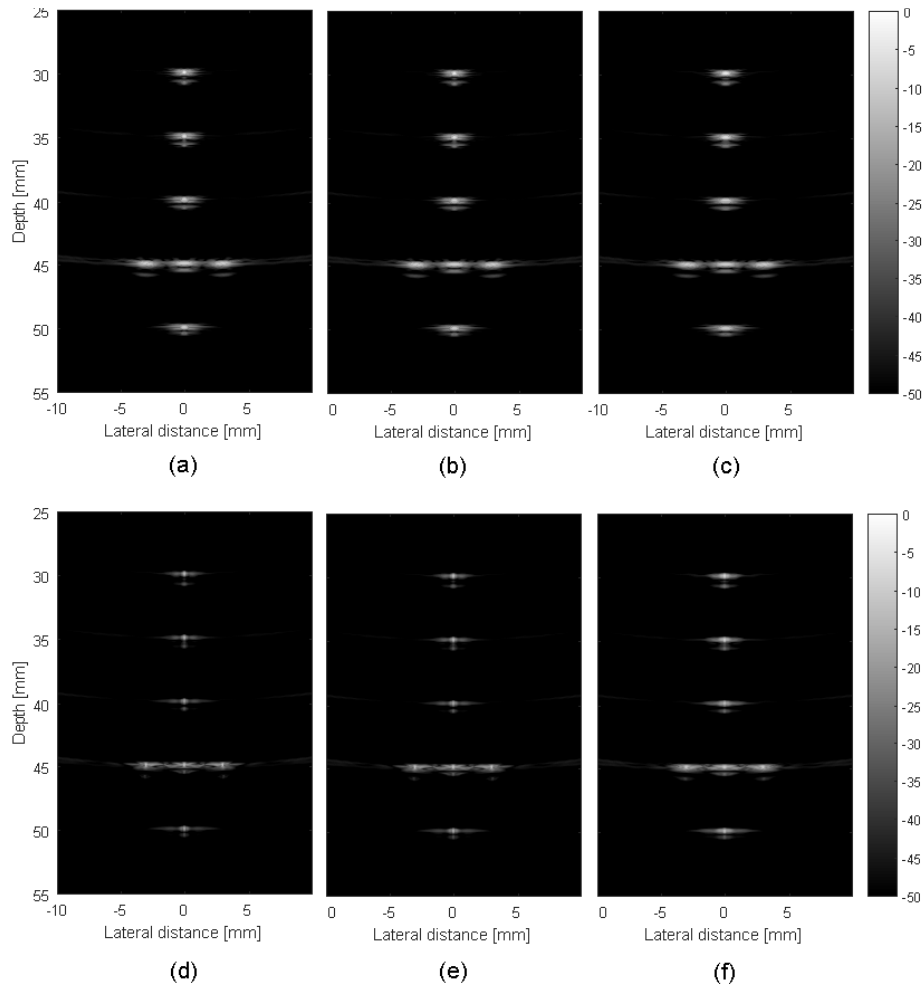


Figure 5.6: Simulated point targets using MV beamformer in the presence of various amounts of Diagonal Loading with the subarray length being 64 elements. (a) $K=60, \Delta=1/20L_p$, (b) $K=60, \Delta=1/10L_p$, (c) $K=60, \Delta=1/L_p$, (d) $K=0, \Delta=1/20L_p$, (e) $K=0, \Delta=1/10L_p$, (f) $K=0, \Delta=1/L_p$. All images are produced with 50dB dynamic range.

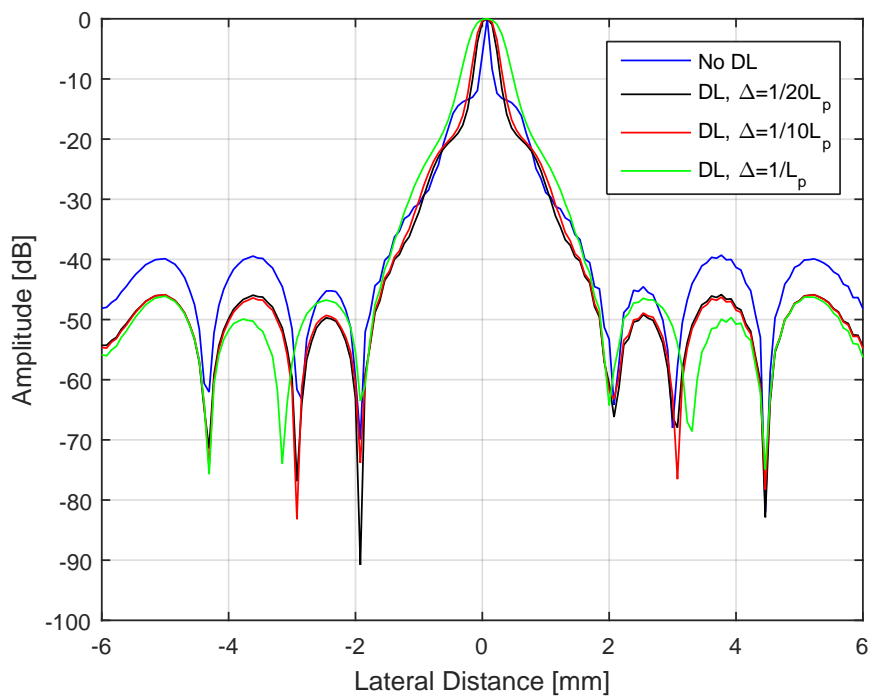


Figure 5.7: Comparing the lateral resolution of MV beamformer for the 40mm depth point shown in figure 5.6, in the presence of different amounts of Diagonal Loading. $L_p=64$ element and $K=60$.

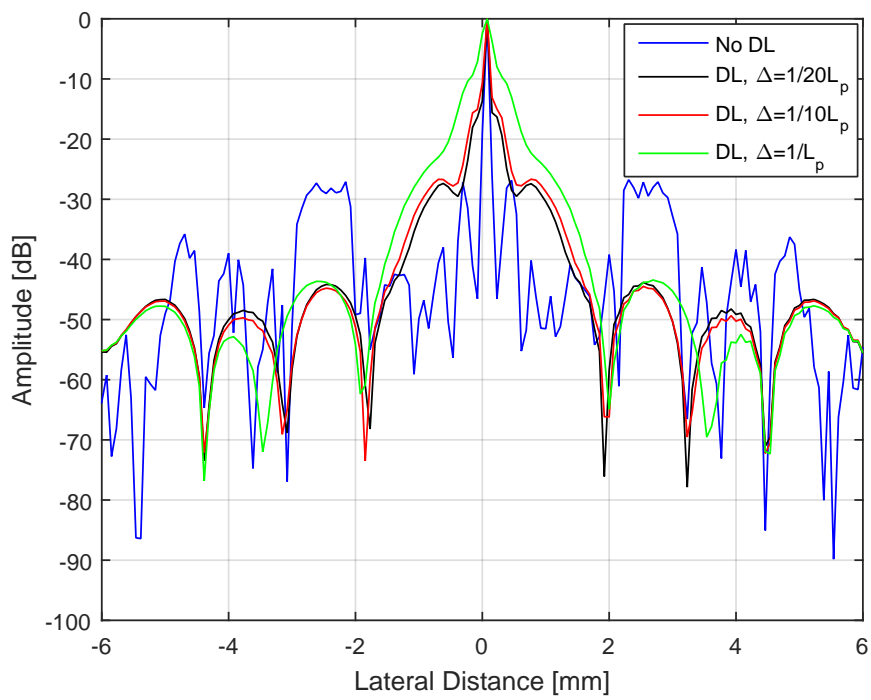


Figure 5.8: Comparing the lateral resolution of MV beamformer for the 40mm depth point shown in figure 5.6, in the presence of different amounts of Diagonal Loading. $L_p=64$ element and $K=0$.

Table 5.2: *FWHM AND PSLR FOR THE POINT LOCATED AT THE 40mm DEPTH, FOR THE BEAMFORMERS SHOWN IN FIGURE 5.3.*

Beamformer	FWHM (mm)	PSLL (dB)
DAS, Boxcar	0.76	-20.39
DAS, Hamming	1.12	-45.96
MV ($L_p = 32, K = 60$)	0.38	-46.17
MV ($L_p = 48, K = 60$)	0.23	-44.85
MV ($L_p = 64, K = 60$)	0.13	-39.29
MV ($L_p = 32, K = 0$)	0.075	-11.24
MV ($L_p = 48, K = 0$)	0.068	-15.62
MV ($L_p = 64, K = 0$)	0.042	-26.76

L_p is the subarray length,

K is the temporal smoothing coefficient.

Table 5.3: *FWHM AND PSLR FOR THE POINT LOCATED AT THE 40mm DEPTH IN THE PRESENCE OF DIFFERENT AMOUNTS OF DIAGONAL LOADING, FOR THE BEAMFORMERS SHOWN IN FIGURE 5.6.*

Beamformer	FWHM (mm)	PSLL (dB)
MV, ($K=60$, No DL)	0.13	-39.29
MV, ($K=60, \Delta = 1/20L_p$)	0.34	-45.84
MV, ($K=60, \Delta = 1/10L_p$)	0.40	-45.87
MV, ($K=60, \Delta = 1/L_p$)	0.67	-46.12
MV, ($K=0$, No DL)	0.042	-26.76
MV, ($K=0, \Delta = 1/20L_p$)	0.063	-27.38
MV, ($K=0, \Delta = 1/10L_p$)	0.078	-26.67
MV, ($K=0, \Delta = 1/L_p$)	0.25	-43.43

$L_p=64$ elements.

5.8 Discussion

In this work, Field II simulations of point target models are used to compare the imaging quality of the MV beamformer with the non-adaptive beamformer of DAS. The results of these simulations are shown in figure 5.3. No apodization at the transmission in either of the two beamformers was used, which results in the artefacts that can be seen below the point scatterers in this figure. These artefacts represent the effect of the grating lobes that result in producing replicas of any strong scattering object exist in the image in a shifted location. The use of the transmit apodization is the solution to eliminate or reduce this effect of the grating lobes. However, it was not used because of its drawback of reducing the amount of the transmitted power and thus limiting the imaging penetration depth. In addition, it is required to show the efficiency of MV in reducing these artefacts without the use of any kind of transmit apodization.

The effect of using receive apodization can be seen from the two DAS images in figure 5.3 (a) and (b), where two types of apodization windows are used, Boxcar and Hamming. When using Hamming window, the level of artefacts is significantly reduced compared to that when using Boxcar window (which has a uniform amplitude of 1), at the expense of degrading the lateral resolution. This degradation is caused by the increase in the mainlobe width due to the use of receive apodization, which reduces the effect of the signals received by the elements at the sides of the transducer. This results in reducing the width of the active receive aperture, with which the lateral resolution is inversely proportional, as shown in chapter 3.

It can be seen from the results that the lateral resolution when using MV adaptive beamformer is higher than that in DAS, even when no receive apodization is used (DAS with Boxcar window), due to the data-dependent weighting of MV. This is confirmed through the lateral variation plot given in figures 5.4 and 5.5, and the measurements of the FWHM given in table 5.2 at the 40mm depth, for the subarray lengths and temporal smoothing vectors used in figure 5.3 (c-h).

When no temporal smoothing is applied ($K=0$) with maximizing the subarray length to 64 elements ($N/2$), the highest resolution and lowest sidelobe level were achieved, as can be seen in figure 5.3 (h). In addition, the artefacts that appear

under the scattering points in the other images of the same figure are completely removed. However, this comes at the cost of reduced robustness, which results in underestimating the amplitudes of the scattering points.

As mentioned earlier, temporal smoothing is used to improve the speckle statistics and contrast in tissue imaging, where a vector of samples instead of a single sample is used to produce the final value of the focal point. For a PSF, this operation has the limitation of degrading resolution, which makes it unsuitable for point targets imaging. This can be noticed by comparing images (c-e) in figure 5.3 where $K=60$ samples, with images (f-h) in the same figure where $K=0$.

The DL operation that enhances the robustness of MV beamformer can be used to improve the problem of underestimating the targets amplitude when large subarray lengths are used. The effect of applying various amounts of DL on the imaging is shown in figure 5.6. It can be seen from this figure that the points amplitudes are better estimated but with lower resolution and sidelobes reduction. This is directly proportional to the amount of the applied DL. In order to further clarify the effect of DL, lateral resolution curves for the point at the depth of 40mm are shown in figures 5.7 and 5.8, when $K=60$ and $K=0$, respectively. These curves show that increasing the amount of the DL by increasing Δ results in further reduction in the lateral resolution. The resolution and sidelobe levels for the images of figure 5.6 are assessed using FWHM and PSLR at the 40mm depth as given in table 5.3. This table shows that the resolution when no temporal smoothing is used is superior to that when $K=60$. Moreover, higher level of sidelobes is produced with the temporal smoothing of ($K=60$), and this level decreases when heavier DL is applied.

An acceptable level of robustness and resolution can be produced either by applying a specific amount of DL, or by lowering the length of the subarrays. In the next two chapters, and in order to achieve a trade-off between resolution and robustness, a subarray length of $N/4$ (32 elements) with no DL is used whenever MV is applied. This is because DL adds more computations to the beamformer, while lowering the subarray length provides a similar effect of DL, in addition to significantly reducing the computational complexity of MV which is a function of L_p^3 .

5.9 Conclusions

Simulations that use point target phantoms are usually employed to reveal the efficiency of the imaging system and beamforming technique in improving resolution and reducing sidelobe levels. In PWI, the use of a single unfocused beam at the transmit helps to provide ultrafast imaging with thousands of frames per second. However, this comes at the expense of reduced imaging quality, which requires the use of efficient beamforming methods to compensate for this quality degradation and produce acceptable or even high quality images that are suitable for medical imaging and diagnostics purposes. Adaptive beamforming is one of these methods that offer improved quality for PWI and is widely used recently in the medical ultrasound imaging research.

The most commonly used adaptive beamformer in the field of ultrasound imaging is the MV, which has the ability to produce superior imaging quality for point targets compared to the non-adaptive beamformer of DAS. The Field II simulations carried out in this chapter show the efficiency of MV beamformer in resolving point targets with high resolution, penetration depth and sidelobe suppression. These properties are controlled by the subarray size and the number of temporal smoothing samples, in addition to the amount of the applied diagonal loading. The simulations of this chapter show the effect of each of these three coefficients on the imaging quality.

In addition to the high computational complexity, another two drawbacks exist in MV beamforming. The first drawback is the robustness that is reduced with increasing the subarray length. For a trade-off between resolution and robustness, either the subarray length is reduced to a specific value, or alternatively, a method that increases the robustness like the diagonal loading can be used, which also reduces the resolution of the imaging. In the following chapters, a subarray length of $(N/4)$ is used for MV beamforming, with no diagonal loading.

The second drawback of MV is having a low contrast that is similar to that in DAS, which results in poor cystic detection and low quality ultrasound images are produced. The next two chapters discuss the methods that are used to resolve this drawback of MV by using different types of techniques, CPWI, coherence based factors and Eigenspace-based MV. In addition, a composite method of

5.9 Conclusions

Partial-ESBMV is proposed to eliminate the drawbacks of reference ESBMV and enable for efficient medical imaging using MV adaptive beamforming.

Chapter 6

Coherence Factor-Based Imaging Combined with Adaptive and Non-Adaptive Beamforming Techniques

Ultrasound imaging is one of the most important methods used in diagnosing cysts and lesions in the human body. In addition to the importance of the operator experience in interpreting ultrasound images in diagnosis, the quality of these images plays an important role during this interpretation. The use of efficient beamforming methods produces high quality ultrasound images, that can together with expert operator lead to a precise diagnoses and thus a suitable medical treatment can be specified.

The low echogenicity of cystic targets as compared to that of the surrounding tissue makes it easy to identify this type of target. However, diagnosis becomes more challenging for small size cysts (of less than 1cm in diameter), where further investigation is required. Early diagnoses and treatment of small cysts is important for preventing possible growth in the size or malignancy transformation.

An important method for improving the performance of beamformers is by weighting their output using adaptive factors that are calculated depending on the received data. In this chapter, different types of recently introduced coherence-based factors are studied and compared from different perspectives for DAS and

MV beamformers. Two sets of experimental RF data were used during this work. The first set of data is related to a wire targets phantom with a speckle background and it is used for assessing both the spatial resolution and imaging artefacts. The second set of RF data is for a cystic phantom with 3mm diameter cyst embedded in a speckle background, and it is used for assessing the imaging contrast and background speckle homogeneity. These assessments are done using various quality metrics for showing the efficiency of the used beamformers and coherence-based factors from different perspectives.

6.1 Background Theory

Since it was introduced by [Hollman *et al.* \(1999\)](#), the Coherence Factor has become the subject of many studies that discussed the properties and applications of this method, and also suggested some modifications that could improve its performance or tackle its drawbacks. The background of the main types of coherence-based factors that are suggested in the literature are explained in the following sections.

6.1.1 Coherence Factor (CF)

Coherence Factor (CF) is an adaptive measure of the coherency of signals. It was first introduced by [Hollman *et al.* \(1999\)](#) as a quantitative measure of ultrasound imaging quality. Recently, CF is widely used for improving the imaging quality in both ultrasound and photoacoustic imaging ([Asl & Mahloojifar, 2009](#); [Avanji *et al.*, 2013](#); [Nilsen & Holm, 2010](#)). CF is calculated from the ratio between coherent and incoherent sums of the RF-signals after applying focusing delays ([Asl & Mahloojifar, 2009](#); [Nilsen & Holm, 2010](#)):

$$CF = \frac{|\sum_{m=0}^{N-1} x_m(n)|^2}{N \sum_{m=0}^{N-1} |x_m(n)|^2} \quad (6.1)$$

where N is the number of elements and $x_m(n)$ is the signal received by the m^{th} element. According to this equation, coherent RF-signals result in increasing the value of the CF, which enables to pass the beamformer output with no distortion. Incoherent signals, on the other hand, lower the value of CF and result in

attenuating the beamformer output. This property in the CF is used to reduce the artefacts and sidelobe levels and improve spatial resolution in point target imaging.

The CF can be used for adaptively weighting the output of any type of beamformer by calculating it for each image point and then multiplying it by the beamformer output at that point:

$$Y_{CF} = CF.Y, \quad (6.2)$$

where Y is the beamformer output and Y_{CF} is the CF-weighted output of the beamformer. All the coherence-based factors explained in the following sections are used for weighting the beamformers by applying equation (6.2), with replacing the CF with the required weighting factor.

Despite the explained benefits of CF, two main drawbacks arise when using this type of adaptive weighting. Firstly, the CF fails to preserve the homogeneity of speckle generating targets, due to their high incoherency that results in reducing the intensity level and increasing the variance. The other drawback is the BBR artefacts that usually appear to the sides of any hyperechoic target that exist in the region of interest. These artefacts result from the incoherency produced by the lesion sidelobes that intersect in this area and result in reducing the value of the CF (Nilsen & Holm, 2010; Xu *et al.*, 2014). Recently, a few of the published papers were introduced to address these CF limitations and propose solutions to overcome them by developing other types of coherence-based factors.

6.1.2 Generalized Coherence Factor (GCF)

The main advantage of GCF, which was first suggested by Li & Li (2003), is that it is generalized to overcome the limitation of CF when dealing with the non-coherency of the background speckle.

Instead of depending on the coherency of the received RF-signals, GCF is calculated from the ratio between the energy in the low-frequency region to the

total energy included in the signal, which can be written as (Li & Li, 2003):

$$\begin{aligned}
 GCF &= \frac{\sum_{k \in \text{low-frequency region}} |X(k)|^2}{\sum_{k=0}^{N-1} |X(k)|^2} \\
 &= \frac{\sum_{k=0}^{M_0} |X(k)|^2}{\sum_{k=0}^{N-1} |X(k)|^2},
 \end{aligned} \tag{6.3}$$

where M_0 represents the cutoff frequency that controls the amount of components included in the low-frequency region and $X(k)$ is the signal in the discrete frequency domain.

GCF considers that the energy included in the low-frequency region is coming from the direction of the mainlobe, while the remaining energy is coming from other directions (off-axis signals). This comes from the fact that the coherent sum of a signal is equal to the value of the DC component of its spectrum, that is:

$$X(0) = \sum_{i=0}^{N-1} x_i(n), \tag{6.4}$$

$$\text{where: } X(k) = \sum_{m=0}^{N-1} x_m(n) e^{-j2\pi km/N}. \tag{6.5}$$

In this way, the GCF is allowed to deal with the non-coherency of the background speckle by simply controlling the value of the cutoff frequency M_0 according to the type of the signal of interest. A detailed study on the effect of M_0 on the performance of GCF by Li & Li (2003) stated that for speckle generating targets, the value of M_0 is chosen between 1 to 3, in order to allow including the incoherent signals of speckle generating targets in the low frequency region (Deylami & Asl, 2016; Wang & Li, 2014). In this chapter, depending on the type of the phantom used, the value of M_0 is selected to be 3.

6.1.3 High Resolution Coherence Factor (HRCF)

In reference coherence factor, the coherent sum of the delayed signals resembles the output value of DAS beamformer with no apodization. In HRCF, the numerator is calculated depending on the output of MV beamformer, as in the following

equation (Nilsen & Holm, 2010; Wang & Li, 2009):

$$HRCF = \frac{N|Y_{MV}|^2}{\sum_{m=0}^{N-1} |x_m(n)|^2}. \quad (6.6)$$

Due to the high resolution provided by MV beamformer as compared to DAS (which resembles the coherent sum), the imaging quality is expected to be improved when using HRCF.

6.1.4 Sign Coherence Factor (SCF)

Phased coherence factor (PCF) is a type of coherent-based factors that was suggested by Camacho *et al.* (2009). PCF depends on the phases of the delayed RF-signals to measure the degree of coherency in phased array transducers. Another form of PCF that can be applied in linear array transducers is the Sign Coherence Factor (SCF), which depends on the signs of the RF-signals in measuring the amount of coherency using the following equation (Camacho *et al.*, 2009; Torbatian *et al.*, 2012):

$$SCF = 1 - \sqrt{1 - \left[\frac{1}{N} \sum_{i=1}^N b_i(k)\right]^2} \quad (6.7)$$

where $b_i(k)$ is a vector containing the sign bits of the RF-signals as follows:

$$b_i(k) = \begin{cases} -1 & \text{if } x_i(k) < 0, \\ +1 & \text{if } x_i(k) \geq 0. \end{cases} \quad (6.8)$$

Regardless of the amplitudes of the RF-signals, the value of SCF ranges between 1 when the signals are of the same polarity (all positive or all negative) and 0 when they are half positive and half negative (indicating high incoherency). In order to control the effect of SCF on the beamformer output, a coefficient P is suggested to be used as follows:

$$SCF = SCF^P. \quad (6.9)$$

The minimum value of P is 0 (no SCF), and the maximum can be as high as half the number of elements (Camacho *et al.*, 2009), where increasing the value of P increases the effect of the incoherent signals on reducing SCF. This is explained in figure 6.1 where SCF^P is calculated when changing P from 1 to 8. For a fair comparison with the other CF types, the value of P is fixed to 1 during the work carried out in this chapter.

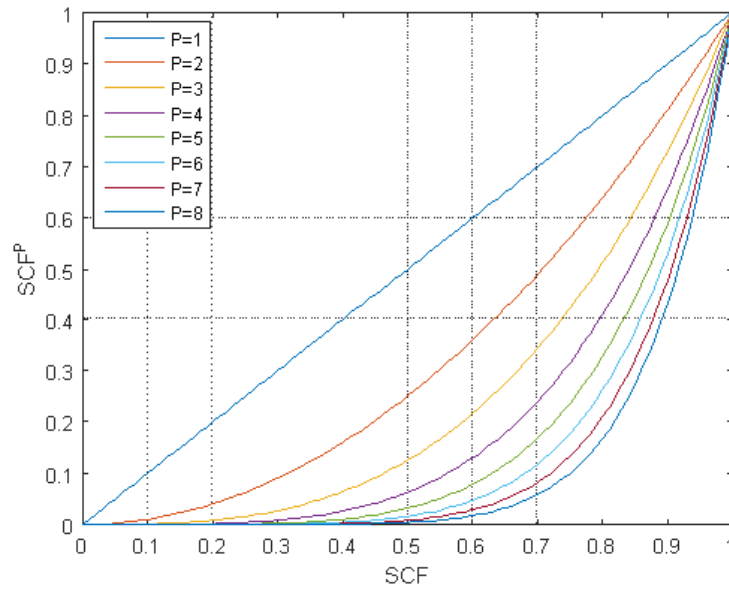


Figure 6.1: The effect of the coefficient P on SCF using equation 6.9, for the values from 1 to 8.

6.1.5 Spatio-Temporally Smoothed Coherence Factor (StS-CF)

In order to depend on more temporal samples when calculating CF, temporal averaging is suggested to be used in StS-CF. This helps in reducing the effect of noise and off-axis signals. In addition, spatial averaging by dividing the elements into P overlapped subarrays is also used. These two averaging methods are followed in reference MV beamformer, in order to improve resolution and reduce noise and sidelobe levels. StS-CF is calculated using the following equation (Xu *et al.*, 2014):

$$StS-CF = \frac{\sum_{k=-K}^K \left| \sum_{l=0}^{N-L_p} \sum_{m=l}^{L_p+l-1} x_m(n+k) \right|^2}{P \sum_{k=-K}^K \sum_{l=0}^{N-L_p} \left| \sum_{m=l}^{L_p+l-1} x_m(n+k) \right|^2}. \quad (6.10)$$

The value of the StS-CF ranges between 0 and 1. K is the temporal smoothing coefficient, P is the number of subarrays and L_p is the subarray length as explained in the previous chapter. By setting K to 0 and L_p to 1, the result of equation (6.10) becomes equal to reference CF.

6.1.6 Scaled Coherence Factor (scCF)

The main problem encountered in the previous CF approaches is that as the noise power increases, and because this power contributes to the total power calculation in the denominator of CF equation, the power of the main signal also decreases as well as off-axis signals. This drawback of CF usually leads to information loss and overall performance degradation.

In order to overcome this limitation, the use of Scaled Coherence Factor (scCF) is suggested by Wang & Li (2014), where a trade off between noise reduction and mainlobe distortion can be achieved. The scCF depends mainly on the Wiener postfiltering concept, that uses the noise output power to control the beamformer output according to the following equation (Nilsen & Holm, 2010; Zeng *et al.*, 2012):

$$H_{Wiener} = \frac{|Y|^2}{|Y|^2 + w^H R_p w}, \quad (6.11)$$

where $|Y|^2$ represents the power of the output signal for the used beamformer. $w^H R_p w$ is the noise output power, with w being the weight of the used beamformer and R_p is the noise covariance matrix calculated by the following equation (Nilsen & Holm, 2010; Zeng *et al.*, 2012):

$$R_p = \frac{1}{N} \sum_{m=1}^N (x_m(k) - Y(k))^2 * I. \quad (6.12)$$

In scCF, a similar form is used to control the value of the CF, where instead of using the noise output power in Wiener postfiltering, an adaptive coefficient

called $\eta(SNR)$ is used for controlling the CF according to the following equation (Wang & Li, 2014):

$$scCF = \frac{CF}{CF + \eta(SNR)(1 - CF)}. \quad (6.13)$$

Using this formula, the benefit of CF in reducing the effect of off-axis signals is achieved, while enabling to maintain the mainlobe energy in the same time. A ratio of the signal power to the noise power P_s/P_n is used for this purpose, where the signal spectrum is divided into signal power region and noise power region. The selection of the cut-off frequency M_0 that is explained in section 6.1.2 is of high importance for the calculation of P_s/P_n ratio. The suitable value for M_0 for tissue phantom imaging is 3 (Li & Li, 2003).

$\eta(SNR)$ is suggested to be calculated using the sigmoid function as follows (Wang & Li, 2014):

$$\eta(SNR) = \frac{N - 1}{2N} \{1 - \tanh[\alpha(\frac{P_s}{P_n} - \beta)]\} + \frac{1}{N}, \quad (6.14)$$

where α and β are two factors controlling the shape of the sigmoid function, with the values of 1 and π , respectively. The output of equation (6.14) ranges between $1/N$ and 1. When the noise power is high, the value of $\eta(SNR)$ approaches 1, enabling to pass the value of CF to scCF with no distortion. High signal power, on the other hand, reduces the effect of CF and enables passing the beamformer output with no distortion. This is because $\eta(SNR)$ becomes nearly $1/N$, which makes scCF almost equal to 1 for most of the CF values. Figure 6.2 shows the values of scCF versus CF when $\eta(SNR) = 1/N$, according to equation (6.13).

6.2 Lab Experiments

6.2.1 Phantoms

Two sets of RF-signals were captured during the lab experiments using Multi-Purpose Multi-Tissue Ultrasound Phantom (Model 040GSE, CIRS Inc., Norfolk, VA, USA). The first set of signals were taken for the part of the phantom shown

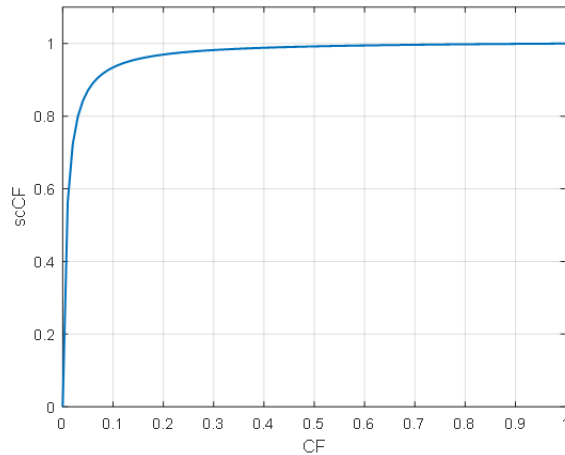


Figure 6.2: scCF versus CF at $\eta(SNR) = 1/N$, according to equation (6.13).

in figure 6.3(a), which contains a 3mm diameter hypoechoic lesion centred at the 17mm depth at $x = -7$ mm and embedded in a speckle generating background with 0.5 dB/cm.MHz attenuation coefficient. This data was used to compare the CF techniques in the speckle mean intensity, CR and CNR, using the four 2x2mm white squares inside and to the left of the cyst shown in figure 6.3(a). Also, the Speckle-Signal-to-Noise Ratio ($SSNR_{Bg}$) is compared using the 5x5mm area shown by the black square at the centre of the image in the same figure.

The second set of RF-signals was taken for the part of the phantom that contains 6 wire targets embedded in the same speckle background at different depths as shown in figure 6.3(b). This set of data was used to assess the resolution and BBR artefacts. Resolution is evaluated using the FWHM for the 23mm depth wire, while the BBR artefacts were measured using the mean intensity of the rectangular area at the side of the 23mm depth wire shown by the black rectangle in figure 6.3(b).

6.2.2 Experimental Setup

Ultrasound imaging experiments were used in this chapter to compare the quality of CF types from different perspectives. The imaging was carried out using L3-8/40EP medical transducer (Prosonic, Korea), derived by the UARP imaging device. The used transducer is of 128 elements, 5MHz central frequency and

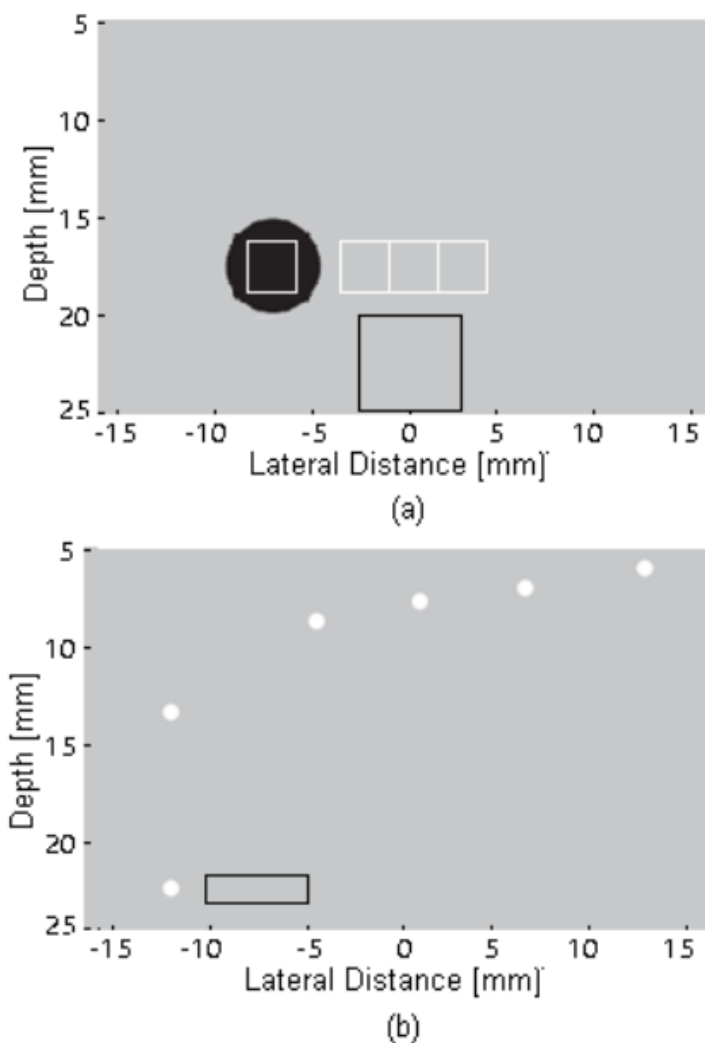


Figure 6.3: The phantom model used for assessing the imaging quality of the coherence-based factors in this chapter. (a) The cystic phantom. (b) The wire-targets phantom.

0.3048mm inter element distance (one wavelength). The excitation signal was two-cycles of sin wave windowed by Gaussian signal, with a sampling frequency of 80 MHz, sound speed of 1540m/s and a transmitted bandwidth of 100%. No focusing was used at the transmission, while dynamic focusing was applied during the beamforming at the receive.

For both DAS and MV beamformers, Directivity Masking (DM) is applied,

which is used to remove any signal received by each single element from more than a specific angle (Hasegawa & Kanai, 2015). This angle is fixed to 45° in this chapter. Apodization is also applied at the receive using Hanning window. For MV beamformer, a fixed subarray length of 32 elements is used, which is equal to $N/4$, with a temporal smoothing vector of 25 samples ($K = 12$), and no diagonal loading was added. CPWI is performed using 7 frames, steered within the $\pm 15^\circ$ angular range, with a step of 5° .

6.3 Quality Metrics

The results are assessed in this chapter using the following quality metrics:

Contrast-to-Noise Ratio (CNR): This metric is used for assessing contrast in the cystic phantom, using the following equation (Wang & Li, 2014):

$$\begin{aligned} CNR &= \frac{CR}{\sqrt{\sigma_{Cyst}^2 + \sigma_{Bg}^2}} \\ &= \frac{|\mu_{Bg} - \mu_{Cyst}|}{\sqrt{\sigma_{Cyst}^2 + \sigma_{Bg}^2}}, \end{aligned} \quad (6.15)$$

where μ_{Cyst} is the mean value of the 2x2mm square area shown in figure 6.3(a) by the white square inside the cyst. μ_{Bg} is the mean of the background speckle inside the three 2x2mm white squares shown to the left of the cyst in the same figure. For accurate measurement, the CNR is calculated for each of these three areas and the results are averaged.

Contrast Ratio (CR): This metric is calculated from the difference between the cyst and background mean values as in equation (6.15), and it is also used to indicate the contrast quality of the imaging.

Speckle Signal-to-Noise-Ratio (SSNR_{Bg}): This metric is used for assessing the quality of the background speckle using the following equation (Lediju *et al.*, 2011; Xu *et al.*, 2014):

$$SSNR_{Bg} = \frac{\mu_{Bg}}{\sigma_{Bg}}, \quad (6.16)$$

where μ_{Bg} and σ_{Bg} are respectively the mean and standard deviation of the area indicated by the 5x5mm black square in figure 6.3(a), measured for the amplitude

detected signal before converting to decibel. $SSNR_{BBR}$ is used for assessing the speckle pattern in the BBR area indicated by the 1.5x6mm black rectangle shown in figure 6.3(b), using the formula given in equation (6.16).

Full Width at Half Maximum (FWHM): This metric is used to measure the lateral resolution for the wire located at the 23mm depth in the wire-targets phantom shown in figure 6.3(b), where the other points in this phantom are considered of a shallow depth for ultrasound imaging in general. Axial resolution is not included in the calculations, since it is only affected by the bandwidth of the transmitted signal, which was fixed during the experiments.

6.4 Results and Discussion

6.4.1 Using Coherence-Based Factors with DAS Beamformer

The first phantom used to examine the properties of coherence-based factors is the cystic phantom shown in figure 6.3(a). This phantom that includes a 3mm diameter anechoic cyst located in a speckle generating background can reveal important properties of the imaging quality, through measuring the SSNR, mean value of the cystic area and background, CR and CNR. For the wire-targets phantom shown in figure 6.3(b), mean value, standard deviation and SSNR of the BBR and FWHM are used for assessing the imaging quality. This is because BBR artefacts only appear to the sides of hyperechoic objects when using CF, so that they do not appear in the cystic phantom.

The use of DAS beamformer for imaging the cystic phantom results in high mean value of -22.92dB inside the cyst due to the presence of noise. However, the background speckle is highly homogeneous with a mean value of -12.12dB, which results in a high SSNR and acceptable values for CR and CNR compared to CF results, as given in table 6.1.

The use of CF with DAS in the cystic phantom decreases the cystic mean and results in better cystic border definition. This is due to the efficiency of CF in improving resolution and reducing the effect of undesired off-axis signals. However, due to being highly incoherent, the amplitude level of the background

6.4 Results and Discussion

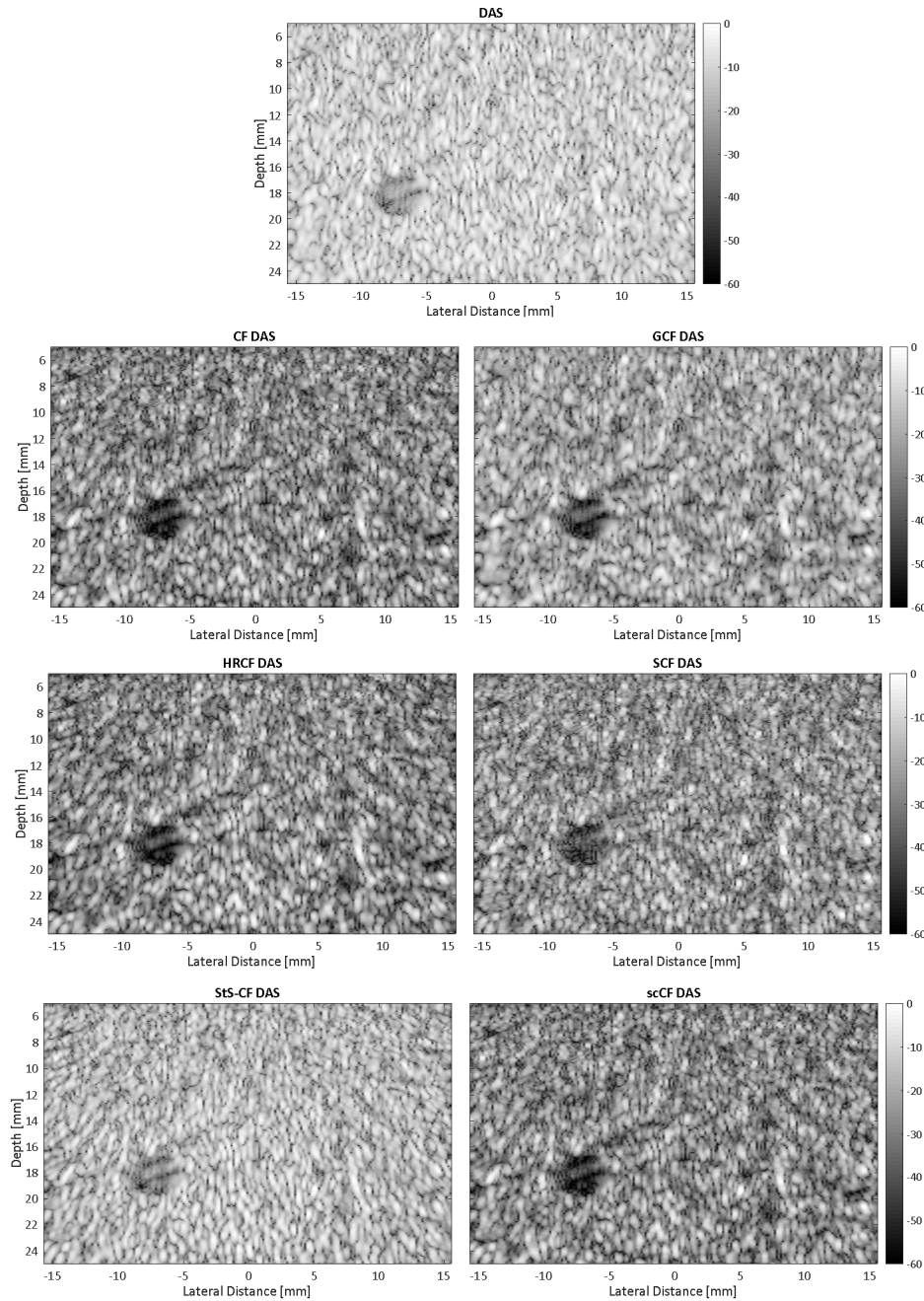


Figure 6.4: Ultrasound images of the cystic phantom shown in figure 6.3(a), using DAS beamformer, for different types of coherence-based methods. All images are displayed with a dynamic range of 60 dB.

6.4 Results and Discussion

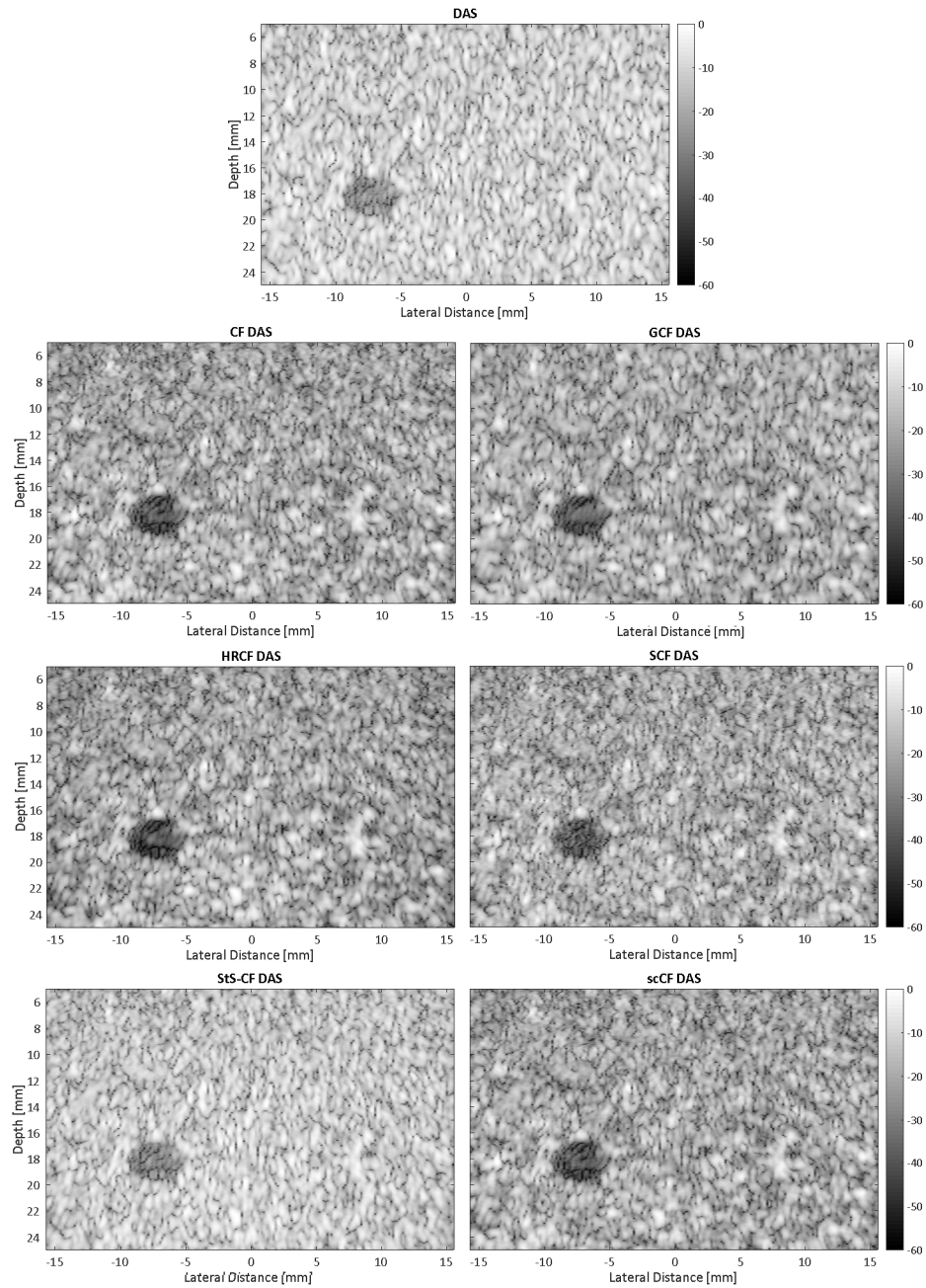


Figure 6.5: Ultrasound images of the cystic phantom shown in figure 6.3(a), using DAS beamformer and CPWI, for different types of coherence-based methods. All images are displayed with a dynamic range of 60 dB.

6.4 Results and Discussion

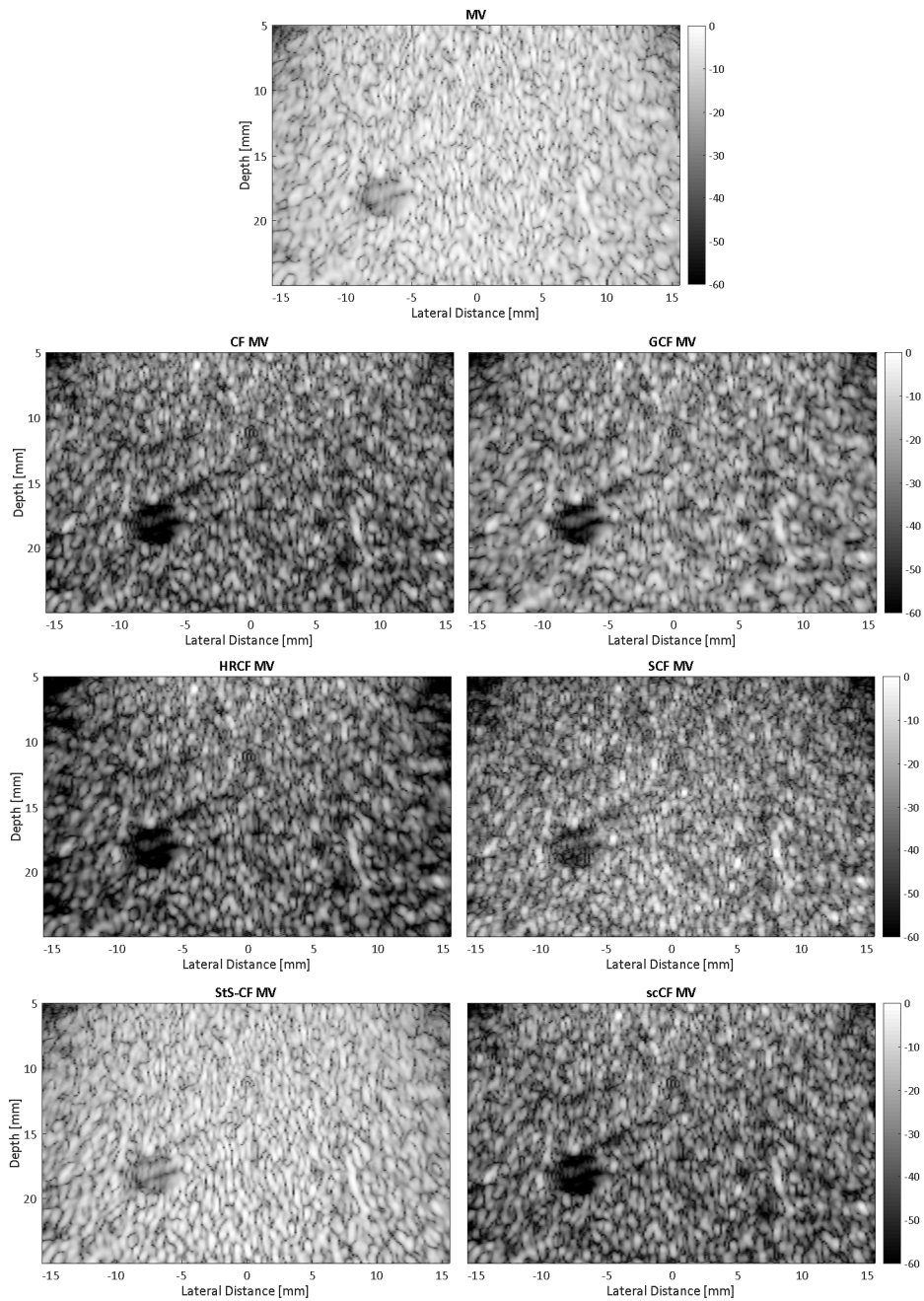


Figure 6.6: Ultrasound images of the cystic phantom shown in figure 6.3(a), using MV beamformer, for different types of coherence-based methods. All images are displayed with a dynamic range of 60 dB.

6.4 Results and Discussion

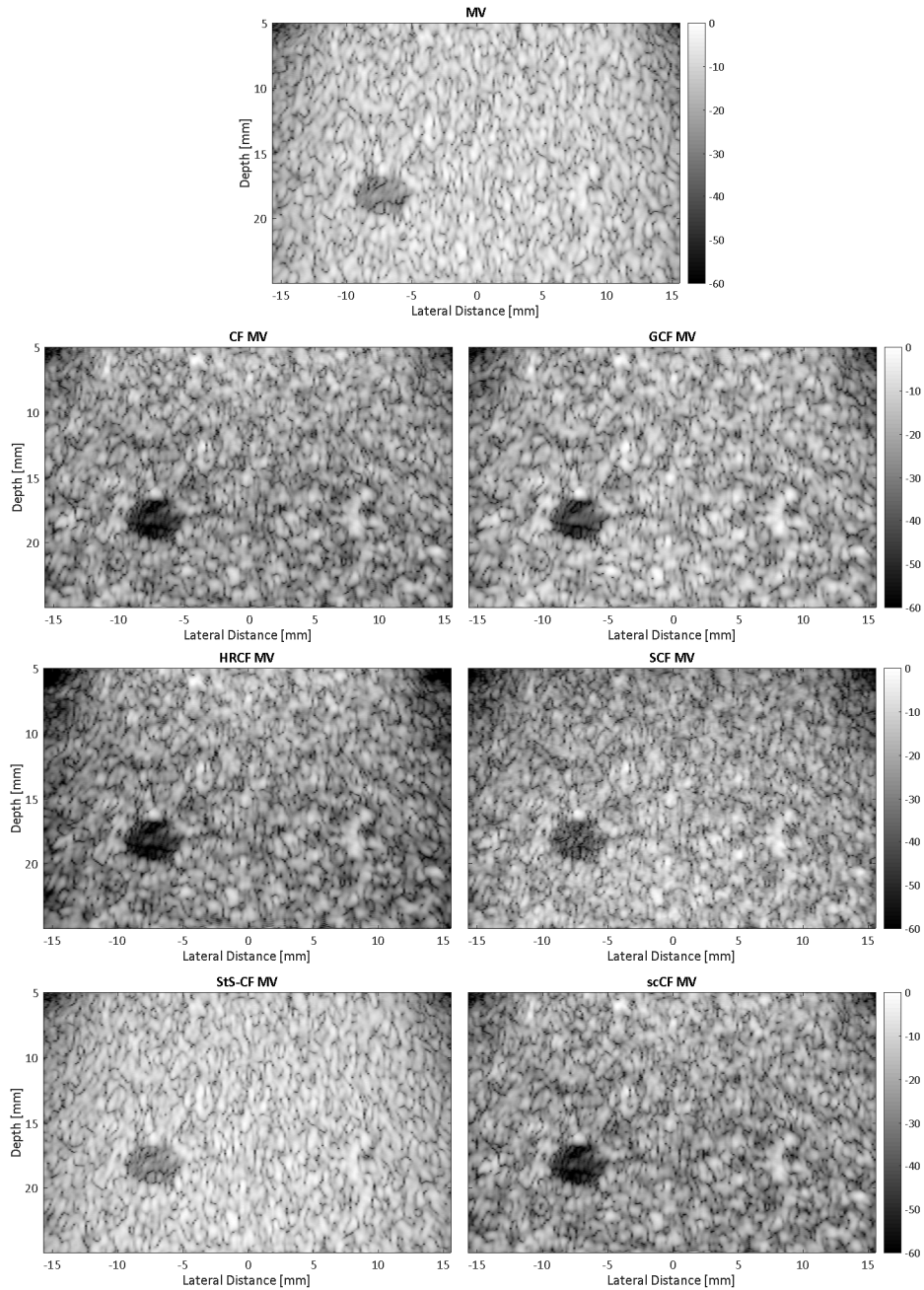


Figure 6.7: Ultrasound images of the cystic phantom shown in figure 6.3(a), using MV beamformer and CPWI, for different types of coherence-based methods. All images are displayed with a dynamic range of 60 dB.

6.4 Results and Discussion

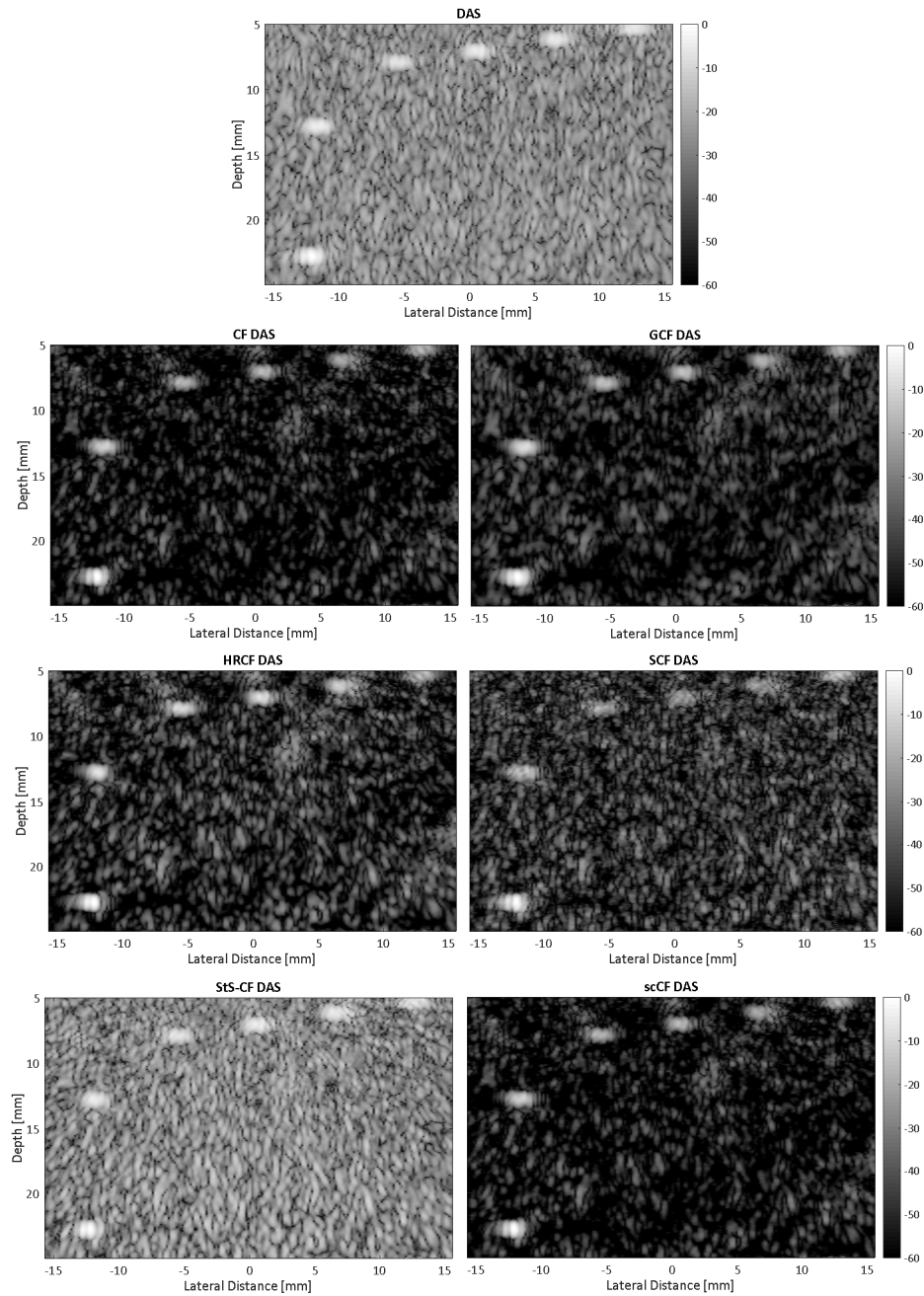


Figure 6.8: Ultrasound images of the wire-targets phantom shown in figure 6.3(b), using DAS beamformer, for different types of coherence-based methods. All images are displayed with a dynamic range of 60 dB.

6.4 Results and Discussion

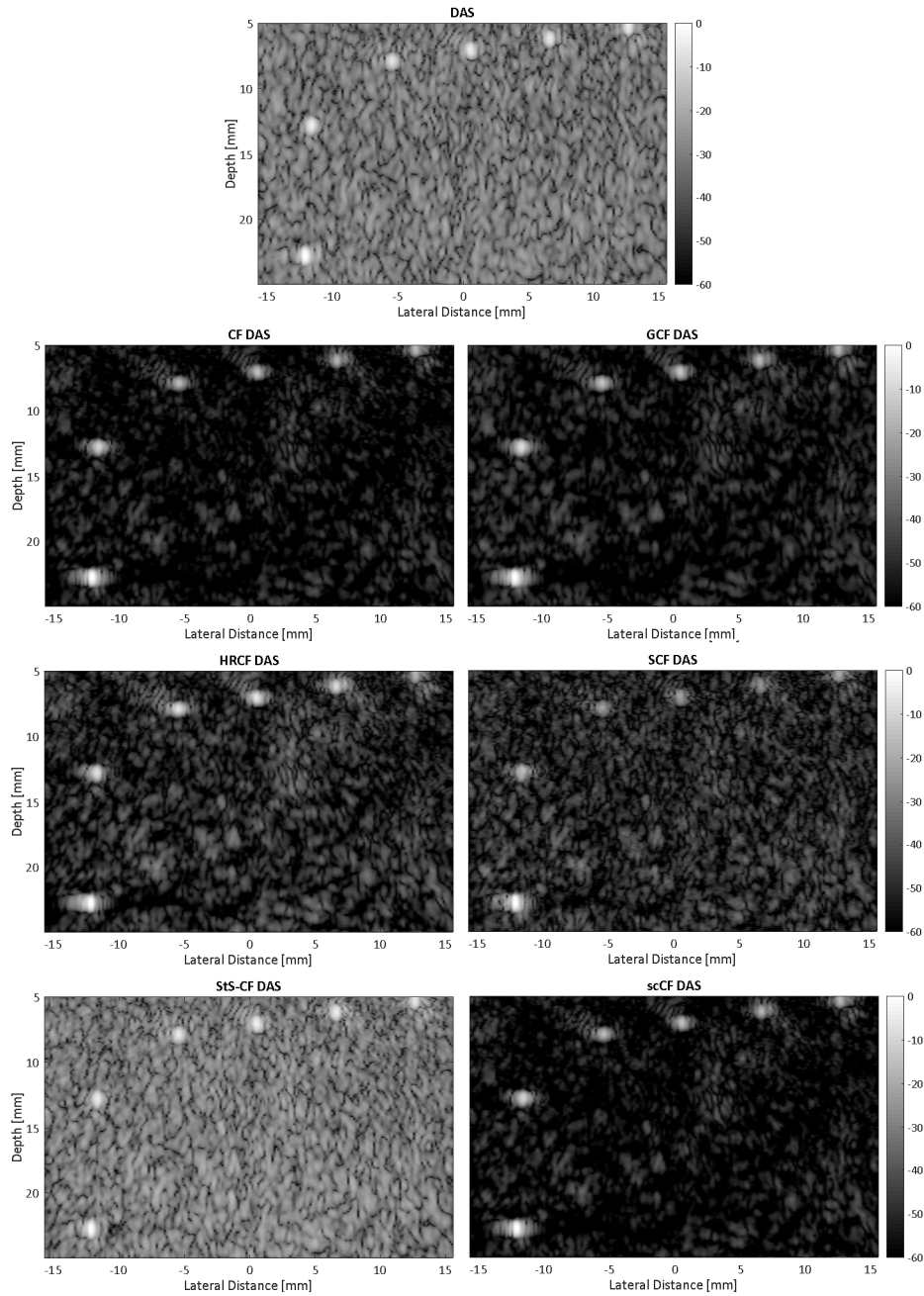


Figure 6.9: Ultrasound images of the wire-targets phantom shown in figure 6.3(b), using DAS beamformer and CPWI, for different types of coherence-based methods. All images are displayed with a dynamic range of 60 dB.

6.4 Results and Discussion

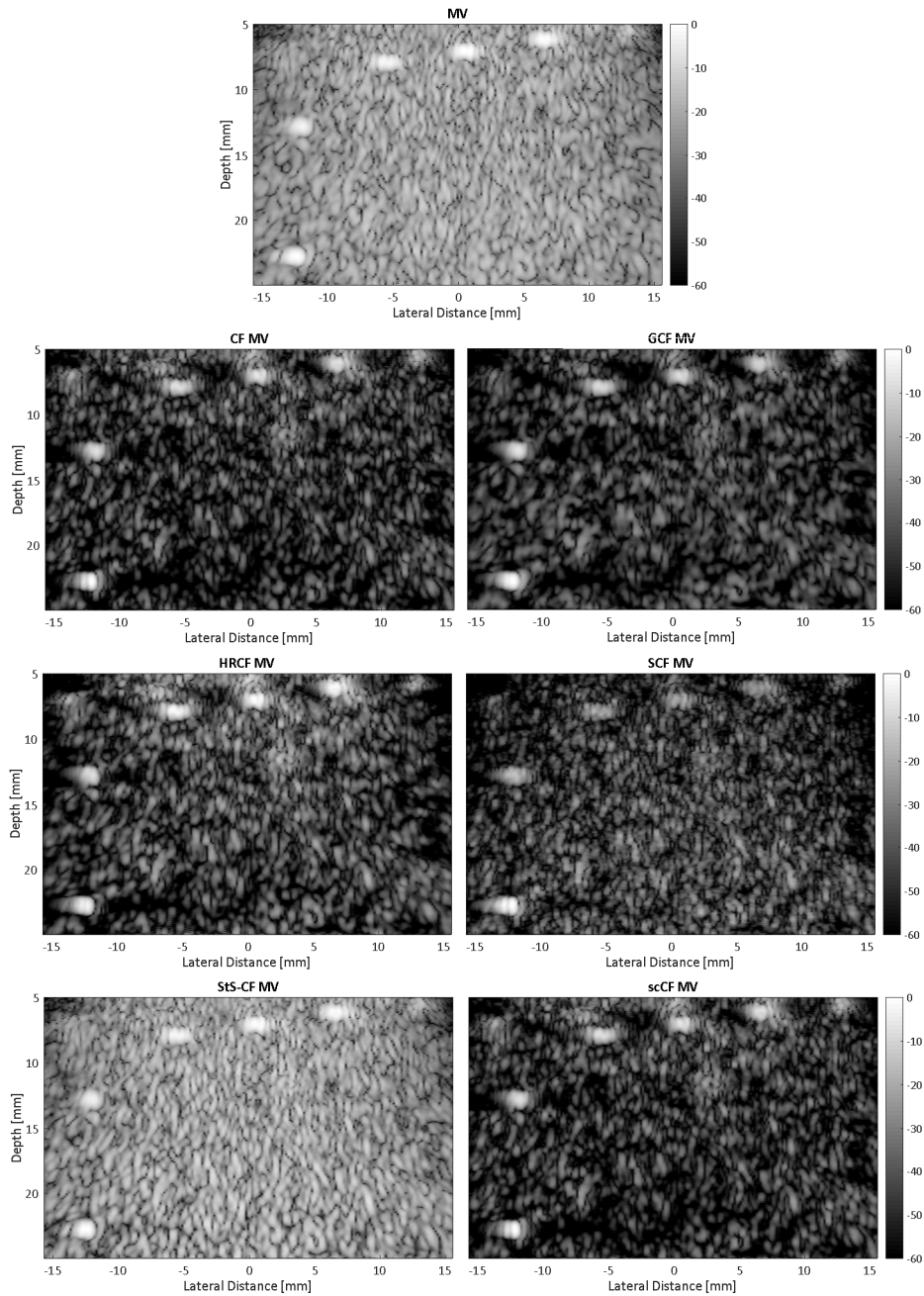


Figure 6.10: Ultrasound images of the wire-targets phantom shown in figure 6.3(b), using MV beamformer, for different types of coherence-based methods. All images are displayed with a dynamic range of 60 dB.

6.4 Results and Discussion

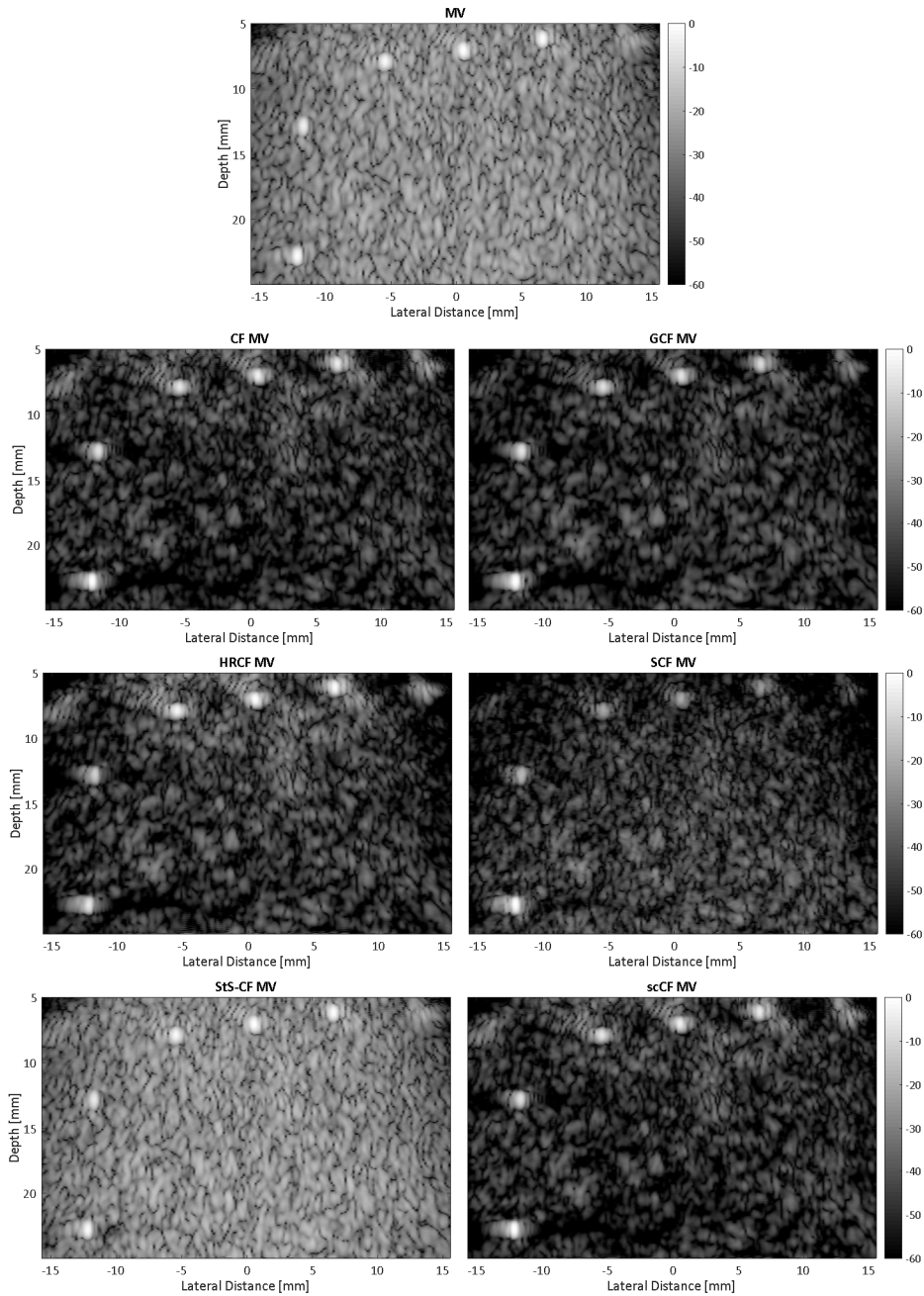


Figure 6.11: Ultrasound images of the wire-targets phantom shown in figure 6.3(b), using MV beamformer and CPWI, for different types of coherence-based methods. All images are displayed with a dynamic range of 60 dB.

Table 6.1: *CONTRAST AND SPECKLE STATISTICS MEASUREMENTS FOR THE CYST PHANTOM SHOWN IN FIGURE 6.3(a) FOR DIFFERENT COHERENCE-BASED FACTORS WHEN USED WITH DAS BEAMFORMER.*

PWI					
Method	μ_{Cyst} (dB)	μ_{Bg} (dB)	CR(dB)	CNR	SSNR _{Bg}
no CF	-22.92	-12.12	10.04	1.65	1.97
CF	-48.70	-35.31	22.58	2.58	0.94
GCF	-42.70	-27.24	22.20	2.50	1.16
HRCF	-46.76	-35.79	22.40	2.48	0.93
SCF	-41.70	-24.54	18.25	2.07	1.00
StS-CF	-28.93	-14.49	12.39	1.88	1.40
scCF	-48.70	-35.32	22.58	2.58	0.94
CPWI					
Method	μ_{Cyst} (dB)	μ_{Bg} (dB)	CR (dB)	CNR	SSNR _{Bg}
No CF	-26.76	-12.63	14.14	2.57	1.91
CF	-40.81	-21.16	19.65	2.91	1.30
GCF	-38.37	-21.89	16.47	2.42	1.30
HRCF	-42.11	-20.34	21.76	2.95	1.26
SCF	-39.30	-20.54	18.75	2.75	1.43
StS-CF	-29.18	-12.32	16.85	3.00	1.90
scCF	-40.81	-21.16	19.65	2.91	1.30

Table 6.2: *CONTRAST AND SPECKLE STATISTICS MEASUREMENTS FOR THE CYST PHANTOM SHOWN IN FIGURE 6.3(a) FOR DIFFERENT COHERENCE-BASED FACTORS WHEN USED WITH MV BEAMFORMER.*

PWI					
Method	μ_{Cyst} (dB)	μ_{Bg} (dB)	CR (dB)	CNR	SSNR _{Bg}
No CF	-22.17	-12.12	10.04	1.61	1.99
CF	-57.89	-35.31	22.58	2.57	0.92
GCF	-49.44	-27.24	22.20	2.69	1.14
HRCF	-58.19	-35.79	22.40	2.50	0.92
SCF	-42.79	-24.54	18.25	2.32	1.01
StS-CF	-26.87	-14.49	12.39	1.74	1.41
scCF	-57.89	-35.32	22.58	2.57	0.92
CPWI					
Method	μ_{Cyst} (dB)	μ_{Bg} (dB)	CR (dB)	CNR	SSNR _{Bg}
No CF	-27.62	-12.70	14.92	2.69	1.89
CF	-51.44	-26.83	24.61	3.35	1.25
GCF	-44.14	-20.24	24.18	3.38	1.25
HRCF	-51.81	-27.36	24.45	3.24	1.23
SCF	-40.33	-18.89	21.45	3.00	1.39
StS-CF	-29.10	-12.49	16.61	2.91	1.88
scCF	-51.44	-26.83	24.61	3.35	1.25

Table 6.3: *RESOLUTION AND BLACK-BOX REGION MEASUREMENTS FOR THE WIRE PHANTOM SHOWN IN FIGURE 6.3(b) FOR DIFFERENT COHERENCE-BASED FACTORS WHEN USED WITH DAS BEAMFORMER.*

PWI				
Method	FWHM (mm)	μ_{BBR} (dB)	σ_{BBR} (dB)	SSNR_{BBR}
No CF	1.38	-28.58	5.50	1.83
CF	0.51	-66.45	11.06	0.74
GCF	0.71	-64.20	8.93	0.92
HRCF	0.52	-64.04	12.15	0.75
SCF	0.43	-56.46	7.82	1.07
StS-CF	1.03	-33.07	9.07	1.09
scCF	0.51	-66.51	11.06	0.74
CPWI				
Method	FWHM (mm)	μ_{BBR} (dB)	σ_{BBR} (dB)	SSNR_{BBR}
No CF	0.56	-32.49	5.08	2.04
CF	0.46	-65.38	7.34	1.15
GCF	0.53	-65.25	6.98	1.19
HRCF	0.47	-59.96	8.06	1.06
SCF	0.43	-56.66	6.66	1.31
StS-CF	0.50	-32.65	6.11	1.66
scCF	0.46	-65.44	7.34	1.15

Table 6.4: *RESOLUTION AND BLACK-BOX REGION MEASUREMENTS FOR THE WIRE PHANTOM SHOWN IN FIGURE 6.3(b) FOR DIFFERENT COHERENCE-BASED FACTORS WHEN USED WITH MV BEAMFORMER.*

PWI				
Method	FWHM (mm)	μ_{BBR} (dB)	σ_{BBR} (dB)	SSNR_{BBR}
No CF	1.25	-25.09	5.35	1.89
CF	0.49	-65.82	12.04	0.73
GCF	0.88	-62.36	9.34	0.96
HRCF	0.96	-59.36	12.18	0.75
SCF	0.44	-53.42	8.09	0.98
StS-CF	1.07	-29.80	9.37	1.09
scCF	0.48	-65.90	12.04	0.73
CPWI				
Method	FWHM (mm)	μ_{BBR} (dB)	σ_{BBR} (dB)	SSNR_{BBR}
No CF	0.59	-27.09	5.19	2.03
CF	0.46	-62.10	8.18	1.02
GCF	0.53	-61.19	8.37	1.04
HRCF	0.50	-53.60	8.63	1.01
SCF	0.47	-52.15	7.08	1.22
StS-CF	0.54	-28.04	6.31	1.62
scCF	0.46	-62.18	8.19	1.02

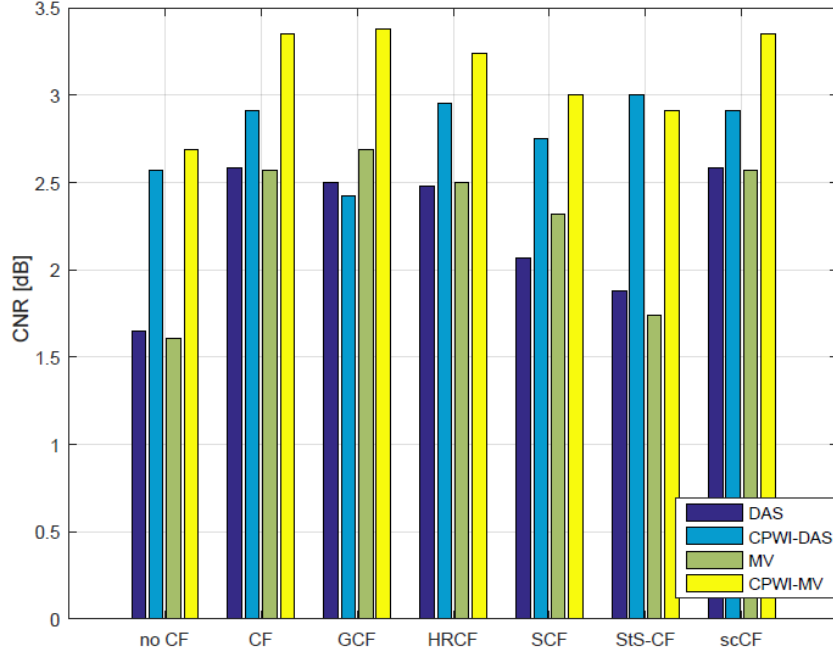


Figure 6.12: The value of CNR achieved from the implemented types of coherence-based factors when used with four different types of beamforming methods.

speckle is significantly reduced when using CF, where the $SSNR_{Bg}$ is dropped to the half. However, the high improvement in the cystic mean results in raising the overall CR and CNR as compared to DAS with no CF, as in table 6.1.

The BBR artefacts that appear when using CF can be noticed to the sides of each wire in the images of the wire-targets phantom shown in figure 6.8. A drop of nearly 40dB in the mean value of the BBR is shown, compared to the no CF case, with the standard deviation increased to the double, resulting in a drop in the SSNR in this region to less than the half. The main advantage of using CF is improving resolution, where the FWHM value is reduced by about 63%.

The amount of computational complexity of CF is directly proportional to the number of elements as shown in table 6.5. However, practically the CF is determined with one step regardless of the number of elements, by using the signals that already exist from DAS beamformer. This corresponds to a computational complexity of $O(1)$.

As compared to CF, GCF results in improved mean and SSNR of the background, due to its ability to deal with the incoherency of background speckle

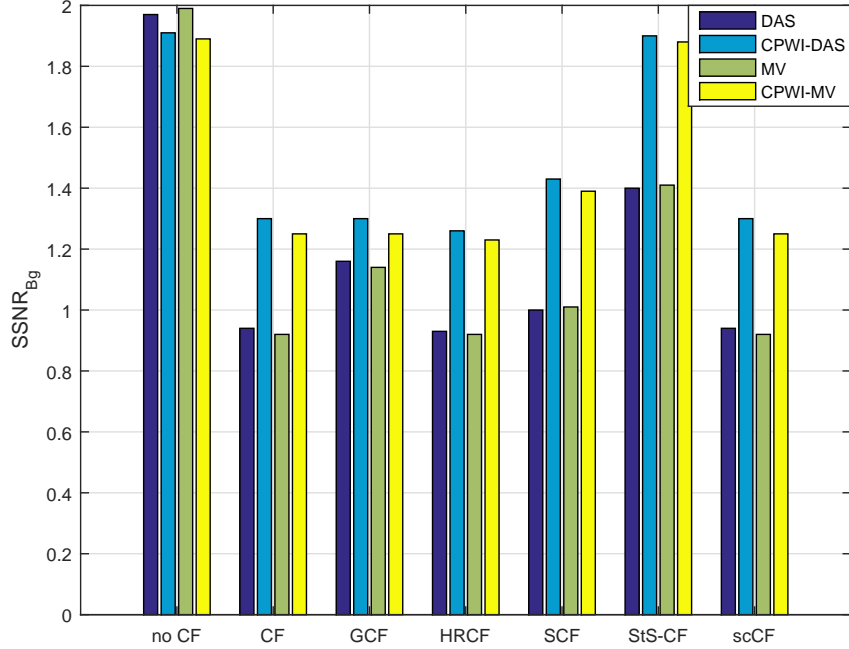


Figure 6.13: The value of $SSNR_{Bg}$ achieved from the implemented types of coherence-based factors when used with four different types of beamforming methods.

using the cutoff frequency M_0 . However, this comes at the cost of a reduction in the mean of the cystic area, which results in a slight reduction in CR and CNR. For the wire-targets phantom, the resolution also was slightly reduced, while the BBR problem is not solved by this type of coherence factor. Compared to CF, GCF has a high computational complexity of $O(N \log N)$, due to the use of FFT.

In HRCF, a subarray length of $N/4$ is used, with a temporal vector length of 25 samples. These settings were giving the best results for both DAS and MV beamformers, where higher subarray length reduces the robustness and thus the imaging quality is reduced, as explained in chapter 5. As shown in tables 6.1 and 6.3, HRCF with the used settings gives a similar imaging quality to that of the CF. However, the computational complexity is increased to $O(L_p^3)$, due to the need to MV beamformer output to calculate HRCF. When MV beamformer is used with HRCF instead of DAS, the computational complexity is reduced to $O(1)$, as the output of the MV is already calculated.

The highest resolution among the coherence-based types is achieved by SCF.

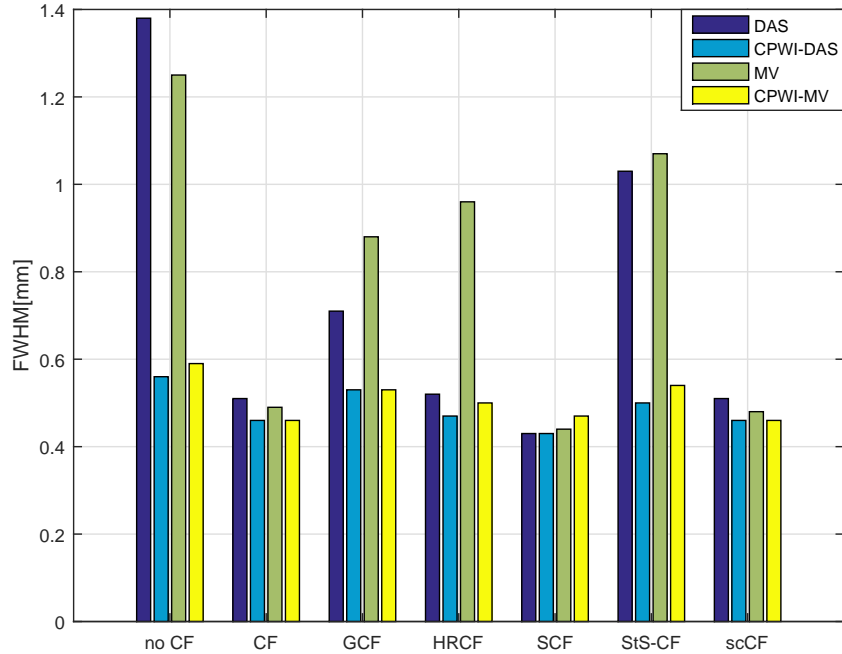


Figure 6.14: The FWHM achieved from the implemented types of coherence-based factors when used with four different types of beamforming methods.

It also reduces BBR artefacts significantly as can be noticed from figure 6.8. However, SCF underestimates the amplitudes of the wire targets, due to being embedded in a speckle background and the dependence only on the signs of the RF-signals rather than the amplitudes when calculating SCF. The improvement in the background mean is accompanied with an increase in the cystic mean, and this results in no increase in CNR, compared to CF. SCF has the same computational complexity as that of the CF, which is $O(N)$. As in CF, the use of this factor with DAS or MV beamformer reduces its computational complexity to $O(1)$.

The use of spatial and temporal smoothing in StS-CF is shown to be very effective in reducing BBR artefacts. However, this comes at the cost of reducing the total imaging quality, which becomes very near to the no CF case. This can be noticed from tables 6.1 and 6.3 and figures 6.4-6.11. Another disadvantage of StS-CF is that the computational complexity increases to $O((2K+1)PL_p)$. However, when it is used with MV beamformer with the same spatial and temporal lengths,

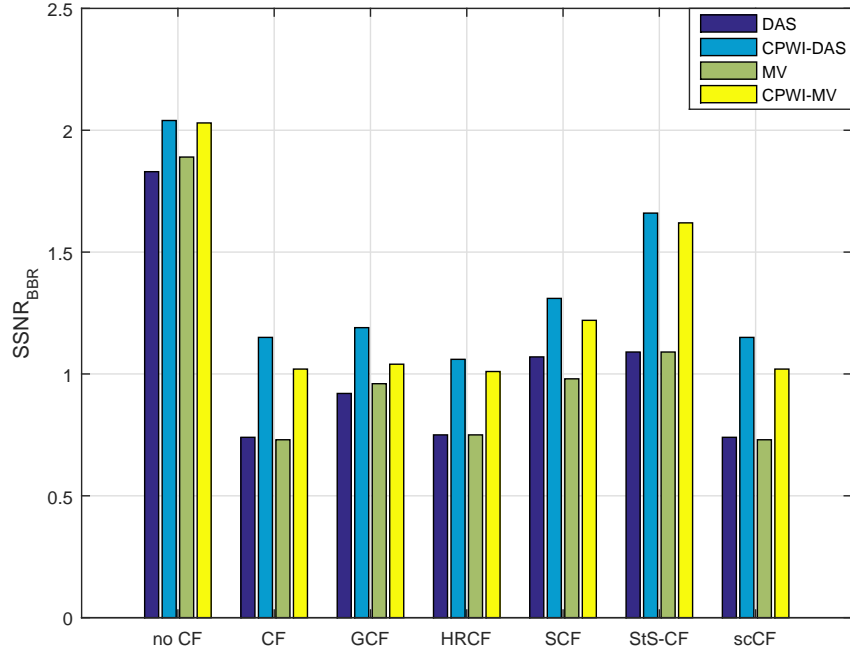


Figure 6.15: The value of $SSNR_{BBR}$ achieved from the implemented types of coherence-based factors when used with four different types of beamforming methods.

the computational complexity drops to $O(1)$.

The scCF is the other type that produced a similar imaging quality to the CF for the used two phantoms. This behaviour is expected at low SNR, since it is designed to turn into CF in this case as explained before. scCF has a similar computational complexity to GCF, which is $O(N \log N)$, since it requires the use of FFT during its calculations.

6.4.2 Using Coherence-Based Factors with MV Beamformer

The results of using the previously discussed factors were obtained using MV beamformer for comparison. It can be noticed from the results that the performances of DAS and MV beamformers are very similar when using the different types of coherence-based factors. This is because the performance of these factors usually dominate the overall performance of the beamformer. Another reason is that the MV beamformer has a similar performance to that of DAS when imaging

Table 6.5: *THE COMPUTATIONAL COMPLEXITY OF THE IMPLEMENTED COHERENCE-BASED FACTORS.*

Method	Computational Complexity
CF	$O(N)$
GCF	$O(N \log N)$
HRCF	$O(L_p^3)$
SCF	$O(N)$
StS-CF	$O((2K + 1) \cdot P \cdot L_p)$
scCF	$O(N \log N)$

lesions and speckle generating targets. This can be confirmed by comparing the images in figures 6.4, 6.6, 6.8 and 6.10 and from the measurements given in tables 6.1-6.4 and figures 6.12-6.15.

6.4.3 Using Coherence-Based Factors with CPWI

The performance of the coherence-based factors is also studied when using CPWI, with both DAS and MV beamformers. The results of the cystic phantom imaging given in figures 6.5 and 6.7 show that in general, the compounding operation improves the cystic mean value in both DAS and MV beamformers, with a slight improvement in the background speckle. This leads to higher CNR and almost the same $SSNR_{Bg}$, as given in tables 6.1 and 6.2. In the presence of coherence-based factors according to these tables, CPWI decreased the effect of these factors in improving the cystic mean value, but achieved higher background mean value which improved both CNR and $SSNR_{Bg}$, compared to DAS and MV with no CPWI. This can be clearly noticed from figures 6.12 and 6.13.

From the results of the wire-targets phantom given in figures 6.9 and 6.11, tables 6.3 and 6.4 and figure 6.14, it can be noticed that the resolution is slightly improved when using CPWI (except for SCF resolution that was not affected by the compounding). The BBR artefacts are reduced by CPWI, but not completely removed. Both the mean and standard deviation of this region are improved by CPWI, which leads to boosting the value of $SSNR_{BBR}$ as can be noticed from

figure 6.15.

6.5 Conclusions

In ultrasound imaging, the efficiency of a beamformer is measured from its ability to eliminate the clutter caused by echo signals coming away from the focal point (off-axis signals), that are real but unwanted signals. CF distinguishes off-axis signals and reduces the beamformer weight depending on the amount of incoherency of these signals. This has a drawback of distorting the background speckle which is highly incoherent.

The two main features that define the quality of medical images are contrast and resolution. In computed tomography and magnetic resonance imaging, high quality images in terms of contrast and resolution are produced. In ultrasound imaging, in addition to being cheap, non-invasive and portable type of imaging, high quality images are obtained, due to the recent developments in ultrasound instruments and beamforming techniques.

In conventional DAS beamformer, poor contrast and resolution are usually achieved, due to the high level of sidelobes. A resolution increase with 10% is achieved using MV beamformer. More improvement in resolution could be attained by increasing the subarray length that was used, but this will be at the cost of degrading the imaging quality due to the reduced robustness. Therefore, a subarray length of $N/4$ for the MV beamformer was used in this chapter to provide a trade-off between resolution and robustness. A resolution increase of 60% in DAS and 53% in MV is achieved when CPWI is used. The use of coherence-based factors helped to add more improvement to resolution. This amount of improvement was nearly similar for all of these types, except when using StS-CF, where a similar resolution to the case of no CF was achieved in both DAS and MV. This is due to the temporal and spatial smoothing operations used in this type of CF to eliminate BBR artefacts.

The contrast achieved with MV is comparable to that in DAS, and the amount of improvement added to contrast when using CPWI in DAS and MV is also comparable. When coherence-based factors are used, the CNR is enhanced, as can be seen from tables 6.1 and 6.2, due to the significant improvement added

to the cystic mean value, except when using StS-CF where a very near CNR to that in the no CF case is achieved.

The BBR artefacts appear in all the implemented coherence-based types and are only reduced in the StS-CF, at the expense of degraded imaging quality in terms of resolution and contrast. However, this degradation in the quality is reduced when CPWI is applied.

Due to the close imaging quality of adaptive and non-adaptive beamformers when coherence-based factors are used, DAS beamformer is recommended to be used due to having lower computational complexity of $O(N)$ that enables real time imaging, compared to a $O(L_p^3)$ complexity in MV.

In addition to resolution improvement, the use of CPWI leads to boosting the imaging quality in terms of contrast and background speckle homogeneity. Furthermore, CPWI reduces the effect of BBR artefacts significantly, which comes at the cost of increased amount of computations and reduced frame rate.

Chapter 7

Partial Eigenspace-Based Minimum Variance for Medical Ultrasound Imaging

This chapter is based on a paper submitted for publication entitled: *(Partial Eigenspace-Based Minimum Variance (PESBMV) Beamforming for Medical Ultrasound Imaging)*.

A beamformer for medical ultrasound imaging must satisfy the performance requirements for three cases; hyperechoic objects, cystic and hypoechoic objects and speckle generating backgrounds. There is no beamformer that can maximize the spatial resolution and contrast simultaneously while preserving the speckle pattern for all these cases. In PWI, Eigenspace-Based Minimum Variance (ESBMV) is one of the methods used for improving contrast as well as resolution of MV adaptive beamformers. However, two types of artefacts that limit the performance in this method exist. They are the BBR and dark-spot artefacts.

A composite method, Partial-ESBMV, to utilize the strengths of existing beamforming methods of ESBMV and MV is proposed in this chapter to remove the artefacts of BBR introduced by ESBMV. In reference ESBMV, the MV weighting vector is projected into the signal subspace matrix that is found from the Eigendecomposition of MV covariance matrix into signal subspace and noise

subspace. The proposed method depends on the number of eigenvectors included in the signal subspace matrix to make the decision of including or eliminating the MV weighting projection using the signal subspace matrix.

The feasibility of using the proposed method of PESBMV in medical imaging to remove BBR artefacts introduced by reference ESBMV is investigated in this chapter, with a study of the impact of this method on computational complexity, resolution, contrast and speckle pattern. This is achieved by using experimental RF-data of two different types of phantoms that include a cyst, hyperechoic lesion and wire targets embedded in speckle generating background. In-vivo images of human carotid are also used in this chapter, in order to examine the efficiency of the proposed method in clinical ultrasound imaging.

7.1 Introduction

Plane wave images can be produced using adaptive or non-adaptive beamformers. Unlike non-adaptive beamformers that use predefined weighting vectors, adaptive beamformers recalculate the weighting vector at each imaging point depending on the received data, which results in high imaging resolution and low sidelobe levels. However, both beamformers suffer from poor contrast, due to the lack of focusing in PWI. In order to overcome this limitation, a number of techniques that can be added during the beamforming have been suggested in the literature.

One of these techniques is the ESBMV. It is used to improve performance in MV beamformer, by projecting the MV weighting vector onto the signal subspace produced from the eigendecomposition of the MV covariance matrix into signal subspace and noise subspace. Since it was first introduced by [Van Veen \(1988\)](#), the ESBMV adaptive beamformer was used in various ultrasound imaging applications ([Lee & Lee, 1997](#); [Mehdizadeh *et al.*, 2012a](#); [Sekihara *et al.*, 2002](#)), and was successfully combined with other techniques like subarray coherence-based postfiltering ([Zhao *et al.*, 2016](#)) and Wiener postfiltering ([Zeng *et al.*, 2012](#)), for higher imaging quality.

ESBMV is of high efficiency in reducing sidelobe levels, which can be noticed clearly when imaging a wire phantom in water, or during the simulations of a PSF. This is due to the high sidelobe interference of the hyperechoic object that

reduces SNR and result in decreasing the ESBMV output weight significantly. However, when imaging a strong scattering object embedded in a speckle generating background, the interference of the sidelobes of this object reduces the ESBMV weight, producing black areas to the sides of this hyperechoic object. These artefacts are called Black-Box Region (BBR) and they are similar to the CF BBR artefacts mentioned in chapter 6.

The main property exploited by ESBMV for removing off-axis and sidelobe energy from signals is the orthogonality between signal and noise subspaces in the MV covariance matrix. However, overestimating the size of the signal subspace leads to lowering the noise reduction from the image and approaching the quality of a reference MV beamformer. On the other hand, underestimating the size of the signal subspace results in distorting the signal and produces dark-spot artefacts in the speckle background.

Recently, several research groups have been investigating and developing different schemes for improving ESBMV beamforming. [Asl & Mahloojifar \(2010\)](#) suggested the use of iterative ESBMV to specify suitable values for the imaging parameters that optimize the imaging quality, using a simulated cyst phantom. However, the effect of the changed parameters on BBR artefacts was not considered for the suggested iterative method, which was inefficient and time consuming. [Zeng *et al.* \(2012\)](#) proposed to combine ESBMV with Wiener postfiltering to improve both the contrast and resolution of ESBMV. However, this proposed combination failed to reduce the dark spots and BBR artefacts in the background speckle. [Aliabadi *et al.* \(2015\)](#) proposed a method that improves contrast in ESBMV by utilizing the properties of the echo signals received by the surrounding points to amend the focal point value. This method was able to reduce dark-spot artefacts, but was not strong enough to remove BBR artefacts. [Zhao *et al.* \(2016\)](#) proposed a new method that combines ESBMV with Subarray-based coherence factor. This method helps improving the imaging quality in terms of contrast, resolution and speckle homogeneity. On the other hand, the computational efficiency is reduced due to the use of subarray smoothing, and BBR artefacts are not reduced. The compensated subspace scheme used to reduce BBR artefacts by reducing the size of signal subspace when BBR artefacts appear is iterative, inefficient and infeasible for medical ultrasound imaging.

7.2 Eigenspace-Based Minimum Variance (ESBMV)

In this chapter, a new method of Partial-ESBMV (PESBMV) is proposed to completely eliminate BBR artefacts in reference ESBMV. This is done by cancelling the projection of the MV weighting in the BBR area, which is detected from the size of the signal subspace calculated by ESBMV. In this way, the speckle pattern is evaluated using reference MV which has no BBR artefacts, and thus these artefacts are totally removed without the need to increase the computational complexity of the method and without any reduction in the imaging quality. The feasibility of the proposed method is demonstrated experimentally using UARP II imaging system (Cowell *et al.*, 2013; Smith *et al.*, 2012, 2013), and Multi-Purpose Multi-Tissue Ultrasound Phantom (Model 040GSE, CIRS Inc., Norfolk, VA, USA) that provides different types of lesions embedded in a scattering background, where speckles are generated physically by the background material of the used phantom.

In order to further improve the imaging quality, the use of CPWI with PESBMV is also proposed. This is because of the improvement that CPWI can add to the resolution and speckle homogeneity of the produced images, without affecting the BBR artefacts reduction of PESBMV and contrast improvement of ESBMV. The results show a complete removal of BBR artefacts, 50% improvement in resolution and a high contrast of up to 104%, as compared to reference MV. In addition, in vivo results of a human carotid RF-data are used to show the efficiency of the proposed method in medical imaging.

7.2 Eigenspace-Based Minimum Variance (ESBMV)

The method of ESBMV is widely used in medical ultrasound imaging, due to its ability to provide MV with high contrast and low sidelobe levels with preserving or even improving resolution. In this technique, the MV covariance matrix is decomposed into signal subspace and noise subspace depending on the Eigen structure of this matrix. Afterwards, the weighting vector of MV is projected to the constructed signal subspace.

7.2 Eigenspace-Based Minimum Variance (ESBMV)

Using Eigendecomposition, the covariance matrix R can be written as (Mehdizadeh *et al.*, 2012a; Zeng *et al.*, 2012):

$$R = \mathbb{V} \mathbb{\Lambda} \mathbb{V}^H, \quad (7.1)$$

where $\mathbb{\Lambda} = \text{diag}[\lambda_1 \geq \lambda_2 \geq \dots \geq \lambda_{L_p}]$ is the diagonal matrix whose diagonal is the eigenvalues denoted by λ_i given in the parenthesis. These eigenvalues are sorted in descending order so that λ_1 represents the maximum eigenvalue. \mathbb{V} consists of the eigenvectors of R , $[v_1, v_2, \dots, v_{L_p}]$, sorted according to their corresponding eigenvalues.

After eigendecomposition and then sorting eigenvalues and their eigenvectors correspondingly, signal subspace matrix (E_s) is constructed using the highest (N_{sig}) eigenvectors of the covariance matrix. In other words, E_s is an L_p by N_{sig} matrix of eigenvectors which can be written as (Asl & Mahloojifar, 2010):

$$E_s = [v_1, v_2, \dots, v_{N_{sig}}], \quad (7.2)$$

where N_{sig} is the number of eigenvectors that can effectively represent the signal subspace.

This is based on the fact that the MV covariance matrix is constructed from two orthogonal subspaces, the first one is the signal subspace E_s that contains the eigenvectors associated with the first highest eigenvalues and it contains mainlobe energy, while the second is the noise subspace E_n which is represented by the rest of the eigenvectors and includes sidelobes and off axis energy (Lee & Lee, 1997).

The number of eigenvectors included in E_s , or N_{sig} , is specified depending on a threshold value called λ_{th} . This threshold is equal to δ times the maximum eigenvalue (Asl & Mahloojifar, 2010; Mehdizadeh *et al.*, 2012a; Zeng *et al.*, 2012), *i.e.*:

$$\lambda_{th} = \lambda_1 \cdot \delta, \quad (7.3)$$

where δ is a constant value that ranges between 0 and 1 and is prespecified by the user before starting the beamforming.

The signal and noise subspace matrices are specified depending on λ_{th} , by including all the eigenvectors that correspond to the eigenvalues that are greater than or equal to λ_{th} in E_s , while the rest eigenvectors are included in E_n . The

The mainlobe energy included in E_s is used to produce a new weighting vector from reference MV weight, using the following equation (Asl & Mahloojifar, 2010; Mehdizadeh *et al.*, 2012a; Zeng *et al.*, 2012):

$$W_{ESBMV} = E_s E_s^H w. \quad (7.4)$$

As the imaging resolution is mainly determined from the mainlobe width, MV resolution is preserved when using ESBMV and for high values of δ , resolution is even improved.

7.3 Proposed Method

The proposed method of PESBMV essentially depends on the value of N_{sig} to enable or disable applying ESBMV. Therefore, it is important to understand the behaviour of this value with the different imaging objects. This is explained by applying ESBMV with δ of 0.2 to the two phantoms shown in the left column of figure 7.2, and displaying the value of N_{sig} in the right column of this figure. The first phantom includes a 3mm diameter cyst centred at the 18mm depth, while the second contains 5 wire targets and an 8mm diameter hyperechoic lesion centred at the 36mm depth. The cyst, hyperechoic lesion and wires are all embedded in a speckle background.

It can be noticed from this figure that the value of N_{sig} becomes very small for the imaging points located in the BBR and strong scattering regions, while in the speckle background and cystic objects, N_{sig} is of about half the subarray length or higher, where a subarray length of 32 elements is used. Based on that, the proposed method of PESBMV uses a threshold of $(L_p \cdot \eta)$ for N_{sig} to decide whether the effect of ESBMV is allowed or blocked, where η is a coefficient specified by the user and it ranges between 0 and 1.

According to this method, equation 7.4 of ESBMV weighting vector will be rewritten as follows:

$$W_{PESBMV} = \begin{cases} E_s E_s^H w & \text{if } N_{sig} > L_p \cdot \eta \\ w & \text{otherwise.} \end{cases} \quad (7.5)$$

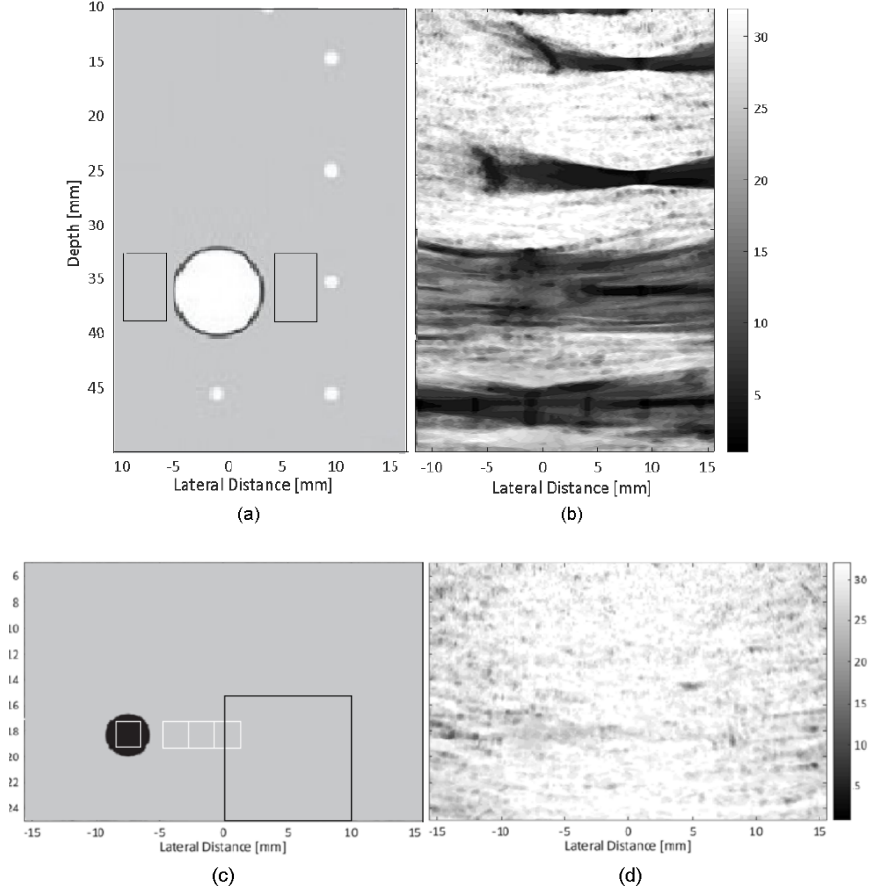


Figure 7.2: The value of N_{sig} , or the number of eigenvectors included in the signal subspace matrix E_s , using reference ESBMV at $\delta=0.2$. (a) and (c) show the two phantoms for which, N_{sig} is displayed in (b) and (d) using a subarray length of 32. Therefore, the colour bars that indicate the values of N_{sig} to the left of the figure are between 1 and 32. (a) is a wire phantom with 5 wires and an 8mm diameter lesion centred at the 36mm depth. The two 6x4mm black squares to the sides of the lesion indicate the area for which, BBR artefacts are assessed using $SSNR_{BBR}$. (c) is a cyst phantom with a 3mm diameter cyst centred at the 18mm depth. The three 2x2 white squares to the left of the cyst are the background areas for which, CR and CNR are measured, while the 10x10mm black square is used to assess the homogeneity of the background speckle using $SSNR_{Bg}$.

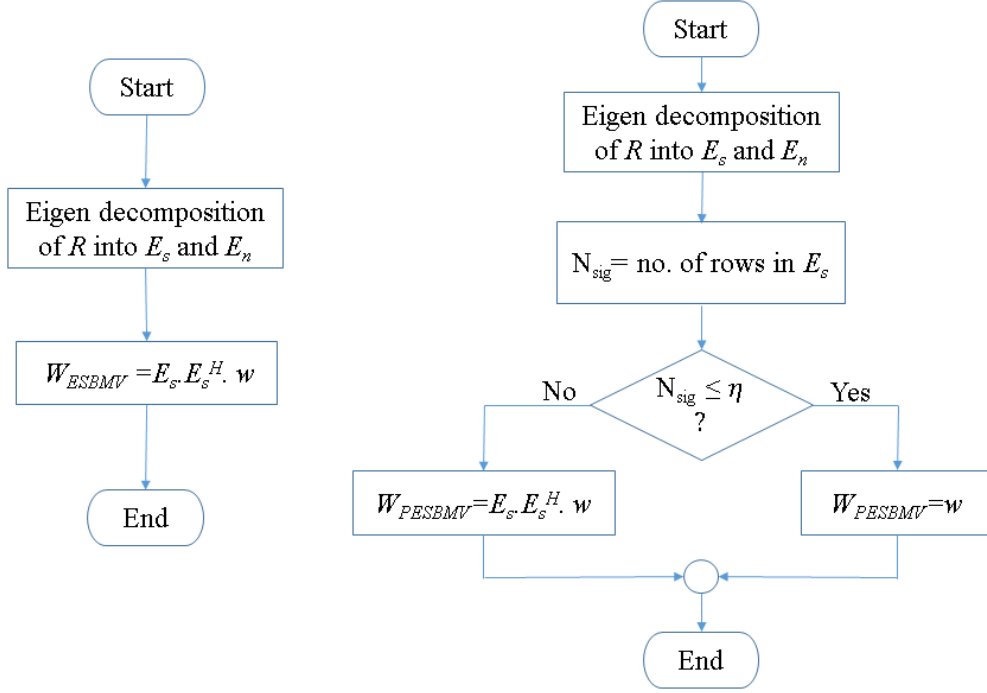


Figure 7.3: Flow charts that explain the steps followed during the beamforming operation after calculating the MV weighting vector and covariance matrix using: (a) ESBMV and (b) PESBMV.

By setting η to 1, only MV beamforming is applied without any Eigenspace-based processing. Setting η to 0, on the other hand, converts the beamformer to reference ESBMV, where equation 7.4 will be applied to all the imaging points. Figure 7.3 shows a flow chart for the proposed method as compared to the reference method of ESBMV.

It is important to mention that the proposed method cannot be used blindly with ESBMV at any value of δ . This is because increasing δ is usually accompanied with a decrease in the value of N_{sig} . In this case, the condition of $N_{sig} > L_p \cdot \eta$ in equation 7.5 will be false more frequently, forcing the behaviour of PESBMV to get closer to MV beamformer. Therefore, whenever δ had to be increased (for example with highly noisy signals), the value of η will have to be decreased ac-

cordingly. Therefore in this work, the proposed method is tested using two values of δ : 0.2 and 0.4, with η being 0.65 and 0.35, respectively.

7.4 Experimental Setup

The performance of the proposed method of PESBMV is evaluated using 2 sets of experimental data that include cystic lesion, hyperechoic lesion and wire targets embedded in speckle generating backgrounds with 0.5 dB/cm.MHz attenuation coefficient. These sets of RF-data were captured for the 040GSE Multi-Purpose Ultrasound phantom, using UARP II ultrasound imaging device.

L3-8/40EP linear array transducer with 128 elements and one wavelength inter-element distance of 0.3048mm was used during experiments, with 5MHz central frequency, 100% bandwidth and 80MHz sampling rate. A 2-cycles Gaussian pulse at the central frequency was used as the excitation signal. In MV beamforming, 25 samples were used for temporal smoothing ($K=12$), while for spatial smoothing, the subarray length was fixed to $N/4$ which equals to 32 transducer element.

PESBMV beamforming method is evaluated using the experimental data of the cyst and wire phantoms shown in figure 7.2(a,c) using two different settings. The first is at $\delta=0.2$ and $\eta=0.65$, and the second is at $\delta=0.4$ and $\eta=0.35$. The performance is evaluated and compared with those of the DAS (with Hanning apodization), MV, CF-MV and ESBMV at two values of δ : 0.2 and 0.4, using the quality metrics explained in section 7.5. This comparison is given in two cases, when using PWI and CPWI, as will be explained in section 7.6.

In CPWI, increasing the step between the compounded angles improves both resolution and artefacts reduction (including dark spots). This improvement increases with the number of compounded angles up to a specific number, where afterwards the improvement becomes negligible. According to the work presented in chapter 4 and from the maximum imaging depth, medium attenuation and transducer sensitivity, the angular range within which the steering angles are selected is $\pm 15^\circ$. At the chosen step of 5° , 7 angles within the $\pm 15^\circ$ can be compounded. However, because the results of compounding 7 and 5 angles were

seen to be very close, only 5 angles are compounded so that less computational time is required.

7.5 Quality Metrics

The imaging quality of the proposed method is assessed using various metrics, in order to show its efficiency in reducing BBR artefacts and preserving contrast and resolution.

Contrast is assessed for the cyst phantom using Contrast Ratio (CR) and Contrast-to-Noise Ratio (CNR). CR is the absolute difference between the mean values of the cystic area and the background tissue as in the following equation (Seo, 2008):

$$CR = |\mu_{Bg} - \mu_{Cyst}|, \quad (7.6)$$

where μ_{Cyst} is the mean value of the 2x2mm white square shown in figure 7.2(c) inside the cyst and μ_{Bg} is the average mean of the background speckle areas shown in the same figure by the three 2x2mm white squares at the same depth of the cyst. CNR is the ratio between CR and the standard deviation of the background speckle (Seo, 2008):

$$CNR = \frac{CR}{\sigma_{Bg}} = \frac{|\mu_{Bg} - \mu_{Cyst}|}{\sigma_{Bg}}, \quad (7.7)$$

where σ_{Bg} is the standard deviation of the background area shown by the three 2x2mm white squares in figure 7.2(c). For accurate contrast measurement, CR and CNR are calculated by averaging the CRs and CNRs at these three square areas. Both CR and CNR are measured for the decibel converted signal, where a dynamic range of 50dB is used.

Lateral Resolution is evaluated using Full Width at Half Maximum (FWHM), or the beam width at the -6dB intensity drop (Harput *et al.*, 2014). This is evaluated for the wire target located at the 25.3mm depth in the wire phantom shown in figure 7.2(a). In axial direction, resolution is only affected by the transmitted bandwidth, and therefore is not included in the calculations, due to the use of a fixed transmitted bandwidth during this work.

Speckle quality is evaluated using the mean, standard deviation and Speckle-Signal-to-Noise-Ratio ($SSNR_{Bg}$) for the speckle area shown in figure 7.2(c) by the 10x10mm black square between the 15 and 25mm depths. $SSNR_{Bg}$ is calculated using the following formula (Lediju *et al.*, 2011; Xu *et al.*, 2014):

$$SSNR_{Bg} = \frac{\mu_{Bg}}{\sigma_{Bg}}, \quad (7.8)$$

where μ_{Bg} and σ_{Bg} are measured for the amplitude detected signal of the background before converting to decibel.

For assessing the efficiency in reducing BBR artefacts, a similar formula to that given in equation (7.8) is used to measure the Speckle-Signal-to-Noise-Ratio of the BBR ($SSNR_{BBR}$) as follows:

$$SSNR_{BBR} = \frac{\mu_{BBR}}{\sigma_{BBR}}, \quad (7.9)$$

where μ_{BBR} and σ_{BBR} are the mean and standard deviation values of the BBR, respectively, measured for the BBR area indicated by the two 6x4mm black squares shown in figure 7.2(a) to the sides of the lesion.

7.6 Results

7.6.1 Plane-Wave Imaging (PWI)

The results of beamforming a single unfocused plane-wave signal captured for the wires and cyst phantoms are shown in figures 7.4 and 7.5, respectively, while the performance evaluation metrics measured for these two figures are given in tables 7.1 and 7.2, respectively.

Table 7.1 shows that DAS and MV beamformers have close FWHM values. This is due to the low robustness of MV which degrades its performance in noisy signals. The highest resolution of 0.54mm was achieved from CF-MV, which is nearly half the resolution of the other beamforming methods. As expected for the proposed method, resolution is shown to be equal to that of MV at both the two values of δ .

The dark spots and BBR artefacts accompanied with ESBMV can clearly be seen in figure 7.4(d) at $\delta=0.2$. These artefacts increase when δ is changed to 0.4,

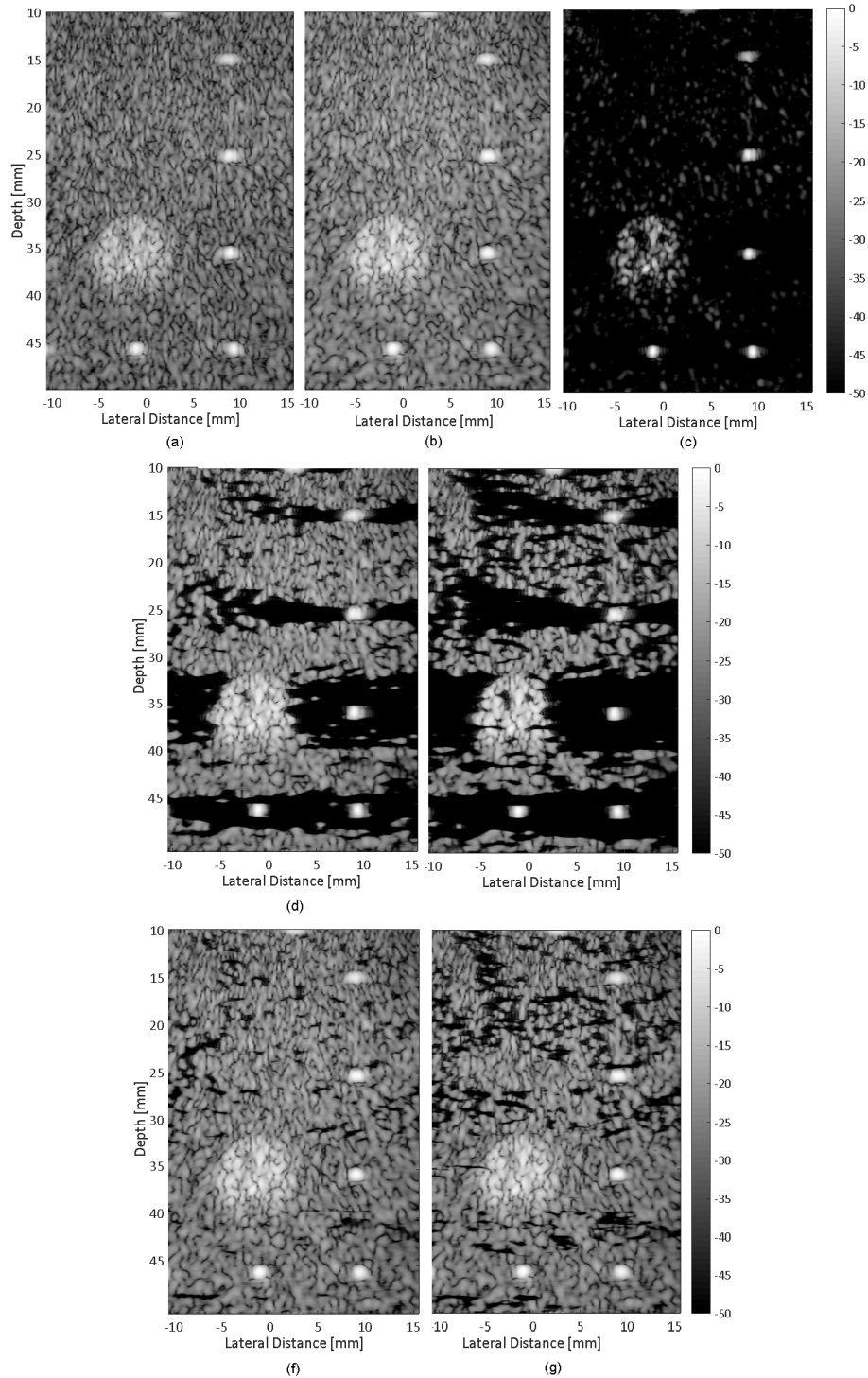


Figure 7.4: Ultrasound images of the experimental RF-data of the wire phantom shown in figure 7.2(a) using: (a) DAS (b) MV (c) CF-MV (d) ESBMV ($\delta = 0.2$) (e) ESBMV ($\delta = 0.4$) (f) PESBMV ($\delta = 0.2$, $\eta = 0.65$) (g) PESBMV ($\delta = 0.4$, $\eta = 0.35$). All images are displayed with a dynamic range of 50dB.

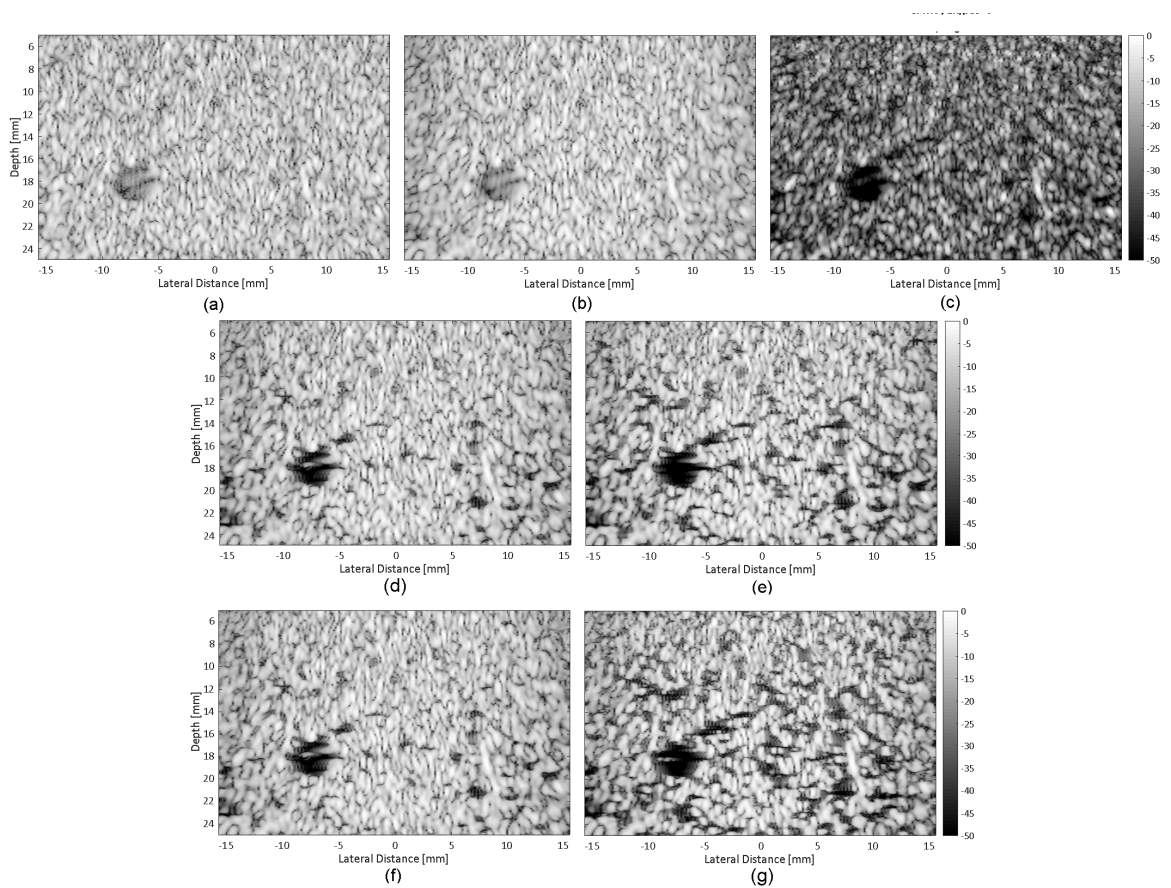


Figure 7.5: Ultrasound images of the experimental RF-data of cyst phantom shown in figure 7.2(c) using: (a) DAS (b) MV (c) CF-MV (d) ESBMV ($\delta = 0.2$) (e) ESBMV ($\delta = 0.4$) (f) PESBMV ($\delta = 0.2$, $\eta = 0.65$) (g) PESBMV ($\delta = 0.4$, $\eta = 0.35$). All images are displayed with a dynamic range of 50dB.

Table 7.1: *RESOLUTION AND BLACK-BOX REGION MEASUREMENTS FOR THE WIRE PHANTOM USING DIFFERENT BEAMFORMING METHODS WITH PWI.*

Beamformer	FWHM (mm)	μ_{BBR} (dB)	σ_{BBR} (dB)	SSNR_{BBR}
DAS	1.12	-30.02	5.96	1.69
MV	1.20	-27.44	6.07	1.86
CF-MV	0.54	-68.64	10.87	0.75
ESBMV($\delta = 0.2$)	1.20	-65.69	15.88	0.31
ESBMV($\delta = 0.4$)	1.08	-80.12	12.82	0.35
PESBMV($\delta = 0.2, \eta = 0.65$)	1.20	-27.50	6.13	1.84
PESBMV($\delta = 0.4, \eta = 0.35$)	1.20	-27.92	6.51	1.78

Table 7.2: *CONTRAST AND SPECKLE STATISTICS MEASUREMENTS FOR THE CYST PHANTOM USING DIFFERENT BEAMFORMING METHODS WITH PWI.*

Beamformer	μ_{cyst} (dB)	μ_{Bg} (dB)	CR(dB)	CNR	SSNR_{Bg}
DAS	-23.90	-13.18	10.72	1.81	1.86
MV	-23.79	-12.05	11.74	1.89	1.89
CF-MV	-51.01	-28.72	22.29	2.54	0.84
ESBMV($\delta = 0.2$)	-42.44	-13.29	29.15	3.86	1.72
ESBMV($\delta = 0.4$)	-57.81	-21.49	36.32	2.70	1.09
PESBMV($\delta = 0.2, \eta = 0.65$)	-42.00	-13.28	28.72	3.81	1.72
PESBMV($\delta = 0.4, \eta = 0.35$)	-51.37	-18.23	33.14	3.15	1.12

where the lowest mean value of -80.12dB at the BBR among the implemented beamformers is achieved. In the same figure, a complete reduction of the BBR artefacts is shown when using PESBMV at the same values of δ (0.2 and 0.4). Table 7.1 confirms that BBR artefacts are completely reduced from the convergence in the values of the mean, standard deviation and $SSNR_{BBR}$ between MV and PESBMV beamformers.

Table 7.2 shows that a close contrast, measured by CR and CNR, is achieved by DAS and MV beamformers. This contrast is the lowest among the other beamformers, due to their high cystic mean value. When CF is used with MV beamformer, both contrast and resolution are improved. However, the presence of BBR artefacts and the speckle reduction have introduced a significant degradation in the image quality, where the lowest background mean value among the other beamformers of -28.72dB is produced.

In ESBMV when δ is 0.2, the mean value at both the cyst and background is superior to that in DAS and MV. Therefore, higher CR and CNR of 29.15dB and 3.86, are achieved. Increasing δ to 0.4 increases the difference in the mean value between the cyst and background, or CR, while the CNR is reduced as stronger dark spots are presented to the background and thus higher standard deviation is achieved.

At $\delta=0.2$, PESBMV achieved close cyst and background mean values to those in ESBMV, so that similar CR and CNR are achieved. When increasing δ to 0.4, an η of 0.35 is required for a complete elimination of BBR, which results in higher cystic darkness and lower background mean than those at $\delta=0.2$.

7.6.2 Compound Plane-Wave Imaging (CPWI)

The figures and measurements in the previous section are repeated using coherent CPWI, where five angles within the $\pm 10^\circ$ angular range and 5° inter-angles step are compounded. The resulting images of the wire and cyst phantoms are shown in figures 7.6 and 7.7, respectively, while the corresponding measurements of the quality metrics are given in tables 7.3 and 7.4.

It can be noticed that the efficiency of PESBMV in removing BBR artefacts is not reduced by the use of CPWI, where a high similarity in the BBR area between

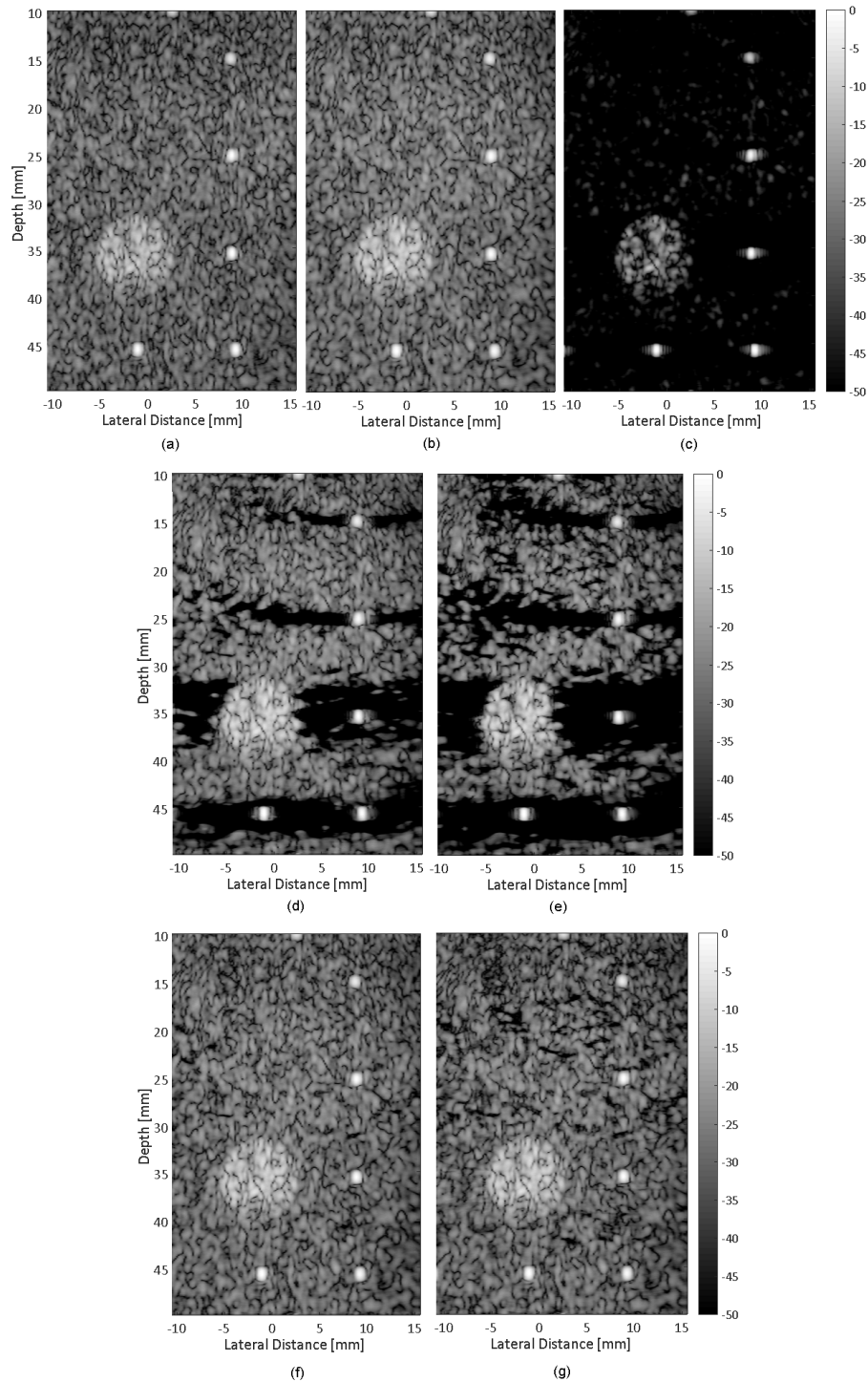


Figure 7.6: Ultrasound images of the experimental RF-data of the wire phantom shown in figure 7.2(a) using CPWI with: (a) DAS (b) MV (c) CF-MV (d) ESBMV ($\delta = 0.2$) (e) ESBMV ($\delta = 0.4$) (f) PESBMV ($\delta = 0.2, \eta = 0.65$) (g) PESBMV ($\delta = 0.4, \eta = 0.35$). All images are displayed with a dynamic range of 50dB.

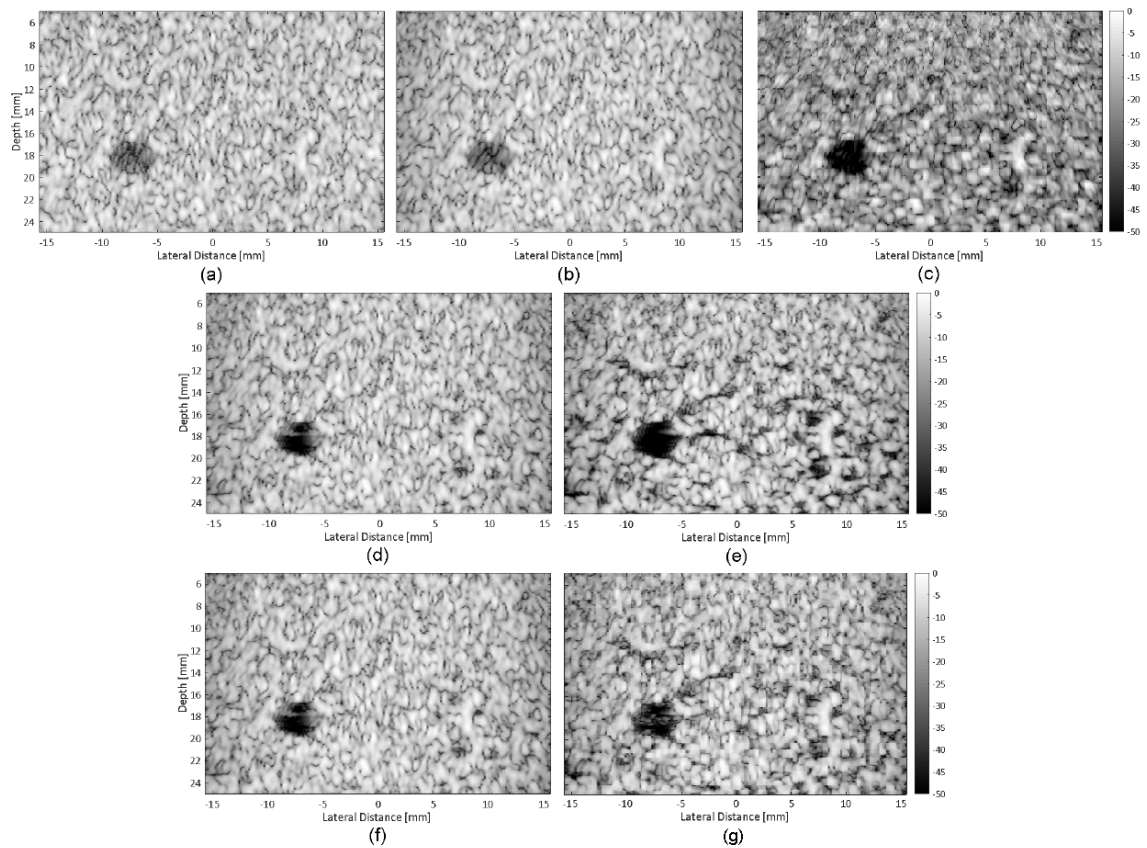


Figure 7.7: Ultrasound images of the experimental RF-data of cyst phantom shown in figure 7.2(c) using CPWI with: (a) DAS (b) MV (c) CF-MV (d) ESBMV ($\delta = 0.2$) (e) ESBMV ($\delta = 0.4$) (f) PESBMV ($\delta = 0.2$, $\eta = 0.65$) (g) PESBMV ($\delta = 0.4$, $\eta = 0.35$). All images are displayed with a dynamic range of 50dB.

Table 7.3: *RESOLUTION AND BLACK-BOX REGION MEASUREMENTS FOR THE WIRE PHANTOM USING DIFFERENT BEAMFORMING METHODS WITH 5-ANGLES CPWI.*

Beamformer	FWHM (mm)	μ_{BBR} (dB)	σ_{BBR} (dB)	SSNR_{BBR}
DAS	0.59	-32.03	5.80	1.75
MV	0.70	-30.48	5.62	1.79
CF-MV	0.48	-67.48	9.67	0.78
ESBMV($\delta = 0.2$)	0.64	-62.29	16.62	0.44
ESBMV($\delta = 0.4$)	0.60	-77.84	13.53	0.29
PESBMV($\delta = 0.2, \eta = 0.65$)	0.70	-30.55	5.59	1.78
PESBMV($\delta = 0.4, \eta = 0.35$)	0.70	-31.02	5.54	1.80

Table 7.4: *CONTRAST AND SPECKLE STATISTICS MEASUREMENTS FOR THE CYST PHANTOM USING DIFFERENT BEAMFORMING METHODS WITH 5-ANGLES CPWI.*

Beamformer	μ_{cyst} (dB)	μ_{Bg} (dB)	CR(dB)	CNR	SSNR_{Bg}
DAS	-31.18	-13.49	17.69	3.03	1.80
MV	-31.98	-12.92	19.05	3.19	1.82
CF-MV	-50.29	-21.86	28.42	3.73	1.02
ESBMV($\delta = 0.2$)	-43.05	-13.27	29.78	4.82	1.71
ESBMV($\delta = 0.4$)	-56.79	-18.22	38.57	3.78	1.28
PESBMV($\delta = 0.2, \eta = 0.65$)	-42.36	-13.27	29.10	4.70	1.71
PESBMV($\delta = 0.4, \eta = 0.35$)	-44.49	-15.74	28.76	3.84	1.32

PESBMV and MV can be noticed in figure 7.6, confirmed by the measurements of the mean, standard deviation and $SSNR_{BBR}$ in table 7.3. Furthermore, table 7.6 shows that the FWHM when using CPWI has been reduced by nearly 50% compared to that in PWI given in table 7.1, for all the implemented types of beamformers except CF-MV, which had a slight improvement in resolution.

Despite the improvement in contrast and resolution achieved using CPWI for CF-MV, only a slight enhancement in the background homogeneity and BBR reduction was attained. On the other hand, CPWI was able to reduce the amount of dark spots presented by ESBMV and PESBMV. This can be clearly noticed by comparing the results of PWI and CPWI of the two beamformers in figures 7.4 and 7.6 for the wire phantom and figures 7.5 and 7.7 for the cyst phantom.

Due to the use of CPWI, contrast is improved for all the beamformers as compared to that in PWI. Only in the case of PESBMV with $\delta=0.4$, CR is reduced by 4.38dB due to the reduced cyst mean value. However, CNR is not correspondingly decreased, due to the improved homogeneity of the background speckle that decreases the standard deviation in the denominator of CNR formula. Although CR can be retained by decreasing the value of η , this will be at the cost of lowering the efficiency of the proposed method in eliminating BBR artefacts.

7.6.3 In-vivo Imaging of a Human Carotid

For further evaluation of the proposed method for medical imaging, beamforming operation for a human carotid RF-data was carried out. Again, the proposed method is compared for this data with DAS, MV, CF-MV and reference ESBMV at $\delta=0.3$, where the resulting images are shown in figure 7.8. This figure shows three types of imaging objects indicated by the circles A, B and C. (A) represents a hypoechoic area, (B) represents a BBR area and (C) contains a deep homogeneous tissue. The resulting images are displayed in a dynamic range of 50dB.

MV shows a close response to that of DAS, where noisy images with low contrast are produced. In CF-MV as expected, a dark image with BBR artefacts and distorted speckle is produced. ESBMV produces a better speckle pattern compared to CF-MV, with a similar darkness in the hypoechoic area due to the

high contrast. However, BBR artefacts are clearly seen in area (B) and dark spots are distorting the tissue in area (C).

When using PESBMV with both of δ and η equal to 0.3, the same level of darkness as that in ESBMV can be seen in the hypoechoic area in (A), while the BBR in area (B) is reduced. Increasing η to 0.4 results in higher BBR reduction, at the cost of lowering the contrast, which can be noticed from the reduced darkness in area (A).

7.7 Discussion

The proposed method of PESBMV is highly efficient in reducing the BBR artefacts commonly introduced in ESBMV beamformer at the sides of any hyperechoic object embedded in a speckle background. When there is no speckle background in the image, for example during the simulations of a PSF or the imaging of a wire phantom in water tank, ESBMV becomes highly efficient (Asl & Mahloojifar, 2010) and the proposed method is not needed.

Designing a beamformer for medical ultrasound imaging requires considering three imaging objects: hyperechoic objects, cystic and hypoechoic objects and speckle generating backgrounds. A beamformer that fails in providing acceptable imaging quality for one of these cases is often infeasible for medical imaging. In the proposed method of Partial ESBMV (PESBMV), the problem of BBR artefacts is solved so that speckle pattern is clearly resolved without affecting the resolution or cystic imaging as a cost.

The drop in the value of N_{sig} in the BBR and strong scattering objects shown in figure 7.2 can be explained by the presence of strong sidelobes at the BBR, that results in increasing the size of the noise subspace matrix and reduces N_{sig} . In the strong scattering area which has a high maximum eigenvalue, λ_{th} in equation (7.3) is increased, and thus the value of N_{sig} is reduced. These two cases do not occur in the cystic or speckle areas, so that N_{sig} is not highly reduced. This property is exploited in the proposed method so that the effect of ESBMV is blocked in the BBR and strong scattering areas, enabling only MV beamforming to be applied, while ESBMV is allowed in other areas. This behaviour of the proposed method gives it the name of Partial ESBMV.

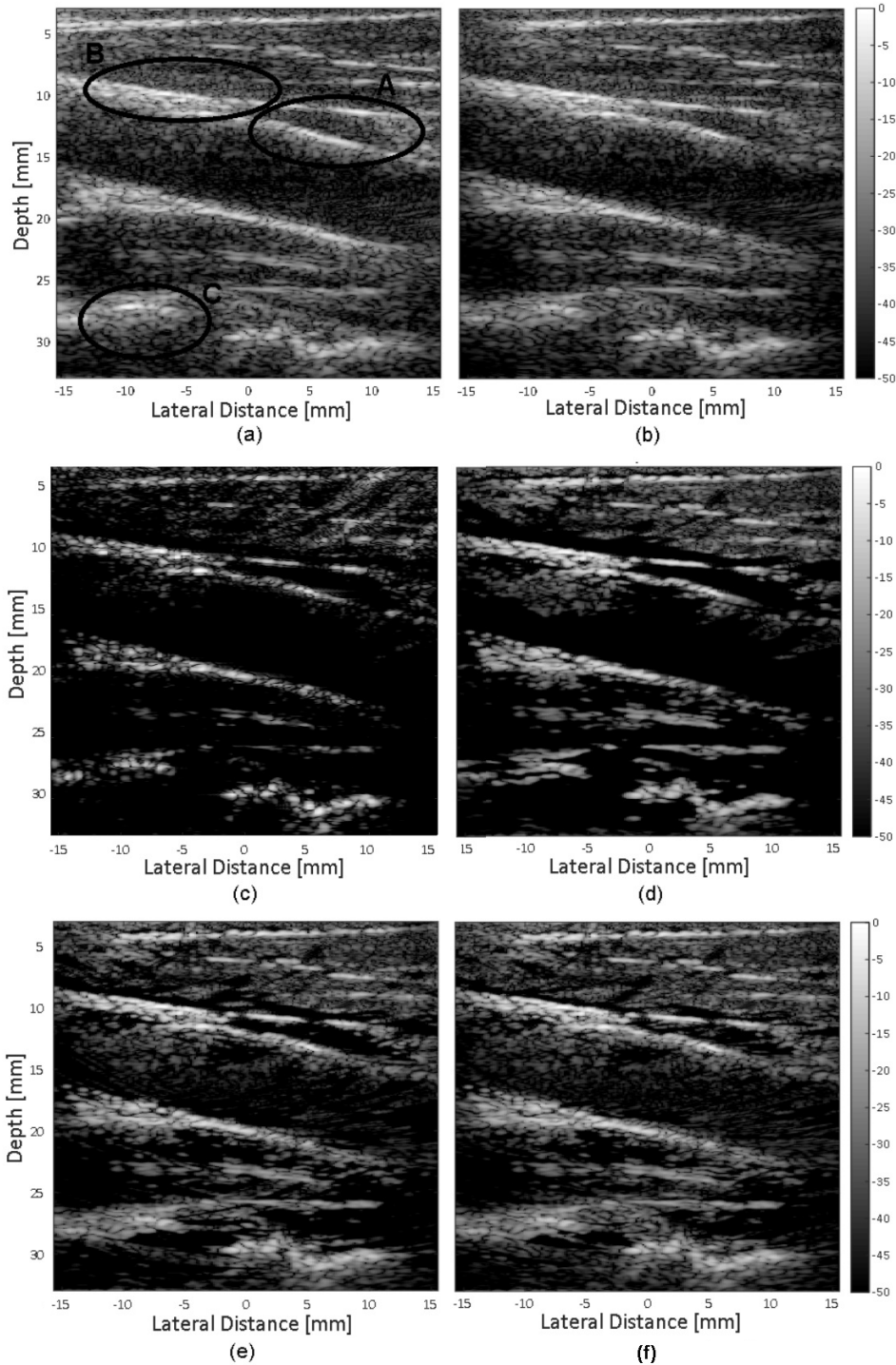


Figure 7.8: Ultrasound images of a human carotid RF-data using: (a) DAS (b) MV (c) CF-MV (d) ESBMV ($\delta=0.3$) (e) PESBMV ($\delta=0.3, \eta=0.3$) (f) PESBMV ($\delta=0.3, \eta=0.4$). Three types of imaging objects are indicated by the circles A, B and C: (A) represents a hypoechoic area, (B) represents a BBR area and (C) contains a deep homogeneous tissue. All images are displayed with a dynamic range of 50 dB.

The artefacts of BBR is a serious problem that limits the efficiency of using ESBMV for medical ultrasound imaging, despite the improvement it adds to contrast and resolution. This is because hyperechoic objects around which, BBR artefacts occur when using ESBMV, appear in almost all of the parts of the human body including bones, stones, deep fat, gas bubbles, cardiac valves and spleen (Lichtenstein, 2010). The proposed method of PESBMV that totally removes BBR artefacts helps increasing the feasibility of using ESBMV for the application of medical ultrasound imaging. In addition, improving the speckle homogeneity and contrast with no BBR artefacts enables to use the proposed method for the application of shear wave Elastography Korukonda (2012), where the displacement is estimated depending mainly on the efficiency of the used beamformer in resolving speckle.

The performance of PESBMV is assessed using experimental data of cyst and wire phantoms, with a comparison with DAS, MV, CF-MV and ESBMV beamformers. The proposed method of detecting BBR areas depending on the number of eigenvectors included in the signal subspace is efficiently exploited to remove these artefacts completely, by simply replacing the image points located in these areas with the response from MV. This technique, as shown in the results section, has the ability to retain MV resolution and ESBMV contrast, simultaneously, without increasing the computational complexity of ESBMV method. Furthermore, the presence of the coefficient η in PESBMV enables it to work with any value of δ by reducing η each time δ is increased, so that the response of MV does not dominate the output image.

It is shown in the literature that merging ESBMV with other beamforming techniques, like subarray coherence-based postfiltering and Wiener postfiltering, can further improve the imaging quality (Zeng *et al.*, 2012; Zhao *et al.*, 2016). However, the use of these techniques with PESBMV results in cancelling its effect in removing BBR artefacts. This happens because the coherence-based factors suffer from the same problem of BBR artefacts due to the incoherency caused by the high level of sidelobes in this area. Furthermore, Wiener postfiltering depends on the level of SNR to filter out the weighting vector, which is highly reduced at the BBR for the same reason. The method that can be combined with PESBMV

to improve performance without re-introducing BBR artefacts into the image is CPWI.

When CPWI is used with ESBMV, both resolution and dark spots reduction are effectively improved. However, BBR artefacts are reduced but not totally removed, as can be seen in figure 7.6(d,e). The presence of PESBMV effectively solves BBR artefacts, and with the help of CPWI, the imaging quality is further improved so that higher resolution, better background homogeneity and less dark spots are presented in the image.

In the method of PESBMV combined with CPWI, it is important to understand the role of the three parameters that control the imaging quality: δ , η and the compounded angles, which is summarized as follows: The number of compounded angles in CPWI has a direct effect on reducing dark spot artefacts and increasing speckle homogeneity, at the cost of expanding the computational burden on the processor. Enlarging the value of δ is used to remove noise and improve contrast, at the cost of increasing the dark spots in the image. Finally, η is the coefficient related to the BBR elimination. Yet increasing η to more than a specific limit has a negative effect on contrast, due to approaching MV behaviour.

Using a value of 0.4 or higher for δ results in eliminating the efficiency of CPWI in decreasing dark spots, and therefore, the value of η needs to be reduced to maintain contrast. This reduction in the value of η may result in reducing the cyst darkness and lowering the efficiency of eliminating BBR. This case can be seen in the results of PESBMV at $\delta=0.4$ and $\eta=0.35$, where CR is less with about 4dB than that in ESBMV with the same δ . Reducing the value of η can cancel this decrease in CR, but this was not done in order to assure a complete removal of BBR artefacts. This case does not mean that the proposed method has a drawback of reducing contrast, but it is only the use of large values of δ that leads to this situation.

In order to achieve the required performance using the proposed method for medical imaging, suitable values should be assigned for δ and η . The value of δ is fixed depending on the amount of noise introduced to the images by the imaging system and the used dynamic range. The selection of η is directly affected by the value of δ as follows: At low values of δ , a value of 0.5 or higher for η can totally eliminate BBR without sacrificing the contrast of reference ESBMV. As

the value of δ increases, a trade-off starts to occur between BBR elimination and contrast, due to having stronger BBR artefacts when increasing δ . This trade-off between contrast and BBR reduction can be noticed by comparing areas (A) and (B) in image (e) with those in image (f) in figure 7.8, where increasing η from 0.3 to 0.4 helped to further reduce BBR in (B) at the cost of degrading the contrast in (A).

It can be noticed that the brightness of the speckle background is higher in the cyst phantom images than that in the wire phantom. The reason of this difference is the normalization operation that is done at the end of the beamforming. In this operation, the output points of the beamformer are divided by their maximum, or equivalently, decreased by their maximum when normalization is performed after converting to decibels. The maximum value in the wire phantom image is taken from the strong scattering lesion or from the wires. As no strong scattering object exists in the images of the cyst phantom, the maximum will be one of the speckle points. This results in increasing the average brightness of these points, due to being close to the maximum value of the image.

The imaging quality of DAS and MV beamformers can be noticed to be similar for the cyst phantom. The reason of that is the low contrast of the two beamformers as mentioned before. In MV, resolution is expected to be higher than that in DAS. However, it can be noticed from the results that worse resolution is achieved when using MV in the two cases of PWI and CPWI. This is due to the low robustness of adaptive beamformers that results from subarray averaging and degrades resolution in the presence of sound speed errors and/or steering vector errors when working with noisy experimental signals, in addition to the use of wires embedded in a speckle background to measure resolution. In order to overcome the problem of the low robustness in MV, methods like diagonal loading and amplitude and phase estimation beamforming can be used.

7.8 Conclusions

ESBMV is a new technique that uses Eigenspace based decomposition to separate the covariance matrix in MV beamformer into signal subspace and noise subspace, enabling a significant increase in contrast, speckle homogeneity and resolution. However, two types of artefacts that limit the performance of this technique in medical imaging exist. They are the BBR and dark-spot artefacts. In this chapter, a new method of Partial ESBMV is proposed as a solution for the problem of BBR artefacts that limits the efficiency of reference ESBMV, where the properties of this beamformer are retained with no additional computational complexity. The performance of Partial ESBMV is investigated using experimental RF-data of cyst and wire phantoms. A complete removal of BBR artefacts is achieved using the proposed method.

Together with CPWI, the proposed method of PESBMV was able to improve lateral resolution, reduce dark-spot artefacts and retain the high contrast provided by ESBMV. These properties of the proposed method will open the way for the use of Eigenspace-based beamforming in different applications in medical ultrasound imaging and shear wave Elastography.

Chapter 8

Conclusions

'Beamforming' is the process of converting the received echo signals into an image to describe the region of interest. This thesis deals with Plane-Wave Imaging (PWI) beamformers, where a complete ultrasound image is produced for the area of interest using a single transmission. This allows data to be acquired with >1000 frames/second, producing new ultrafast imaging applications, such as shear wave tracking and flow motion estimation. Meanwhile, different beamforming techniques have been developed in order to compensate for the lack of focusing in PWI that lowers the imaging quality. This work focuses on two main types of beamformers; Delay-And-Sum (DAS) and Minimum Variance (MV) beamformers.

For DAS beamformer, an empirical expression that describes the relation between lateral resolution with the imaging parameters in PWI is produced. This enables estimation of the imaging quality that can be achieved by knowing the transducer width, transmitted frequency and imaging depth. In addition, a method to calculate the steering range within which the steering angles are selected for Compounded PWI is proposed, depending on the transducer sensitivity, imaging depth and medium attenuation.

For MV beamformer, the Coherence-based Factors and Eigenspace-based MV techniques are studied, with proposing a new method of Partial-ESBMV that solves the problem of BBR artefacts accompanied with reference ESBMV. The presence of this method paves the way for the use of Eigenspace-based beamforming for medical ultrasound imaging.

8.1 Resolution in PWI

In recent years, more attention has been paid to the development of ultrafast imaging techniques for medical ultrasound imaging, where frame rates of thousands of frames per second can be achieved. Selecting the system parameters for a specific type of imaging requires the ability to estimate the effect of each of these parameters on the produced imaging quality. One of the metrics used to assess this quality is resolution, which is defined as the minimum distinguishable distance between two adjacent points located in the lateral or axial direction.

Specifying the effect of the imaging parameters on resolution required studying each of these parameters separately, then an empirical expression can be estimated for resolution based on this study. These parameters are the imaging depth, transmitted frequency, bandwidth, pitch and the total width of the transducer. Lateral resolution is found to be directly proportional to the wavelength and imaging depth and inversely proportional to the total transducer width. According to this study, increasing frequency to more than 10MHz has no effect on lateral resolution. Therefore, when frequencies of higher than that are available, it is more useful to increase bandwidth rather than increasing frequency so that axial resolution is improved. As compared to linear imaging, PWI has higher resolution due to the use of dynamic focusing at the receive and because the whole transducer elements are used as the aperture, in addition to the lack of focusing in PWI that leads to reducing the second harmonics generation which is usually accelerated by the focusing in linear imaging.

It is known that the imaging depth is the parameter that depends on the imaging region and therefore it cannot be controlled. In addition, this depth restricts the range of the transmitted frequencies that can be used. This is because at a specific imaging depth, higher transmitted frequencies are more strongly attenuated. Furthermore, the second harmonics generation is increased with increasing the transmitted frequency and penetration depth, which leads to weakening the fundamental frequency. Therefore, the operation of improving lateral resolution will mainly depend on the width of the transducer. Wider transducers produce higher lateral resolution, with taking into consideration that a complete contact between the body wall and the transducer surface through the use of a matching

material is provided, to eliminate the air gaps and provide higher compatibility between the two surfaces.

8.2 CPWI Parameters

In order to make the correct selection of the number and values of the steering angles in CPWI, it is required to specify what quality parameters need to be improved and the effect of the compounded angles on these parameters. Firstly, the angular range within which the steering angles can be selected is specified depending on the maximum imaging depth, transducer sensitivity and medium attenuation. In addition to be limited by the field of view of the applied transducer, compounding angles from outside the calculated angular range adds no improvement to the imaging. After specifying the angular range, the steering angles can be selected by considering the following points:

- Lateral resolution is directly proportional to the step between the compounded angles. Therefore, it is maximized when only two angles are compounded using the maximum possible angular range. This also maximizes the frame rate of CPWI. However, only odd numbers of angles are compounded in this study because angle 0 is always included to compare with PWI.

- Improving the artefacts reduction and noise removal from individual compounded frames requires increasing the number of frames up to a specific limit, after which, the effect of the added frames will be negligible. In addition to the reduced frame rate, this has a drawback of reducing resolution because within a specific angular range, increasing the number of compounded angles requires reducing the angular step between them.

Following these notes helps in efficiently selecting the proper compounding angles by specifying the imaging parameters and requirements.

8.3 PESBMV

The problem of the BBR in the CF and ESBMV methods occurs due to the strong incoherency of the sidelobes of the hyperechoic objects that appear in the imaging region, which is considered by the beamformer to be noise and therefore

it is highly attenuated. The first step to eliminate BBRs is to find a way to differentiate between this region and the cystic objects. This is because the coherent sum, incoherent sum and SNR are similar in the two regions. Therefore, any reduction in the BBR problem is accompanied with a reduction in the contrast due to the reduced cystic detection, and vice versa. The only factor that is found to be different in the two areas is the number of rows in the signal subspace matrix in ESBMV method. This value is found to be highly reduced in both the hyperechoic objects and BBRs, while it is higher in the speckle backgrounds and cystic objects. This point was exploited in the new method of Partial-ESBMV to find a solution that totally eliminates the BBRs without affecting the cystic targets, and thus the contrast is preserved.

Designing a beamformer for medical ultrasound imaging requires considering three imaging objects: hyperechoic objects, cystic and hypoechoic objects and speckle generating backgrounds. A beamformer that fails in providing acceptable imaging quality for one of these cases is often infeasible for medical imaging. In the proposed method of Partial ESBMV (PESBMV), the problem of BBR artefacts is solved so that speckle pattern is clearly resolved without affecting the resolution or cystic imaging as a cost.

The proposed method of PESBMV combines two conventional and previously published methods; MV and ESBMV. However, the selective implementation of these methods based on the signal intensity values has novelty. This work is original in the way of combining specific areas of the image so that BBR artefacts of ESBMV method are totally eliminated without affecting the efficiency of ESBMV in resolving cystic targets. In addition, the BBRs are detected during the beamforming operation depending on the number of columns of the signal subspace. Differentiating between BBR and cystic targets during the beamforming using this number is the second novelty of the proposed method. In addition to reducing BBR, the proposed method of PESBMV can be combined with CPWI to reduce dark spot artefacts without affecting the efficiency of PESBMV in reducing BBRs. As far as the author is aware, this is the first time CPWI is suggested for effectively reducing dark-spot artefacts in ESBMV.

The presence of the proposed method of PESBMV that removes BBR artefacts usually introduced to the sides of hyperechoic objects by reference ESBMV paves

the way for the use of Eigenspace-Based beamforming in medical ultrasound imaging. This is because hyperechoic objects appear in almost all of the parts of the human body including bones, stones, deep fat, gas bubbles, cardiac valves and spleen.

Appendix

1 Signal Travel Time in CPWI

When a plane wave is transmitted with zero degree (no steering), the distance between each transducer element and the field point is calculated as the perpendicular distance between them. To steer the unfocused transmitted signal with θ degree, the elements are pulsed with a constant delay between each two consecutive elements. In this case, the distance between the transmitter and any field point is calculated by assuming that the x-axis (transducer) is steered with the angle θ , or equally, assuming that the field point is steered with the negative of this angle. This second case is considered during this derivation.

Let $p(x, z)$ be a field point located at x and z axial and lateral distances, respectively. Steering this point with an angle of θ about a centre point $p_c(x_c, z_c)$ results in the new point location $p(x_2, z_2)$, where:

$$z_2 = (x - x_c) \sin \theta + (z - z_c) \cos \theta + z_c. \quad (1)$$

The axial distance of the centre point z_c is always zero, being at the surface of the transducer. Thus equation (1) becomes:

$$z_2 = x \sin \theta - x_c \sin \theta + z \cos \theta. \quad (2)$$

The lateral distance of the centre point x_c depends on the rotation angle; for positive angles, $x_c = W/2$ where W is the total width of the transducer, while for negative angles, $x_c = -W/2$. According to this, equation 2 becomes:

$$z_2 = z \cos \theta + x \sin \theta + \frac{W}{2} \sin |\theta|. \quad (3)$$

These calculations are required for calculating the transmit time in CPWI, while the receiving time is calculated from the direct distance from the focal point to the receiving element, where the steering has no effect on the receiving time.

2 Ring Down Time of the Transducer

During the transmission, the receiving circuit receives the transmitted excitation pulse. This prevents distinguishing any echo reflected from the area near to the transducer surface. That is why this area is called Dead Zone [Goodsitt *et al.* \(1998\)](#). The length of the dead zone depends on the length of the transmitted pulse which can be reduced using backing material or increasing the central frequency of the pulse. The number of samples that are removed from the RF-data so that the transmitted signal is not shown in the image is calculated by:

$$N_{samples} = S_{RD} - \left\lfloor \frac{\frac{N}{2} \cdot d \cdot \sin \theta}{c \cdot T_s} \right\rfloor, \quad (4)$$

where S_{RD} is the number of ring down samples needed to be truncated from the RF-data to eliminate the received excitation signal. The second term of the equation represents the samples corresponding to the delay time needed to steer the signal with angle θ and make the first element to the left or the right of the transducer (depending on the sign of the angle) start sending the signal at $t=0$.

3 Constructed Matlab Functions

In this section, the functions of MV, ESBMV and PESBMV used in this thesis are given.

3.1 MV Function

In this function, MV beamforming is performed for the input RF-data acquired using a plane wave steered with a specific angle.

```
function [Beamformed_data, z_axis, x_axis]= MV(RF_data,theta_d,z_start,  
z_stop,image_width,dx,N_elements,pitch,c,Ts,K,Lp)
```

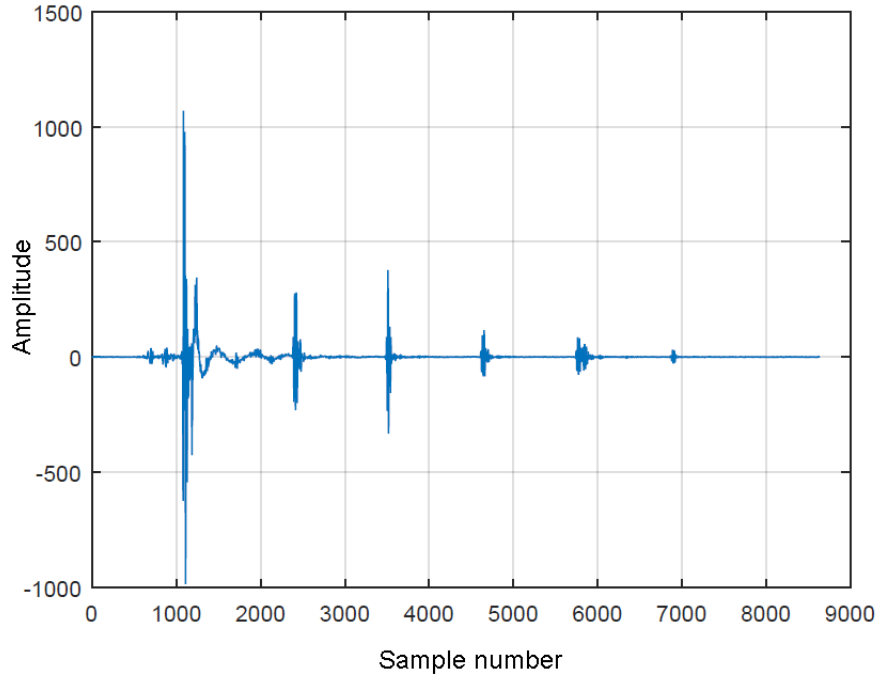


Figure 1: The RF data received by element #64 when imaging the wire phantom with 7 scattering points shown in figure 4.3 with 0° steering angle.

```

td=2*K+1;
dz=c*Ts/2;
P=N_elements-Lp+1;
e=ones(Lp,1);
tdd= (td-1)/2;
time_array=1:size(RF_data,1);
Z=z_start: dz :z_stop;
z_axis=Z;
X=-image_width/2: dx: image_width/2;
x_axis=X;

tdd_matrix= repmat((-tdd:tdd) ,length(Z),1);
Y=zeros(length(Z), td, N_elements);
Beamformed_data=zeros(length(Z), length(X));

```

```

adrs_x=1;
for x=-image_width/2:dx:image_width/2
    d1= Z.*cosd(theta_d)+x*sind(theta_d)+(N_elements pitch/2)*
        sind(abs(theta_d));
    xjj=1;
    for xj=-(N_elements/2)+0.5:(N_elements/2)-0.5
        address_vector=(d1+sqrt(Z.^2+(x-(xj*pitch))^2))/c/Ts;
        address_matrix= repmat(address_vector',1,td);
        final_matrix=address_matrix + tdd_matrix;
        Y(:, :, xjj)=interp1(time_array,RF_data(:, xjj),final_matrix,'linear',0);
        xjj=xjj+1;
    end
    for adrs_z=1:length(Z)
        R=zeros(Lp,Lp);
        sum_Gp=zeros(Lp,td);
        for loopG = 1 : P
            Gp=(shiftdim(Y(adrs_z , : , loopG:loopG+Lp-1 ),1))';
            R=R+(Gp * conj(Gp'));
            sum_Gp=sum_Gp+Gp;
        end
        R=R/P;
        w=(R \ e) / (conj(e') * (R \ e)) ;
        % [w]=func_ESBMV(R,w,0.4); %uncomment to use ESBMV
        % [w]=func_PESBMV(R,w,0.4, 0.3); %uncomment to use PESBMV
        B= conj(w') * (sum_Gp / P);
        Beamformed_data(adrs_z,adrs_x)=B((td+1)/2);
    end
    adrs_x=adrs_x+1;
end
Beamformed_data(find(isnan(Beamformed_data))) = 0;

```

3.2 ESBMV Function

The function of ESBMV produces a new weighting vector that replaces the weight of the MV. Therefore it is called from the MV function given above.

```
function [W_ESBMV]= func_ESBMV (R,w, Delta)
[Ei_vec, Ei_val]= eig(R);
Ei_val=diag(Ei_val);
% Sorting eigenvalues in descending order with sorting the
corresponding eigenvectors:
for i=1:length(Ei_val)-1
    max_add=i;
    for j=i+1:length(Ei_val)
        if Ei_val(max_add) < Ei_val(j)
            max_add=j;
        end
    end
    Ei_val([i max_add])=Ei_val([max_add i]);
    Ei_vec(:, [i max_add])=Ei_vec(:, [max_add i]);
end
% end of sorting.
Ei_val(Ei_val<(Ei_val(1)*Delta))=[];
Num=length(Ei_val);
Es=Ei_vec(:, 1:Num);
W_ESBMV= Es * conj(Es)' * w ;
```

3.3 PESBMV Function

The function of PESBMV produces a new weighting vector that replaces the weight of the MV. Therefore it is called from the MV function given above.

```
function [W_PESBMV]= func_ESBMV (R, w, Delta, Eta)
[Ei_vec, Ei_val]= eig(R);
Ei_val=diag(Ei_val);
% Sorting eigenvalues in descending order with sorting the
corresponding eigenvectors:
```

```
for i=1:length(Ei_val)-1
    max_add=i;
    for j=i+1:length(Ei_val)
        if Ei_val(max_add) < Ei_val(j)
            max_add=j;
        end
    end
    Ei_val([i max_add])=Ei_val([max_add i]);
    Ei_vec(:, [i max_add])=Ei_vec(:, [max_add i]);
end
% end of sorting.
Ei_val(Ei_val<(Ei_val(1)*Delta))=[];
Num=length(Ei_val);
if Num<=length(w)*Eta
    W_PESBMV=w;
else
    Es=Ei_vec(:, 1:Num);
    W_PESBMV= Es * conj(Es)' * w ;
end
```

References

- ALIABADI, S., YU, J. & WANG, Y. (2015). Enhance contrast in pca based beamformers using smoothing kernel. *Bio-Medical Materials and Engineering*, **26**, S1613–S1621. [4](#), [119](#)
- ALOMARI, Z., HARPUT, S., HYDER, S. & FREEAR, S. (2014). Selecting the number and values of the cpwi steering angles and the effect of that on imaging quality. In *IEEE International Ultrasonics Symposium (IUS)*,, 1191–1194, IEEE. [i](#)
- ALOMARI, Z., HARPUT, S., HYDER, S. & FREEAR, S. (2015). The effect of the transducer parameters on spatial resolution in plane-wave imaging. In *IEEE International Ultrasonics Symposium (IUS)*,, 1–4, IEEE. [i](#)
- ASL, B.M. & MAHLOOJIFAR, A. (2009). Minimum variance beamforming combined with adaptive coherence weighting applied to medical ultrasound imaging. *IEEE Transactions on Ultrasonics, Ferroelectrics and Frequency Control*,, **56**, 1923–1931. [72](#), [87](#)
- ASL, B.M. & MAHLOOJIFAR, A. (2010). Eigenspace-based minimum variance beamforming applied to medical ultrasound imaging. *IEEE Transactions on Ultrasonics, Ferroelectrics, and Frequency Control*,, **57**, 2381–2390. [119](#), [121](#), [123](#), [137](#)
- ASL, B.M. & MAHLOOJIFAR, A. (2012). A low-complexity adaptive beamformer for ultrasound imaging using structured covariance matrix. *IEEE Transactions on Ultrasonics, Ferroelectrics, and Frequency Control*,, **59**, 660–667. [5](#), [72](#), [73](#)

REFERENCES

- AUSTENG, A., NILSEN, C., JENSEN, A.C., NASHOLM, S. & HOLM, S. (2011). Coherent plane-wave compounding and minimum variance beamforming. In *IEEE International Ultrasonics Symposium (IUS)*, 2448–2451, IEEE. [3](#)
- AVANJI, S.A.I., FAR, A.M. & ASL, B.M. (2013). Investigation of the effects of transducer parameters on adaptive mv beamformers in medical ultrasound applications. In *21st Iranian Conference on Electrical Engineering (ICEE)*, 1–6, IEEE. [34](#), [87](#)
- AZHARI, H. (2010). *Basics of biomedical ultrasound for engineers*. John Wiley & Sons. [29](#), [30](#)
- BAUN, J. (2004). Physical principles of general and vascular sonography. *California Publ. Co.* [58](#)
- BERCOFF, J. (2011). Ultrafast ultrasound imaging. *Ultrasound Imaging-Medical Applications*, 3–24. [2](#), [5](#), [7](#), [12](#), [13](#)
- BERCOFF, J., TANTER, M., SANDRIN, L., CATHELINE, S. & FINK, M. (2001). Ultrafast compound imaging for 2d displacement vector measurements: Application to transient elastography and color flow mapping. In *IEEE International Ultrasonics Symposium (IUS)*, vol. 2, 1619–1622, IEEE. [25](#)
- BERCOFF, J., TANTER, M. & FINK, M. (2004). Supersonic shear imaging: a new technique for soft tissue elasticity mapping. *IEEE Transactions on Ultrasonics, Ferroelectrics and Frequency Control*, **51**, 396–409. [2](#), [25](#)
- BERCOFF, J., MONTALDO, G., LOUPAS, T., SAVERY, D., MEZIERE, F., FINK, M. & TANTER, M. (2011). Ultrafast compound doppler imaging: providing full blood flow characterization. *IEEE Transactions on Ultrasonics, Ferroelectrics and Frequency Control*, **58**, 134–147. [2](#), [26](#)
- BERSON, M., RONCIN, A. & POURCELOT, L. (1981). Compound scanning with an electrically steered beam. *Ultrasonic Imaging*, **3**, 303–308. [2](#)
- BHARGAVA, N. & KULSHRESHTHA, N.B.S.G.D. (1984). *Basic Electronics and Linear Circuits*. Tata McGraw-Hill Education. [12](#)

-
- BUI, A.A. & TAIRA, R.K. (2009). *Medical imaging informatics*. Springer Science & Business Media. [1](#)
- BUSHBERG, J.T. & BOONE, J.M. (2011). *The essential physics of medical imaging*. Lippincott Williams & Wilkins. [28](#)
- CAMACHO, J., PARRILLA, M. & FRITSCH, C. (2009). Phase coherence imaging. *IEEE Transactions on Ultrasonics, Ferroelectrics and Frequency Control*, **56**, 958–974. [3](#), [90](#), [91](#)
- CAPON, J. (1969). High-resolution frequency-wavenumber spectrum analysis. *Proceedings of the IEEE*, **57**, 1408–1418. [2](#), [63](#)
- CHENG, J., SERRA-HSU, F., TIAN, Y., LIN, W. & QIN, Y.X. (2011). Effects of phase cancellation and receiver aperture size on broadband ultrasonic attenuation for trabecular bone in vitro. *Ultrasound in Medicine and Biology*, **37**, 2116–2125. [71](#)
- COBBOLD, R.S.C. (2007). *Foundations of Biomedical Ultrasound*. Oxford University Press, Inc. [11](#), [13](#), [16](#)
- COUTURE, O., BANNOUF, S., MONTALDO, G., AUBRY, J.F., FINK, M. & TANTER, M. (2009). Ultrafast imaging of ultrasound contrast agents. *Ultrasound in Medicine & Biology*, **35**, 1908–1916. [27](#)
- COUTURE, O., FINK, M. & TANTER, M. (2012). Ultrasound contrast plane wave imaging. *IEEE Transactions on Ultrasonics, Ferroelectrics and Frequency Control*, **59**. [2](#), [27](#)
- COWELL, D.M., SMITH, P.R. & FREEAR, S. (2013). Phase-inversion-based selective harmonic elimination (pi-she) in multi-level switched-mode tone-and frequency-modulated excitation. *IEEE Transactions on Ultrasonics, Ferroelectrics, and Frequency Control*, **60**, 1084–1097. [120](#)
- CULJAT, M.O., GOLDENBERG, D., TEWARI, P. & SINGH, R.S. (2010). A review of tissue substitutes for ultrasound imaging. *Ultrasound in Medicine and Biology*, **36**, 861–873. [49](#), [50](#)

REFERENCES

- DELANNOY, B., TORGUET, R., BRUNEEL, C., BRIDOUX, E., ROUVAEN, J. & LASOTA, H. (1979). Acoustical image reconstruction in parallel-processing analog electronic systems. *Journal of Applied Physics*, **50**, 3153–3159. [2](#)
- DELCHAR, T.A. (1997). *Physics in medical diagnosis*, vol. 11. Springer. [17](#)
- DEYLAMI, A.M. & ASL, B.M. (2016). Low complex subspace minimum variance beamformer for medical ultrasound imaging. *Ultrasonics*, **66**, 43–53. [89](#)
- DIAMANTIS, K., VOXEN, I.H., GREENAWAY, A.H., ANDERSON, T., JENSEN, J.A. & SBOROS, V. (2014). A comparison between temporal and subband minimum variance adaptive beamforming. In *SPIE Medical Imaging*, 90400L–90400L, International Society for Optics and Photonics. [66](#)
- DUCK, F.A. (2002). Nonlinear acoustics in diagnostic ultrasound. *Ultrasound in Medicine & Biology*, **28**, 1–18. [41](#)
- ENTREKIN, R.R., PORTER, B.A., SILLESEN, H.H., WONG, A.D., COOPERBERG, P.L. & FIX, C.H. (2001). Real-time spatial compound imaging: application to breast, vascular, and musculoskeletal ultrasound. In *Seminars in Ultrasound, CT and MRI*, vol. 22, 50–64, Elsevier. [23](#), [45](#)
- GAN, W.S. (2012). *Acoustical Imaging: Techniques and Applications for Engineers*. John Wiley & Sons. [17](#)
- GOODSITT, M.M., CARSON, P.L., WITT, S., HYKES, D.L. & KOFLER JR, J.M. (1998). Real-time b-mode ultrasound quality control test procedures. report of aapm ultrasound task group no. 1. *Med Phys*, **25**, 1385–1406. [149](#)
- GORCE, J.M., ARDITI, M. & SCHNEIDER, M. (2000). Influence of bubble size distribution on the echogenicity of ultrasound contrast agents: a study of sonovue. *Investigative Radiology*, **35**, 661–671. [27](#)
- HARPUR, S. & BOZKURT, A. (2008). Ultrasonic phased array device for acoustic imaging in air. *IEEE Sensors Journal*, **8**, 1755–1762. [17](#), [18](#)

REFERENCES

- HARPUT, S., ARIF, M., MCLAUGHLAN, J., COWELL, D.M. & FREEAR, S. (2013). The effect of amplitude modulation on subharmonic imaging with chirp excitation. *IEEE Transactions on Ultrasonics, Ferroelectrics and Frequency Control*, **60**, 2532–2544. [49](#)
- HARPUT, S., MCLAUGHLAN, J., COWELL, D.M. & FREEAR, S. (2014). New performance metrics for ultrasound pulse compression systems. In *IEEE International Ultrasonics Symposium (IUS)*, 440–443, IEEE. [29](#), [30](#), [74](#), [127](#)
- HASEGAWA, H. & KANAI, H. (2015). Effect of element directivity on adaptive beamforming applied to high-frame-rate ultrasound. *IEEE Transactions on Ultrasonics, Ferroelectrics, and Frequency Control*, **62**, 511–523. [96](#)
- HEDRICK, W.R. (2013). *Technology for Diagnostic Sonography*. Elsevier Health Sciences. [29](#)
- HERNANDEZ, A., BASSET, O., CHIROSSEL, P. & GIMENEZ, G. (1996). Spatial compounding in ultrasonic imaging using an articulated scan arm. *Ultrasound in Medicine & Biology*, **22**, 229–238. [45](#)
- HINDI, A., PETERSON, C. & BARR, R.G. (2013). Artifacts in diagnostic ultrasound. *Reports in Medical Imaging*, **6**. [58](#)
- HOLFORT, I.K., GRAN, F. & JENSEN, J.A. (2008a). Investigation of sound speed errors in adaptive beamforming. In *IEEE International Ultrasonics Symposium (IUS)*, 1080–1083, IEEE. [5](#), [24](#), [72](#)
- HOLFORT, I.K., GRAN, F. & JENSEN, J.A. (2008b). Plane wave medical ultrasound imaging using adaptive beamforming. In *5th IEEE Sensor Array and Multichannel Signal Processing Workshop*, 288–292, IEEE. [15](#), [63](#)
- HOLFORT, I.K., GRAN, F. & JENSEN, J.A. (2009). Broadband minimum variance beamforming for ultrasound imaging. *IEEE Transactions on Ultrasonics, Ferroelectrics and Frequency Control*, **56**, 314–325. [66](#), [67](#), [68](#), [69](#)
- HOLFORT, I.K., GRAN, F. & JENSEN, J.A. (2010). High resolution ultrasound imaging using adaptive beamforming with reduced number of active elements. *Physics Procedia*, **3**, 659–665. [34](#)

REFERENCES

- HOLLMAN, K., RIGBY, K. & O'DONNELL, M. (1999). Coherence factor of speckle from a multi-row probe. In *IEEE International Ultrasonics Symposium (IUS), Proceedings.*, vol. 2, 1257–1260, IEEE. [3](#), [87](#)
- HUANG, J., TRIEDMAN, J.K., VASILYEV, N.V., SUEMATSU, Y., CLEVELAND, R.O. & DUPONT, P.E. (2007). Imaging artifacts of medical instruments in ultrasound-guided interventions. *Journal of Ultrasound in Medicine*, **26**, 1303–1322. [17](#), [36](#)
- HUBER, S., WAGNER, M., MEDL, M. & CZEMBIREK, H. (2002). Real-time spatial compound imaging in breast ultrasound. *Ultrasound in Medicine and Biology*, **28**, 155–163. [23](#), [45](#)
- JENSEN, J.A. (1999). Linear description of ultrasound imaging systems. *Notes for the International Summer School on Advanced Ultrasound Imaging, Technical University of Denmark July*, **5**. [54](#)
- JENSEN, J.A. (2001). Users guide for the field ii program. *Technical University of Denmark*, **2800**. [28](#)
- JESPERSEN, S.K., WILHJELM, J.E. & SILLESEN, H. (2000). $\text{\textcircled{ij}}$ in vitro $\text{\textcircled{ij}}$ spatial compound scanning for improved visualization of atherosclerosis. *Ultrasound in Medicine and Biology*, **26**, 1357–1362. [23](#), [45](#)
- KERN, R., SZABO, K., HENNERICI, M. & MEAIRS, S. (2004). Characterization of carotid artery plaques using real-time compound b-mode ultrasound. *Stroke*, **35**, 870–875. [45](#)
- KORUKONDA, S. (2012). *Application of synthetic aperture imaging to non-invasive vascular elastography*. Ph.D. thesis, University of Rochester. [19](#), [139](#)
- KOSSOFF, G., GARRETT, W., CARPENTER, D., JELLINS, J. & DADD, M. (1976). Principles and classification of soft tissues by grey scale echography. *Ultrasound in Medicine & Biology*, **2**, 89–105. [2](#)
- KREMKAU, F. & TAYLOR, K. (1986). Artifacts in ultrasound imaging. *Journal of Ultrasound in Medicine*, **5**, 227–237. [28](#)

REFERENCES

- LEDIJU, M.A., TRAHEY, G.E., BYRAM, B.C. & DAHL, J.J. (2011). Short-lag spatial coherence of backscattered echoes: imaging characteristics. *IEEE Transactions on Ultrasonics, Ferroelectrics, and Frequency Control*, **58**, 1377–1388. [96](#), [128](#)
- LEE, C.C. & LEE, J.H. (1997). Eigenspace-based adaptive array beamforming with robust capabilities. *IEEE Transactions on Antennas and Propagation*, **45**, 1711–1716. [4](#), [118](#), [121](#)
- LEONDES, C.T. (2007). *Mems/Nems:(1) Handbook Techniques and Applications Design Methods,(2) Fabrication Techniques,(3) Manufacturing Methods,(4) Sensors and Actuators,(5) Medical Applications and MOEMS*. Springer. [17](#)
- LI, J. & STOICA, P. (2005). *Robust adaptive beamforming*, vol. 88. John Wiley & Sons. [69](#), [71](#), [72](#)
- LI, P.C. & LI, M.L. (2003). Adaptive imaging using the generalized coherence factor. *IEEE Transactions on Ultrasonics, Ferroelectrics, and Frequency Control*, **50**, 128–141. [3](#), [88](#), [89](#), [93](#)
- LICHTENSTEIN, D.A. (2010). *Whole body ultrasonography in the critically ill*. Springer Science & Business Media. [139](#)
- LO, K.W. (2004). Adaptive array processing for wide-band active sonars. *IEEE Journal of Oceanic Engineering*, **29**, 837–846. [63](#)
- MACÉ, E., MONTALDO, G., COHEN, I., BAULAC, M., FINK, M. & TANTER, M. (2011). Functional ultrasound imaging of the brain. *Nature methods*, **8**, 662–664. [4](#)
- MADISETTI, V. (2009). *Wireless, networking, radar, sensor array processing, and nonlinear signal processing*. CRC Press. [65](#)
- MANN, J.A. & WALKER, W. (2002). A constrained adaptive beamformer for medical ultrasound: Initial results. In *IEEE International Ultrasonics Symposium (IUS), Proceedings.*, vol. 2, 1807–1810, IEEE. [3](#)

REFERENCES

- MEHDIZADEH, S., AUSTENG, A., JOHANSEN, T.F. & HOLM, S. (2012a). Eigenspace based minimum variance beamforming applied to ultrasound imaging of acoustically hard tissues. *IEEE Transactions on Medical Imaging*, **31**, 1912–1921. [4](#), [118](#), [121](#), [123](#)
- MEHDIZADEH, S., AUSTENG, A., JOHANSEN, T.F. & HOLM, S. (2012b). Minimum variance beamforming applied to ultrasound imaging with a partially shaded aperture. *IEEE Transactions on Ultrasonics, Ferroelectrics and Frequency Control*, **59**, 683–693. [63](#)
- MEOLA, M., PETRUCCI, I. & RONCO, C. (2016). Ultrasound imaging in acute and chronic kidney disease. *Am J Nephrol*, **43**, 305–388. [2](#)
- MOHANA SHANKAR, P. & NEWHOUSE, V. (1985). Speckle reduction with improved resolution in ultrasound images. *IEEE Transactions on Sonics and Ultrasonics*, **32**, 537–543. [23](#)
- MONTALDO, G., TANTER, M., BERCOFF, J., BENECH, N. & FINK, M. (2009). Coherent plane-wave compounding for very high frame rate ultrasonography and transient elastography. *IEEE Transactions on Ultrasonics, Ferroelectrics and Frequency Control*, **56**, 489–506. [2](#), [4](#), [12](#), [14](#), [19](#), [20](#), [23](#), [25](#), [46](#)
- MONTALDO, G., MACÉ, E., COHEN, I., BERCKOFF, J., TANTER, M. & FINK, M. (2010). Ultrafast compound doppler imaging: a new approach of doppler flow analysis. In *IEEE International Symposium on Biomedical Imaging: From Nano to Macro*, 324–327, IEEE. [26](#)
- NILSEN, C.I.C. & HOLM, S. (2010). Wiener beamforming and the coherence factor in ultrasound imaging. *IEEE Transactions on Ultrasonics, Ferroelectrics and Frequency Control*, **57**, 1329–1346. [87](#), [88](#), [90](#), [92](#)
- OPRETZKA, J., VOGT, M. & ERMERT, H. (2011). A high-frequency ultrasound imaging system combining limited-angle spatial compounding and model-based synthetic aperture focusing. *IEEE Transactions on Ultrasonics, Ferroelectrics and Frequency Control*, **58**, 1355–1365. [23](#), [45](#)

REFERENCES

- PAPADACCI, C., PERNOT, M., COUADE, M., FINK, M. & TANTER, M. (2014). High-contrast ultrafast imaging of the heart. *IEEE Transactions on Ultrasonics, Ferroelectrics and Frequency Control*, **61**, 288–301. [16](#), [23](#)
- PARK, S., AGLYAMOV, S.R., SCOTT, W.G. & EMELIANOV, S.Y. (2007). Strain imaging using conventional and ultrafast ultrasound imaging: Numerical analysis. *IEEE Transactions on Ultrasonics, Ferroelectrics and Frequency Control*, **54**, 987–995. [2](#), [26](#)
- PARK, S., KARPIOUK, A.B., AGLYAMOV, S.R. & EMELIANOV, S.Y. (2008). Adaptive beamforming for photoacoustic imaging. *Optics Letters*, **33**, 1291–1293. [63](#)
- RAITON, B., MCLAUGHLAN, J.R., SMITH, P.R., COWELL, D.M., HARPUT, S. & FREEAR, S. (2011). Counter flow microbubble channeling using acoustic radiation force funnel. In *IEEE International Ultrasonics Symposium (IUS)*, 2432–2435, IEEE. [49](#)
- RAMALLI, A., BASSET, O., CACHARD, C. & TORTOLI, P. (2010). Quasi-static elastography based on high frame-rate imaging and frequency domain displacement estimation. In *IEEE International Ultrasonics Symposium (IUS)*, 9–12, IEEE. [24](#), [26](#)
- RIGHETTI, R., SRINIVASAN, S. & OPHIR, J. (2003). Lateral resolution in elastography. *Ultrasound in Medicine & Biology*, **29**, 695–704. [29](#), [39](#)
- SANDERS, R.C. & WINTER, T.C. (2007). *Clinical sonography: a practical guide*. Lippincott Williams & Wilkins. [17](#)
- SASSO, M. & COHEN-BACRIE, C. (2005). Medical ultrasound imaging using the fully adaptive beamformer. In *IEEE International Conference on Acoustics, Speech, and Signal Processing, Proceedings.*, vol. 2, 489–492. [66](#)
- SCHÄBERLE, W. (2010). *Ultrasonography in vascular diagnosis: A therapy-oriented textbook and atlas*. Springer Science & Business Media. [11](#)

REFERENCES

- SCHICKERT, M., KRAUSE, M. & MÜLLER, W. (2003). Ultrasonic imaging of concrete elements using reconstruction by synthetic aperture focusing technique. *Journal of Materials in Civil Engineering*, **15**, 235–246. [12](#)
- SEKIHARA, K., NAGARAJAN, S.S., POEPEL, D., MARANTZ, A. & MIYASHITA, Y. (2002). Application of an meg eigenspace beamformer to reconstructing spatio-temporal activities of neural sources. *Human Bbrain Mapping*, **15**, 199–215. [4](#), [118](#)
- SEO, C.H. (2008). *Improved contrast in ultrasound imaging using dual apodization with cross-correlation*. ProQuest. [127](#)
- SER, W., CHEN, H. & YU, Z.L. (2007). Self-calibration-based robust near-field adaptive beamforming for microphone arrays. *IEEE Transactions on Circuits and Systems II: Express Briefs*, **54**, 267–271. [63](#)
- SHAN, T.J. & KAILATH, T. (1985). Adaptive beamforming for coherent signals and interference. *IEEE Transactions on Acoustics, Speech and Signal Processing*, **33**, 527–536. [67](#)
- SHUNG, K.K. (2005). *Diagnostic ultrasound: Imaging and blood flow measurements*. CRC press. [29](#)
- SMITH, P.R., COWELL, D.M., RAITON, B., KY, C.V. & FREEAR, S. (2012). Ultrasound array transmitter architecture with high timing resolution using embedded phase-locked loops. *IEEE Transactions on Ultrasonics, Ferroelectrics and Frequency Control*, **59**, 40–49. [49](#), [120](#)
- SMITH, P.R., COWELL, D.M. & FREEAR, S. (2013). Width-modulated square-wave pulses for ultrasound applications. *IEEE Transactions on Ultrasonics, Ferroelectrics, and Frequency Control*, **60**, 2244–2256. [120](#)
- SYNNEVAG, J.F., AUSTENG, A. & HOLM, S. (2007). Adaptive beamforming applied to medical ultrasound imaging. *IEEE Transactions on Ultrasonics, Ferroelectrics and Frequency Control*, **54**, 1606–1613. [15](#), [65](#), [66](#), [67](#), [68](#), [71](#), [72](#), [73](#)

REFERENCES

- SYNNEVÅG, J.F., NILSEN, C.I. & HOLM, S. (2007). speckle statistics in adaptive beamforming. In *IEEE International Ultrasonics Symposium (IUS)*,, 1545–1548, IEEE. [65](#)
- SYNNEVAG, J.F., AUSTENG, A. & HOLM, S. (2009). Benefits of minimum-variance beamforming in medical ultrasound imaging. *IEEE Transactions on Ultrasonics, Ferroelectrics and Frequency Control*,, **56**, 1868–1879. [65](#), [71](#), [72](#), [73](#)
- SYNNEVAG, J.F., AUSTENG, A. & HOLM, S. (2011). A low-complexity data-dependent beamformer. *IEEE Transactions on Ultrasonics, Ferroelectrics, and Frequency Control*,, **58**, 281–289. [73](#)
- SZABO, T.L. (2004). *Diagnostic ultrasound imaging: inside out*. Academic Press. [17](#), [24](#), [25](#)
- SZABO, T.L. & LEWIN, P.A. (2013). Ultrasound transducer selection in clinical imaging practice. *Journal of Ultrasound in Medicine*, **32**, 573–582. [34](#)
- TORBATIAN, Z., ADAMSON, R. & BROWN, J. (2012). A virtual point source pulse probing technique for suppressing grating lobes in large-pitch phased arrays. In *IEEE International Ultrasonics Symposium (IUS)*,, 1291–1294, IEEE. [90](#)
- VAN VEEN, B.D. (1988). Eigenstructure based partially adaptive array design. *IEEE Transactions on Antennas and Propagation*, **36**, 357–362. [4](#), [118](#)
- VAN VEEN, B.D., VAN DRONGELEN, W., YUCHTMAN, M. & SUZUKI, A. (1997). Localization of brain electrical activity via linearly constrained minimum variance spatial filtering. *IEEE Transactions on Biomedical Engineering*, **44**, 867–880. [3](#)
- VARGHESE, T. (2009). Quasi-static ultrasound elastography. *Ultrasound Clinics*, **4**, 323. [26](#)
- VOGT, M. & ERMERT, H. (2008). Limited-angle spatial compound imaging of skin with high-frequency ultrasound (20 mhz). *IEEE Transactions on Ultrasonics, Ferroelectrics and Frequency Control*,, **55**, 1975–1983. [45](#)

REFERENCES

- VON RAMM, O.T. & SMITH, S.W. (1983). Beam steering with linear arrays. *IEEE Transactions on Biomedical Engineering*, 438–452. [17](#)
- WAN, M., FENG, Y. & TER HAAR, G. (2015). *Cavitation in Biomedicine: Principles and Techniques*. Springer. [69](#)
- WANG, S.L. & LI, P.C. (2009). Mvdr-based coherence weighting for high-frame-rate adaptive imaging. *IEEE Transactions on Ultrasonics, Ferroelectrics and Frequency Control*, **56**, 2097–2110. [3](#), [90](#)
- WANG, Y.H. & LI, P.C. (2014). Snr-dependent coherence-based adaptive imaging for high-frame-rate ultrasonic and photoacoustic imaging. *IEEE Transactions on Ultrasonics, Ferroelectrics, and Frequency Control*, **61**, 1419–1432. [4](#), [89](#), [92](#), [93](#), [96](#)
- WANG, Z., LI, J. & WU, R. (2005). Time-delay-and time-reversal-based robust capon beamformers for ultrasound imaging. *IEEE Transactions on Medical Imaging*, **24**, 1308–1322. [3](#)
- WARD, M. (1999). Ultrasound atlas of vascular diseases. *Radiologic Technology*, **71**, 93–93. [39](#)
- WEINSTEIN, S.P., CONANT, E.F. & SEHGAL, C. (2006). Technical advances in breast ultrasound imaging. In *Seminars in Ultrasound, CT and MRI*, vol. 27, 273–283, Elsevier. [23](#)
- WILHJELM, J.E., JENSEN, M., JESPERSEN, S., SAHL, B. & FALK, E. (2004). Visual and quantitative evaluation of selected image combination schemes in ultrasound spatial compound scanning. *IEEE Transactions on Medical Imaging*, **23**, 181–190. [2](#), [45](#)
- XU, M., YANG, X., DING, M. & YUCHI, M. (2014). Spatio-temporally smoothed coherence factor for ultrasound imaging [correspondence]. *IEEE Transactions on Ultrasonics, Ferroelectrics, and Frequency Control*, **61**, 182–190. [3](#), [88](#), [91](#), [96](#), [128](#)

REFERENCES

- ZENG, X., CHEN, C. & WANG, Y. (2012). Eigenspace-based minimum variance beamformer combined with wiener postfilter for medical ultrasound imaging. *Ultrasonics*, **52**, 996–1004. [92](#), [118](#), [119](#), [121](#), [123](#), [139](#)
- ZENG, X., WANG, Y., YU, J. & GUO, Y. (2013). Correspondence-beam-domain eigenspace-based minimum variance beamformer for medical ultrasound imaging. *IEEE Transactions on Ultrasonics, Ferroelectrics and Frequency Control*, **60**, 2670–2676. [73](#)
- ZHAO, J., WANG, Y., YU, J., GUO, W., LI, T. & ZHENG, Y.P. (2016). Subarray coherence based postfilter for eigenspace based minimum variance beamformer in ultrasound plane-wave imaging. *Ultrasonics*, **65**, 23–33. [4](#), [118](#), [119](#), [139](#)